

8-1-2024

New Insights into the Diverse Intraplate Volcanism Present within the Howland and Baker Island United States Exclusive Economic Zone

Nicholas Foresta

Follow this and additional works at: <https://digitalscholarship.unlv.edu/thesesdissertations>



Part of the [Geology Commons](#), and the [Oceanography and Atmospheric Sciences and Meteorology Commons](#)

Repository Citation

Foresta, Nicholas, "New Insights into the Diverse Intraplate Volcanism Present within the Howland and Baker Island United States Exclusive Economic Zone" (2024). *UNLV Theses, Dissertations, Professional Papers, and Capstones*. 5115.

<https://digitalscholarship.unlv.edu/thesesdissertations/5115>

This Thesis is protected by copyright and/or related rights. It has been brought to you by Digital Scholarship@UNLV with permission from the rights-holder(s). You are free to use this Thesis in any way that is permitted by the copyright and related rights legislation that applies to your use. For other uses you need to obtain permission from the rights-holder(s) directly, unless additional rights are indicated by a Creative Commons license in the record and/or on the work itself.

This Thesis has been accepted for inclusion in UNLV Theses, Dissertations, Professional Papers, and Capstones by an authorized administrator of Digital Scholarship@UNLV. For more information, please contact digitalscholarship@unlv.edu.

NEW INSIGHTS INTO THE DIVERSE INTRAPLATE VOLCANISM PRESENT
WITHIN THE HOWLAND AND BAKER ISLAND UNITED STATES
EXCLUSIVE ECONOMIC ZONE

By

Nicholas Foresta

Bachelor of Science – Geology
University of Nevada, Las Vegas
2022

A thesis submitted in partial fulfillment
of the requirements for the

Master of Science – Geoscience

Department of Geoscience
College of Sciences
The Graduate College

University of Nevada, Las Vegas
August 2024



Thesis Approval

The Graduate College
The University of Nevada, Las Vegas

July 8, 2024

This thesis prepared by

Nicholas Foresta

entitled

New Insights into the Diverse Intraplate Volcanism Present within the Howland and Baker Island United States Exclusive Economic Zone

is approved in partial fulfillment of the requirements for the degree of

Master of Science - Geoscience
Department of Geoscience

Kevin Konard, Ph.D.
Examination Committee Chair

Arya Udry, Ph.D.
Examination Committee Member

Andrew Martin, Ph.D.
Examination Committee Member

Aude Picard, Ph.D.
Graduate College Faculty Representative

Alyssa Crittenden, Ph.D.
*Vice Provost for Graduate Education &
Dean of the Graduate College*

Abstract

The origin of oceanic volcanism has been attributed to various mechanisms, such as upwelling mantle plumes, lithospheric extension driven decompression melting, and small-scale convective cells in the asthenosphere. Discovering the range of magmatic drivers present in the ocean basins aids in understanding mantle geodynamics and tectonic processes. A recent seafloor exploration campaign within the Howland and Baker Island (HBI) U.S. Exclusive Economic Zone (EEZ; approximately near the equator and the International Date Line) resulted in the collection of multiple lava flow samples, which offer valuable insights into the complex origins and dynamics of intraplate seamounts. According to current absolute plate motion (APM) models, the seamounts and islands that compose part of the HBI, as well as the Tokelau Seamount Chain to the south, was sourced by the long-lived Macdonald hotspot during the Late Cretaceous. This study utilizes new high precision $^{40}\text{Ar}/^{39}\text{Ar}$ age determinations, along with whole rock major and trace element analyses from previously unexplored seamounts, which help elucidate the volcanic history of the HBI EEZ during the Cretaceous.

Three major age groups, each with their own geodynamic origins, are observed in the HBI EEZ. The new age data confirms a linear age progression at Howland Island (73.75 ± 0.28 Ma) and Titov Ridge (71.41 ± 0.23 Ma) aligning with the projected Macdonald hotspot track. The Unnamed Seamount 2 (85.61 ± 0.14 Ma) west of Howland Island (around 1.0°N , 179.3°E), does not fit the expected age or geometry of the Macdonald hotspot track. The origin of this seamount and neighboring Unnamed Seamount 3 remains enigmatic but may represent a pulse of plume melt channelization or similar anomalous short-lived volcanic activity. The oldest pulse of regional volcanism are tephra deposits (124.17 ± 0.12 Ma; 124.22 ± 0.13 Ma) from Unnamed Seamount 1 (around 3.9°N , 176.3°W). The deposits do not have chemistry consistent with

mantle plume volcanism (i.e., deep melting and enriched reservoir rare earth element ratios) and are likely related either to the emplacement of the massive Ontong Java Plateau large igneous province on the Pacific basin at that time, or to plate deformation resulting from the adherence of the Magellan microplate onto the Pacific. These chemical and chronological findings from previously unexplored seamounts support the notion of the Macdonald Hotspot's long-term activity extending to the Late Cretaceous and provide new perspectives on the variety of intraplate volcanism in oceanic basins.

Acknowledgments

I would like to extend my deepest gratitude to the entire UNLV staff for providing an exceptional educational environment and a supportive workplace. Your dedication and hard work have been instrumental in my academic journey.

I am immensely thankful to both the current and former graduate students for their unwavering support throughout this research. In particular, I would like to acknowledge Amber Ciravolo, Debbie Morales, Sierra Ramsey, and Brandon Scott for their invaluable assistance and encouragement.

My heartfelt thanks go to my committee members – Dr. Andrew Martin, Dr. Arya Udry, and Dr. Aude Picard – for their dedication and time in being a part of this project. A special mention goes to Dr. Shichun Huang, who provided me with my initial opportunity to work in a laboratory, sparking my interest in research. Additionally, I would like to express my profound gratitude to Dr. Kevin Konrad for his outstanding support and guidance as my academic advisor.

Lastly, I am deeply grateful to my friends and family for their constant support and encouragement. A special thanks to my mother for her endless support, which has been a pillar of strength throughout my academic endeavors. Thank you all for your contributions throughout the past two years of this project. I will forever be appreciative of your support.

Table of Contents

Abstract.....	iii
Acknowledgments	v
Table of Contents	vi
List of Tables.....	viii
List of Figures.....	ix
Chapter 1: Introduction	1
1.1 Background	1
1.2 Mantle plume dynamics	1
1.3 Macdonald hotspot reconstruction.....	9
Chapter 2: Methodology.....	15
2.1 Sample collection.....	15
2.2 Major and trace element geochemistry methodology.....	17
2.3 $^{40}\text{Ar}/^{39}\text{Ar}$ geochronology methodology	17
Chapter 3: Results.....	22
3.1 Seamount descriptions.....	22
3.2 Major element geochemistry.....	34
3.3 Trace element geochemistry	37

3.4 $^{40}\text{Ar}/^{39}\text{Ar}$ geochronology	43
Chapter 4: Discussion	49
Chapter 5: The Surface Expression of the Macdonald Hotspot from Cretaceous to Modern Day.....	63
5.1 Plume and age progressions within the Cook-Austral Islands	63
5.2 Linking old to young Macdonald (Tokelau Ridge)	66
5.3 Howland and Baker Island EEZ interpretations	69
5.4 Relative Pacific Plume motion	73
Chapter 6: On the Origin of Barremian-aged Felsic Volcanism in the Howland and Baker Island Region.....	79
Chapter 7: Summary and Conclusions	84
Appendices.....	86
Appendix A: $^{40}\text{Ar}/^{39}\text{Ar}$ results from incremental heating experiments.....	86
References	93
Curriculum Vitae	108

List of Tables

Table 1: Lava flow location metadata for samples used in this study.....	16
Table 2: Major element oxides of selected samples reported as weight percent (wt. %) normalized to 100% totals	35
Table 3: Whole rock trace element concentrations of selected samples reported in ppm.....	38
Table 4: Whole rock trace element concentrations of selected samples reported in ppm.....	39
Table 5: $^{40}\text{Ar}/^{39}\text{Ar}$ age determination incremental heating experiments summary from samples recovered from FK210605.....	45

List of Figures

Figure 1: Schematic of the Earth’s interior showing plate boundaries and associated mantle processes unmodified from Koppers et al. (2021).....	3
Figure 2: Schematic of radiogenic Sr-Nd-Pb endmember components for mantle-derived basalt unmodified from Hart et al. (1992).....	6
Figure 3: Regional map of the South Pacific highlighting prominent geologic features and Pacific plate movement relative to fixed hotspots	10
Figure 4: Regional map of the South Pacific highlighting age progressions of hotspots originating from the Cook-Austral Islands.....	11
Figure 5: Map of the Howland and Baker Island EEZ study area	14
Figure 6: Hand samples images of representative core material gathered from seamounts during the FK210605 research cruise expedition.....	20
Figure 7: Representative XPL thin section images of sample phenocrysts and alteration effects from FK210605 and NA112	21
Figure 8: Colored bathymetry map lines of Swains Island and all sample locations collected from NA112 (NA112-001, -002, -003, -004, -005, -006, -008)	23
Figure 9: Colored bathymetry map of Howland Island	25
Figure 10: Colored bathymetry map of Unnamed Seamount 1	27
Figure 11: Colored bathymetry map of Unnamed Seamount 2 and Unnamed Seamount 3.....	29
Figure 12: Colored bathymetry map of Titov Ridge.....	31
Figure 13: Colored bathymetry map of Lelei	33
Figure 14: Total alkali silica chemical classification diagram for volcanic rocks (Bas et. al, 1987).	36

Figure 15: Trace element diagram normalized to primitive upper mantle values (Sun and McDonough, 1989) displaying three geochemical trends	40
Figure 16: REE diagram illustrating enrichment patterns of lava flow samples	42
Figure 17: Map of the Howland and Baker Island EEZ with new $^{40}\text{Ar}/^{39}\text{Ar}$ age determinations outlined in grey boxes	46
Figure 18: Age determinations and inverse isochron results from incremental $^{40}\text{Ar}/^{39}\text{Ar}$ heating experiments	47
Figure 19: Age determinations and inverse isochron results from incremental $^{40}\text{Ar}/^{39}\text{Ar}$ heating experiments	48
Figure 20: Scatter plots illustrating the effects of seawater alteration on whole rock chemistry.	51
Figure 21: Y/Y* plots illustrating phosphorization effects on lava flow samples in red markings.	52
Figure 22: Depth of melting and degree of melting fractionation trends of HREEs and LREEs for the Swains Island and the Howland and Baker Island EEZ seamounts using the $(\text{Dy}/\text{Yb})_{\text{PM}}$ vs. $(\text{La}/\text{Sm})_{\text{PM}}$ system	54
Figure 23: Linear discrimination analysis of ocean basalt fields and a first order classification for categorizing seamounts	55
Figure 24: Th/Yb and Nb/Yb ratios compared to MORB and OIB arrays	57
Figure 25: Regional map of the Cook-Austral Islands	64
Figure 26: Regional map of the Tokelau Islands and nearby geographic features	67
Figure 27: Age distance plot of seamounts suspected to originate from the Macdonald hotspot.	71
Figure 28: Map of the South Pacific illustrating the hot spotting analytical technique (Wessel and Kroenke, 1998)	72

Figure 29: Map of potential long-lived hotspots in the South Pacific	77
Figure 30: Calculated distances between hotspots as a function of time interpolated model with error bars	78
Figure 31: Bathymetric map of Magellan Rise and surrounding area	81
Figure 32: Reconstruction of the Pacific plate with various LIPs <i>ca.</i> 124 Ma	82

Chapter 1: Introduction

1.1 Background

Plate tectonic theory imparts a foundation for interpreting volcanism at plate boundaries (Wilson, 1965). Mantle convection has long been thought to be the driving force of plate tectonics, in which cold, dense subducted lithosphere is recycled into the mantle and new lithosphere is produced via decompression melting at mid-ocean ridges. However, the origin of volcanoes sourced far from plate boundaries cannot be readily explained by convergent or divergent processes that occur at the margins of tectonic plates. An early explanation that is compatible with plate tectonics is that plumes deep beneath the Earth's surface form through processes other than upper mantle convection (Wilson, 1963). Morgan (1972) suggested oceanic intraplate volcanism is sourced by upwelling mantle plumes rooted deep in the lower mantle that are fixed with respect to the overlying lithosphere. Since then, significant research has been conducted into understanding the interplay between geodynamic processes, plate motion and intra-plate volcanism, much of which remains unresolved (e.g., Koppers et al., 2021). For example, current best fit geophysical models for Earth's interior involve either whole mantle convection (e.g. Vankeken and Ballentine, 1998) or two convective regimes (whole mantle + upper mantle) (e.g., van der Hilst et al., 1997; Bercovici and Karato, 2003). Provided that the Earth's deep interior cannot be directly sampled, observations of surface features need to be inverted to better understand the complex underlying geodynamic processes.

1.2 Mantle plume dynamics

Understanding the physical and chemical properties of mantle plumes, as well as the mantle source reservoirs they interact with, is vital for deconvolving the evolution of terrestrial planetary bodies. Current models that incorporate a range of interdisciplinary observations (e.g., age

determination experiments, surficial geochemical mantle tracers, geophysical modeling) suggest that plumes are narrow rising columns driven by a combination of thermal and compositional buoyancy that ascend from the deep mantle towards the Earth's surface (e.g., Koppers et al., 2021). Seismic imaging indicates an anomalous structure exists near the core-mantle boundary, where slow shear wave velocities record the presence of large geoid perturbations (Dziewonski and Woodhouse, 1987; Garnero et al., 2016). These perturbations have been designated as the large low-shear velocity province (LLSVP) and are thought to produce upwelling chemically heterogeneous diapirs, driven by thermal buoyancy, thus providing a model for deeply sourced plume production (Burke, 2011; Koppers et al., 2021; Figure 1). The surface expressions of hotspots, which represent the shallow melting regime of mantle plumes via decompression melting, correlate to the edges of LLSVPs, indicating that plumes likely initiate on the steep flanks of LLSVPs (Burke et al., 2008). While the origin of LLSVPs is still debated, it has been suggested that they are remnants of ancient subducted lithosphere (van der Hilst et al., 1997) or crystal cumulate residues of an early magma ocean (Brown et al., 2014).

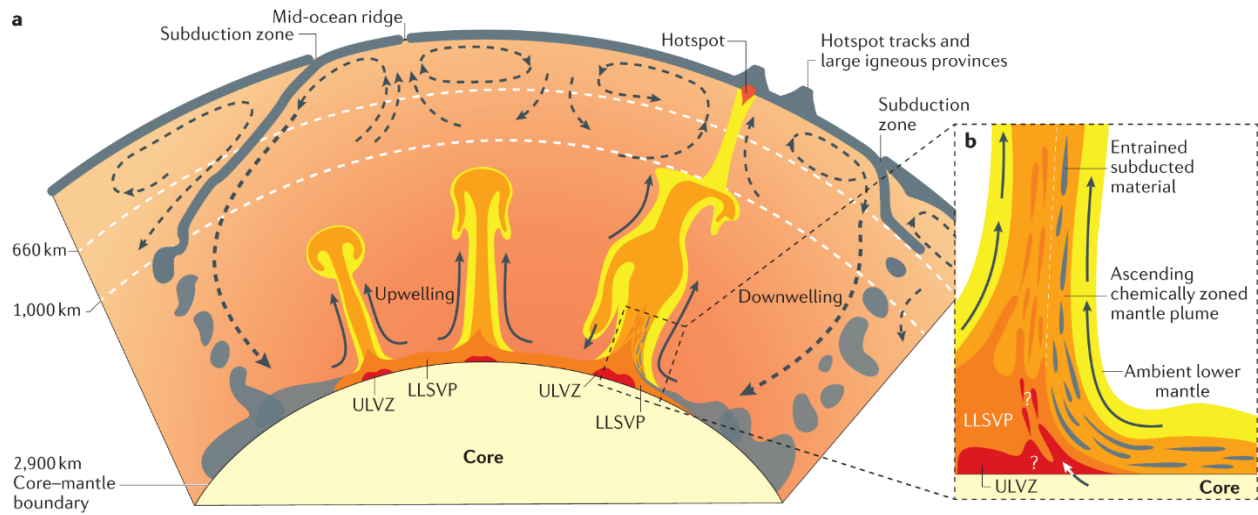


Figure 1: Schematic of the Earth's interior showing plate boundaries and associated mantle processes unmodified from Koppers et al. (2021). Subducted slabs accumulate near the core at a large-low-shear velocity province (LLSVP) which may provide subducted materials to the rising plume. Mineralogical phase changes and a corresponding density contrast at 1000 km discontinuity accounts for apparent pooling of the rising conduits. Entrained material may provide the chemical signatures that differentiate OIB from MORB, suggesting a possible connection between subducted plates and mantle plumes.

In order to study mantle plume dynamics, it is essential to analyze the geochemical features of samples obtained from surface expressions of plumes, such as hotspot volcanism (as proposed by Morgan, 1972; Duncan and Clague, 1985; Staudigel et al., 1991; Koppers et al., 2021). Hotspot volcanic products contain distinctive chemical and isotopic signatures that have been interpreted as originating from discrete mantle reservoirs (Hofmann, 2007). Observations of significant source mantle heterogeneity may shed light on the complex interplay of deep mantle plumes and ancient subducted oceanic lithosphere (e.g., Hofmann and White 1982). Ocean island basalts (OIB), that are commonly produced from decompressional melting of upwelling plumes, are geochemically distinct lava flows typically unaffected by crustal contamination (e.g., Hofmann, 2007). Unlike the trace-element depleted lavas that produce mid-ocean ridge basalts (MORB) at divergent plate boundaries, OIBs are relatively more enriched in incompatible elements (i.e., U, Th, Pb) that preferentially partition into the melt during partial mantle melting, suggesting distinct but different mantle reservoirs for MORB and OIBs (e.g., Hofmann and White, 1982). In addition to major and trace element chemistry, isotopic signatures of OIBs reveal further evidence of mantle heterogeneity, including end-member Sr-Nd-Pb isotopic compositions representative of idealized source mantle domains (Zindler and Hart, 1986). The domains include the depleted MORB mantle (DMM), HIMU (high μ or [U-Th]/Pb), enriched mantle I (EMI) and enriched mantle II (EMII; Figure 2). The origins of the HIMU, EMI, and EMII endmember signatures are still debated, largely due to the difficulties in using isotopic compositions to constrain geodynamic models (see Weis et al., 2023, for a recent review). However, it is generally accepted that they are the result of mixing between the Earth's variably depleted ambient mantle (i.e., background mantle that constitutes the bulk of the Earth's mantle) and recycled subducted oceanic lithosphere (HIMU), lower continental crust or marine carbonates (EMI), and/or upper continental crustal material

(EMII) (Hart et al., 1992; Stracke et al., 2005; Hofmann, 2007). Isotopic diversity between endmembers is best illustrated by a mixing tetrahedron (Figure 2; Hart et al., 1992) with mixing arrays extending towards a shared, undifferentiated focal reservoir (FOZO). Other non-endmember reservoirs have also been proposed by Zindler and Hart (1986) including a prevalent mantle (PREMA) representing a large homogeneous mantle source that has undergone mixing over time, and bulk silicate earth (BSE) from which the silicate mantle and crust are separated from the iron core and examined as an average isotopic composition. Understanding where these different chemical reservoirs correlate to Earth's deep interior requires a combination of geochemical and geophysical observations. Identifying the nature of these geochemically and isotopically distinct mantle reservoirs can potentially be inferred by tracing the history of long-lived, isotopically distinct hotspots.

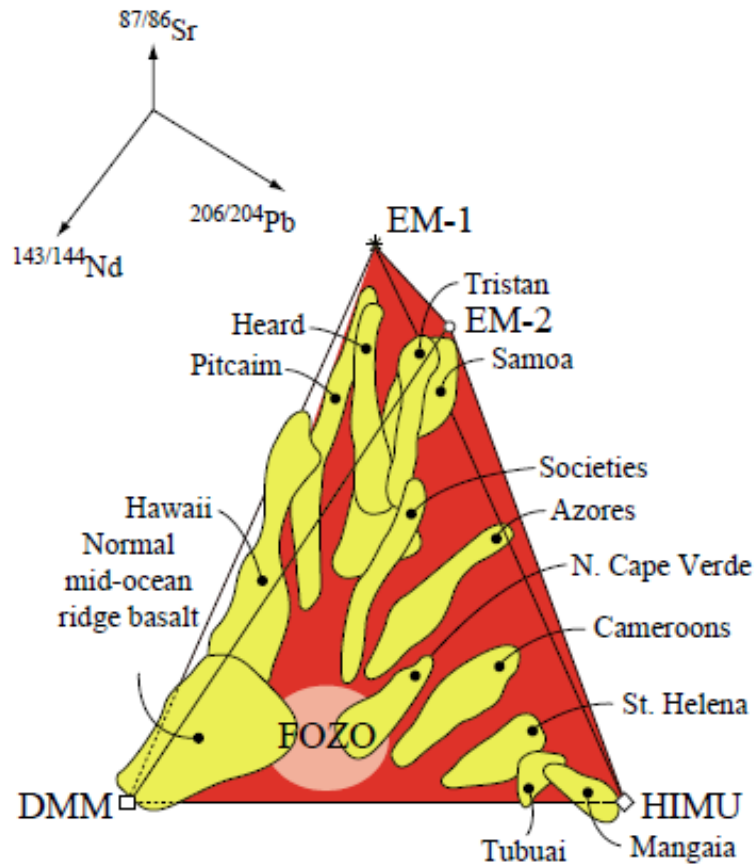


Figure 2: Schematic of radiogenic Sr-Nd-Pb endmember components for mantle-derived basalt unmodified from Hart et al. (1992). Binary mixing arrays stem from a hypothesized central focal zone (FOZO) that represents a primitive lower mantle mixing component. Depleted mantle material (DMM), enriched mantle I (EMI), enriched mantle II (EMII), and high μ (HIMU) represent endmember compositions.

Hotspot tracks are age-progressive surficial features on the oceanic lithosphere that provide unique insights into mantle plume dynamics (Morgan, 1972). The movement of tectonic plates over stationary mantle plumes can leave a trail of volcanic features, such as seamounts and island chains, that have been used as a record of ancient plate motions (Duncan and Clague, 1985; Wessel and Kroenke, 2008). Resolving absolute plate motion (APM) models requires a fixed reference frame, such a stable fixed mantle plume or a plume that moves at a significantly lower rate than plate motion. Therefore, understanding the stability of mantle plumes rising through the mantle, or lack thereof, is central to understanding the nature of plate motions, as well as mantle convection.

The Pacific Basin contains a number of hotspot tracks that provide the necessary reference frames for resolving paleo plate motion. Furthermore, long-lived hotspots, such as the Hawaiian-Emperor and Louisville chains, provide additional data points that allow APM to extend further back in time. The 80 Ma history of age progressive seamounts that comprise the Hawaiian-Emperor chain suggest they formed from a single hotspot and can be used to document plate motion history (Duncan and Clague, 1985). However, the surface manifestation of some plumes are not continuous with some hotspots tracks indicating long-lived mantle anomalies (>20 Ma), while others are short-lived (<20 Ma) (Courtilot et al., 2003). The number of mantle plumes that are long-lived or short-lived remains unresolved, yet growing evidence suggest that many plumes commonly exist for over 100 m.y. (Coffin, 2002; Konter et al., 2008; Hoernle et al., 2015; Koppers et al., 2021). In order to map the history of an individual hotspot, the “isotopic fingerprinting” technique is typically employed, wherein the isotopic composition of a seamount’s lava flows are combined with age-progressions to track the history of hotspots in regions that contain overlapping tracks (Konter et al., 2008; Jackson et al., 2010). Once mapped, the resulting hotspot tracks can be

used to refine models of plate motion, independent plume motion and plume buoyancy flux through time.

Since Morgan (1972) proposed a kinematic model in which the Hawaiian-Emperor bend (HEB) was attributed to lithospheric plate motion moving over a fixed mantle hotspot, growing evidence of independent mantle plume motion has complicated their use for APM modeling (Steinberger and O'Connell, 1998). Paleolatitudes derived from paleomagnetic analyses of deeply drilled cores extracted from several Emperor seamounts revealed a southward drift of the Hawaiian plume during the Cretaceous (Tarduno et al., 2003; Bono et al., 2019). Hawaiian plume motion has also been suggested by geodynamic modeling that requires a combination of hotspot motion (Steinberger et al., 2004) and a significant change in Pacific plate motion to account for the formation of the Emperor seamount track and the HEB (Torsvik et al., 2017). Modeling the relationship between multiple hotspot tracks present on the same plate is another effective method for interpreting plume motion. Konrad et al. (2018) calculated interpolated great circle age-distances between the Hawaii, Louisville and Rurutu-Arago plumes, finding a large plume divergence from 60 to 48 Ma, consistent with a fast-moving Hawaiian plume at that time.

Although the mantle plume model has been the prevalent explanation for most intraplate volcanism for the past 50 years (Koppers, 2011), other models have been put forth to explain the volcanic expressions. Alternative hypotheses for intraplate volcanism suggest a plate tectonics origin (i.e., stress and cracks in the lithosphere) interpreted from upper mantle thermal variations (e.g., Anderson, 2000) or a mantle transition zone origin for hotspots (Anderson and Natland, 2014). These observations often fail to successfully address age-progressive seamount chains, which are indicative of plate motion, as well as key isotopic characteristics of OIBs, such as primitive noble gas signatures (Mukhopadhyay and Parai, 2019). Here we use a combination of

age determination experiments coupled with whole rock major and trace element analyses to better understand the underlying drivers of intraplate age progressive volcanic chains.

1.3 Macdonald hotspot reconstruction

One potentially long-lived hotspot with a relatively poorly defined history is the Macdonald hotspot. The active Macdonald hotspot is positioned in the complex Cook-Austral Islands in the South Pacific Ocean (Figure 3). Though the origin of the Cook-Austral chain remains contentious, recent work attributes the seamounts and islands primarily to plume-related activity (Konter et al., 2008; Konrad et al., 2018; Rose and Koppers, 2019). Current APM models coupled with published age determinations predict the Macdonald hotspot was partially the source of multiple seamounts in the South Pacific (Figure 4; Koppers et al., 2007; Konter et al., 2008; Wessel and Kroenke, 2008; Rose and Koppers, 2019). The Macdonald hotspot contains distinctive HIMU mantle endmember isotopic signatures (Woodhead, 1996) and has a debated lifespan, with some studies arguing it only extends back to Mangaia Island in the western Cook-Austral chain (20 Ma; Figure 3; Turner and Jarrard, 1982), while others attest for a late Cretaceous extent in the Tokelau Seamount Chain (70 Ma; Figure 4; Konter et al., 2008; Buff et al., 2021).

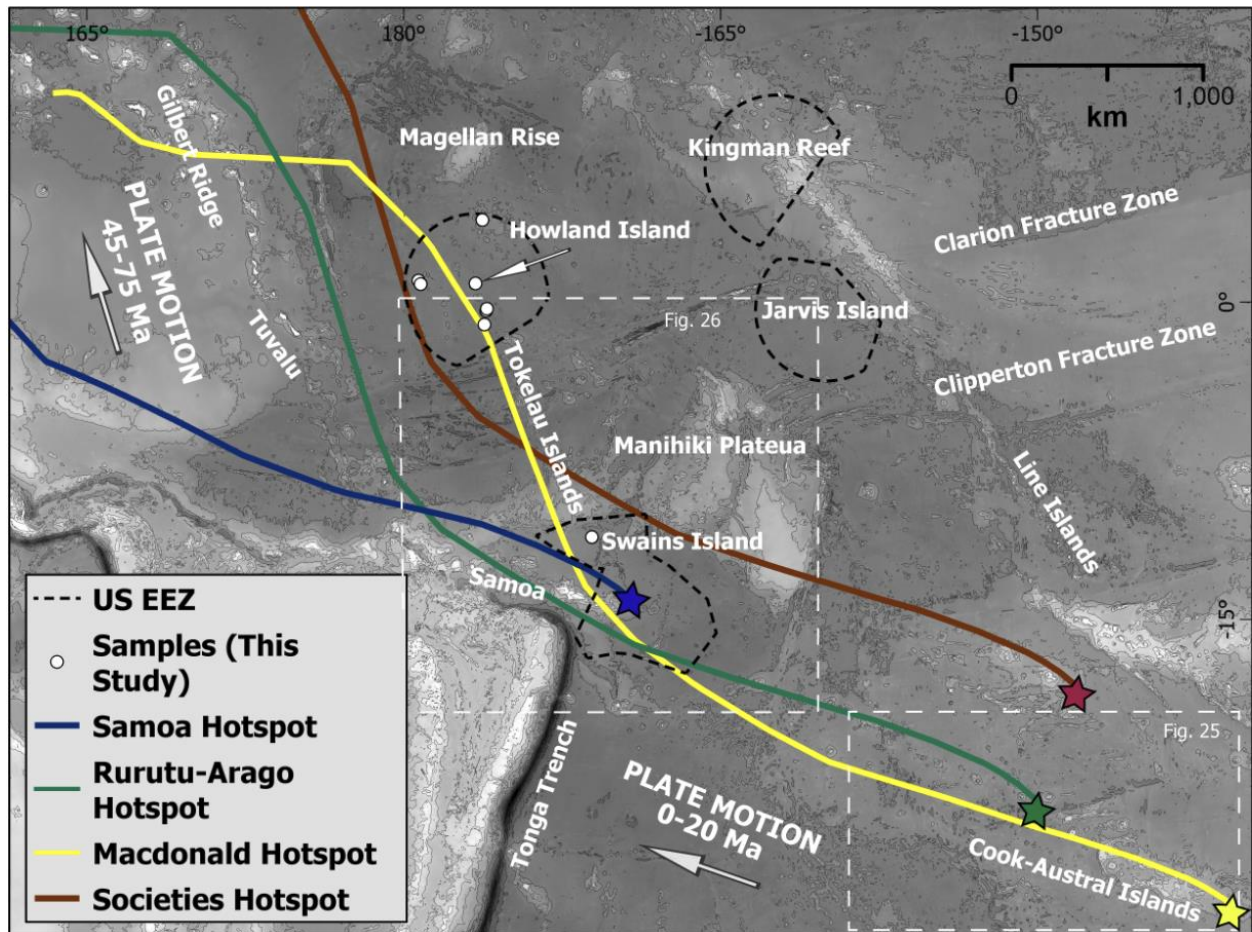


Figure 3: Regional map of the South Pacific highlighting prominent geologic features and Pacific plate movement relative to fixed hotspots. Plate reconstruction follows pole rotations of the WK08-A plate motion model (Wessel and Kroenke, 2008). Hotspot tracks are modeled interpreted reconstructions of plate movement from 120 Ma to the present. Modeled hotspot reconstructions are colored by individual hotspots found in the region and stars indicate their current eruptions sites.

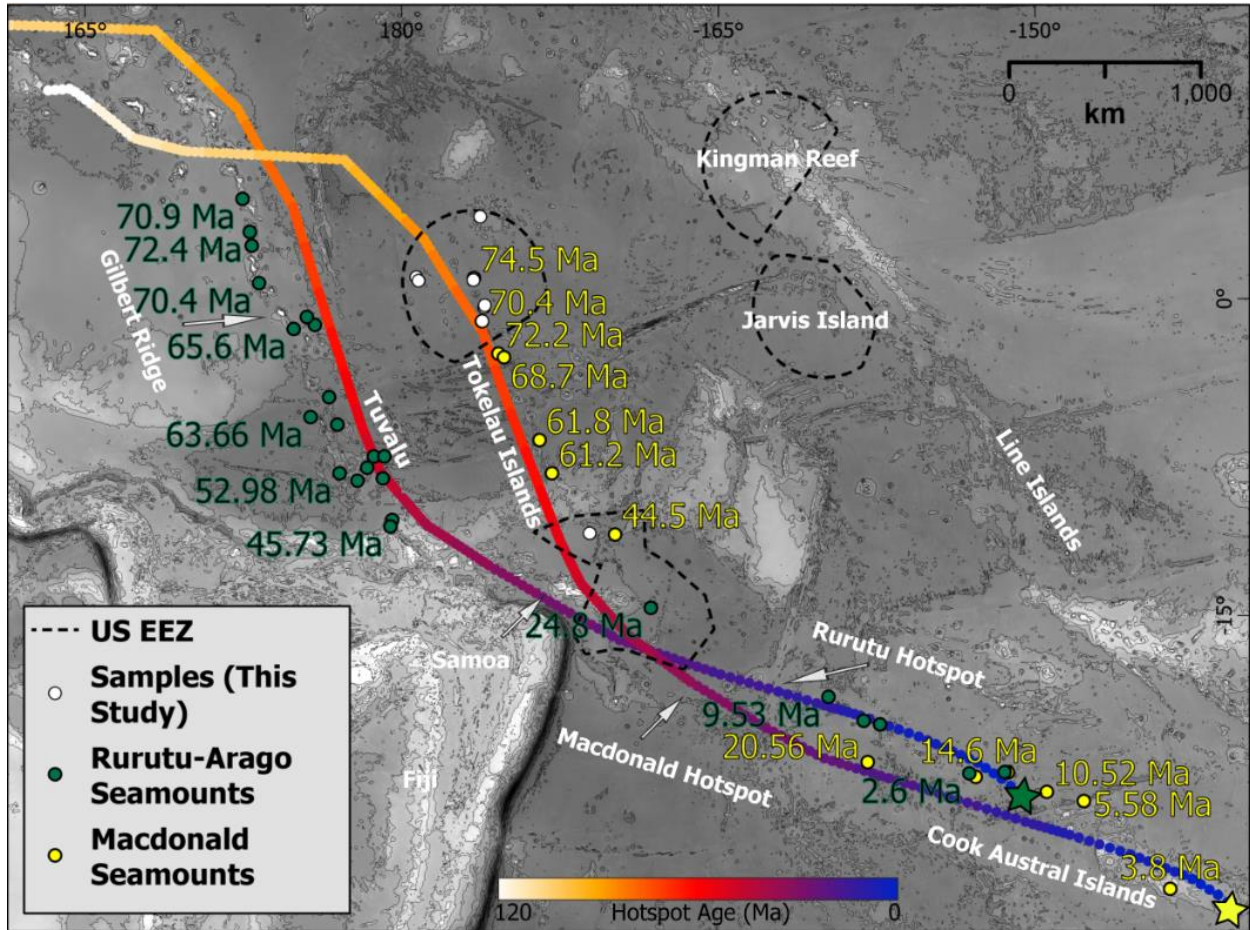


Figure 4: Regional map of the South Pacific highlighting age progressions of hotspots originating from the Cook-Austral Islands. Yellow circles and labels are published age determinations thought to represent the Macdonald hotspot and green circles and labels are ages thought to represent the Rurutu-Arago hotspot. Plate reconstruction follows pole rotations of the WK08-A plate motion model (Wessel and Kroenke, 2008). Hotspot tracks are interpolated reconstructions of plate movement from 120 Ma to the present. Active volcanism is present at the Macdonald Seamount and Arago Seamount highlighted by the yellow and green stars, respectively.

This study contributes to the discussions on the long-lived nature of the Cook-Austral hotspots by investigating the genesis of undated lava flows suspected to originate from the Macdonald hotspot (Figure 3). Fingerprinting seamounts through their chemical compositions and age determinations will provide additional insight regarding the lifespan of mantle plumes and the dynamics of the HIMU reservoir. If the Macdonald plume is truly long-lived, it will provide an additional reference frame for plate reconstructions and plume dynamics. This work focuses on newly acquired submarine rock samples from poorly explored U.S. territories that are suspected to originate from the Macdonald hotspot. The following sample areas are located within the Samoa unit and Howland and Baker Islands (HBI) unit of the U.S. Exclusive Economic Zone (EEZ) (Figure 3). In addition to better understanding the geological processes that led to the formation of various seamounts and islands, exploring the EEZ will ultimately help us better preserve and maintain the natural resources of those areas.

Swains Island (11°07' S, 171°05' W), an undated atoll west of the Manihiki Plateau and northeast of Samoa, may provide additional insight regarding the longevity of the Macdonald plume (Figure 3). Swains Island and the surrounding area is a national wildlife preserve that is located within the United States EEZ and encompass 135.5 km² of a preserved marine sanctuary. Newly acquired submarine basaltic lava flow samples from the flanks of Swains Island will assist in unravelling its enigmatic origin and whether it is related to Eocene magmatism of the Macdonald plume or another unknown source.

Howland and Baker Islands are U.S. territories within the EEZ that coincides with a unit of the Pacific Remote Island Marine National Monument (PRIMNM; Figure 5). The HBI EEZ contains the northern reaches of the Tokelau Chain, and thus may hold clues to the oldest available Macdonald plume volcanics (Konter et al., 2008). Numerous seamounts in these zones have never

been sampled for geologic context. Furthermore, the region is lacking in high-resolution maps that require modern sonar techniques (e.g., side-scan sonar, multi-beam sonar) only obtainable from seafaring vessels. Therefore, in addition to addressing first-order questions on plume longevity and seamount genesis, this work will continue on efforts to map U.S. seafloor territory in the Pacific by producing geologic and high-resolution (100 m) bathymetry maps using recently published datasets. The findings of this study will test the hypothesis that the Macdonald hotspot connects and extends from the late Cretaceous Tokelau Islands to the active Macdonald seamount.

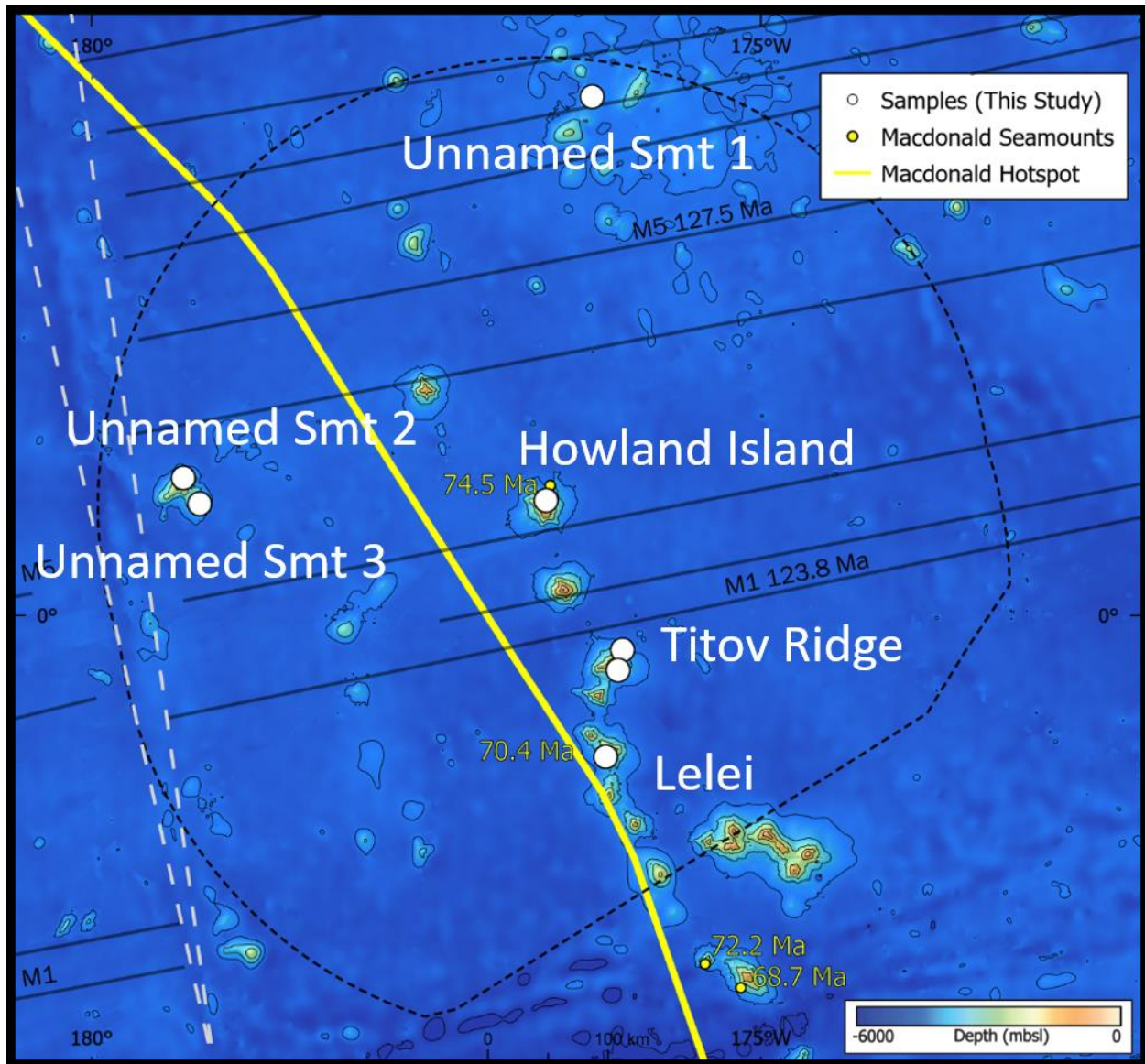


Figure 5: Map of the Howland and Baker Island EEZ study area. Yellow labels are previously published ages from Koppers et al. (2007). Black lines represent seafloor magnetic anomalies. M1 highlights the beginning of the Cretaceous Normal Superchron and corresponding seafloor ages. The dashed white line is the Central Pacific Fracture Zone (Nakanishi et al., 1992).

Chapter 2: Methodology

2.1 Sample collection

Samples for this project were collected on two research expeditions (Table 1). This research uses samples retrieved from Swains Island that were gathered by the Ocean Exploration Trust's cruise NA112 in 2019 aboard the *E/V Nautilus*. Samples from NA112 were picked individually using the *Hercules* remote operating vehicle (ROV) along the southern flanks of Swains Island. Additional samples were picked from the ROV *SuBastion* onboard the *R/V Falkor* during the 2021 FK210605 expedition. These expeditions mapped the U.S. EEZ within the America Samoa and HBI regions, respectively. Here we focus on seven samples collected from Swains Island during the NA112 cruise and ten samples from six seamounts in the HBI EEZ from FK210605.

The samples shown in Figure 6 are aphanitic mafic rocks with variable amounts of secondary alteration from seawater alteration. Figure 6A and 6B exhibit tephra-like morphologies. Amygdule precipitation in the formation of calcite and zeolite was observed in most samples (e.g., Figure 6D; 6E) as well as unfilled vesicles (Figure 6G). Phosphorite veins were apparent in some samples as well (Figure 6J). Finally, all samples were covered with variable (~1-4 mm) FeMn veneers. Representative thin section images revealed the presence of feldspars (Figure 7A; 7B; 7C). Amphiboles were present in two samples (Figure 7E, 7G). Altered groundmass was abundant in many samples leading to difficulties identifying mineral phases (Figure 7D). Other evidence of alteration, including phosphorite veins (Figure 7F) and zeolites (Figure 7H) were also present in samples.

Table 1: Lava flow location metadata for samples used in this study. Mbsl = meters below sea level

Sample ID	Seamount	Latitude	Longitude	Depth (mbsl)
NA112-001	Swains Island	-11.1175	-171.0896	2436
NA112-002	Swains Island	-11.1174	-171.0900	2432
NA112-003	Swains Island	-11.1171	-171.0906	2415
NA112-004	Swains Island	-11.1169	-171.0908	2415
NA112-005	Swains Island	-11.1148	-171.0902	2205
NA112-006	Swains Island	-11.1123	-171.0909	2078
NA112-008	Swains Island	-11.1108	-171.0916	1977
FK210605-072	Unnamed Seamount 1	3.8798	-176.2743	2596
FK210605-080	Unnamed Seamount 1	3.8806	-176.2751	2497
FK210605-138	Howland Island	0.8791	-176.5988	1787
FK210605-304	Unnamed Seamount 2	1.0136	-179.2987	2012
FK210605-307	Unnamed Seamount 2	1.0130	-179.3007	1858
FK210605-338	Unnamed Seamount 3	0.8503	-179.1944	2175
FK210605-353	Unnamed Seamount 3	0.8477	-179.1980	1831
FK210605-372	Titov Ridge	-0.4104	-176.0908	1564
FK210605-397	Titov Ridge	-0.3172	-176.0607	1893
FK210605-428	Lelei	-1.0644	-176.1783	2987

2.2 Major and trace element geochemistry methodology

Fifteen samples were selected for whole rock major element geochemical analysis. These rocks were chosen based on the availability of material and the lowest degree of visible degree of alteration. Five representative samples from Swains Island (NA112-001, -002, -003, -005, -008) were cut into small, ~100 g pucks for major and trace element analyses. Secondary alteration, including ferromanganese (FeMn) crusts and secondary phosphorite veins were avoided, when possible, to circumvent generating sampling bias in the data. Following a thorough abrasion process using aluminum oxide sandpaper sheets to remove potential embedded metal from the trim saw, samples were repeatedly sonicated in deionized water to remove residual dust. The pucks were broken into smaller pieces with a hammer in plastic bags to avoid metal contamination. An agate-lined Fritsch Pulverisette mortar and pestle ground the fragments into fine powders. Geochemical analyses of Swains Island were originally planned to be carried out at UNLV, but the samples, along with those from FK201605, were eventually outsourced due to staff relocations. The ten samples from FK201605 underwent similar trimming (without crushing and pulverizing) into ~50 g representative pucks. The samples were polished to remove saw marks and sonicated to remove residual polishing powder. The five powders and ten pucks were sent to the Michigan State University's XRF and ICP-MS laboratories to be analyzed. Following the methodology of Rooney et al. (2011; 2015), major and trace element triplicates were analyzed from XRF and solution ICP-MS, respectively.

2.3 $^{40}\text{Ar}/^{39}\text{Ar}$ geochronology methodology

Petrographic examinations of the collected igneous rocks prior to sample preparation aided in determining which samples are appropriate for collecting age determinations. Traditional mineral phases for $^{40}\text{Ar}/^{39}\text{Ar}$ geochronology were targeted when available (i.e., sanidine,

plagioclase, amphibole). Due to the remoteness of the study area, very few samples were available for experimental analysis and other non-traditional phases (i.e., clinopyroxenes) were sometimes selected instead. All samples from Swains Island (NA112) do not contain any traditional phases visible in thin sections and were targeted for clinopyroxene-bearing phenocrysts following Konrad et al. (2019). Separates for $^{40}\text{Ar}/^{39}\text{Ar}$ age determination experiments were generated from ten samples from FK210605 including, five plagioclase, two sanidine, two amphibole, and one clinopyroxene separate, as well as seven clinopyroxene separates from NA112 lava flows.

The bulk rocks were reduced in size using a BICO steel jaw chipmunk rock crusher followed by grinding in a BICO rotary disk mill. Phenocryst separates were targeted at a specific size, typically between 200-425 μm . After sieving the crushate to the desired grain size, samples were immersed in deionized water and stimulated in an ultrasonic bath to remove fine-grained dust particles. Several washing iterations (4-7 dependent on sample necessity) were undertaken per sample, proceeded by oven drying at 50 °C for up to 48 hours. A Frantz isodynamic magnetic separator was utilized to separate desirable concentrations from the more magnetic groundmass. The crushate was subjected to a successive acid leaching procedure, wherein material was submerged in various acids for one-hour 40 °C ultrasonic baths. Following Konrad et al. (2018), acid leaching included 3N HCl, 6N HCl, 1N HNO₃, and 3N HNO₃ in sixty minutes iterations to remove secondary clays and carbonates from the samples. The feldspar separates were subjected to an additional 4% HF sonicated bath for 15 minutes to remove any potential sericite rims. Following leaching, separates were rinsed and sonicated in deionized water and oven dried. A meticulous picking process under a microscope removed any remaining impurities and inclusion-laden grains. Samples were packed into aluminum packets and inserted into pure quartz tubes

along with known Fish Canyon Tuff sanidine fluence monitors. Packing heights were measured and sent to the Oregon State University's TRIGA reactor to undergo irradiation for nine hours.

Analyses were carried out using the incremental heating method at the Nevada Isotope Geochronology Laboratory (NIGL) with a double-vacuum furnace connected to a stainless-steel extraction line. Samples were dropped into the crucible at 400 °C to remove adhered atmospheric gas. The crucible was held at a given temperature for fourteen-minutes while the released gases were exposed to a hot SAES 'getter'. Then the furnace temperature was set back to 400 °C and the gas was subjected to an additional six-minute exposure to a second set of room temperature and hot SAES getters. The processed gas was then introduced into a NGX multi-collector noble gas mass spectrometer with ATONA amplifiers, with time zero being initiated after a twenty second gas equilibration period. The 40, 39, 38, 37, and 36 masses were analyzed and regressed following the procedures outlined in Balbas et al. (2023). Age determinations were computed using the ArArCalc software (Koppers, 2002), incorporating the propagated uncertainties as described in Balbas et al. (2023). The ages were calculated against a Fish Canyon Tuff sanidine fluence monitor, assuming an age of 28.201 ± 0.08 Ma (Kuiper et al., 2008), and utilizing a ^{40}K total decay constant of $5.530 \pm 0.097 \times 10^{-10} \text{ yr}^{-1}$ (Min et al., 2000). Additionally, existing literature $^{40}\text{Ar}/^{39}\text{Ar}$ age determinations were recalculated using the same fluence monitor age and updated Min et al., (2000) decay constant, when necessary.

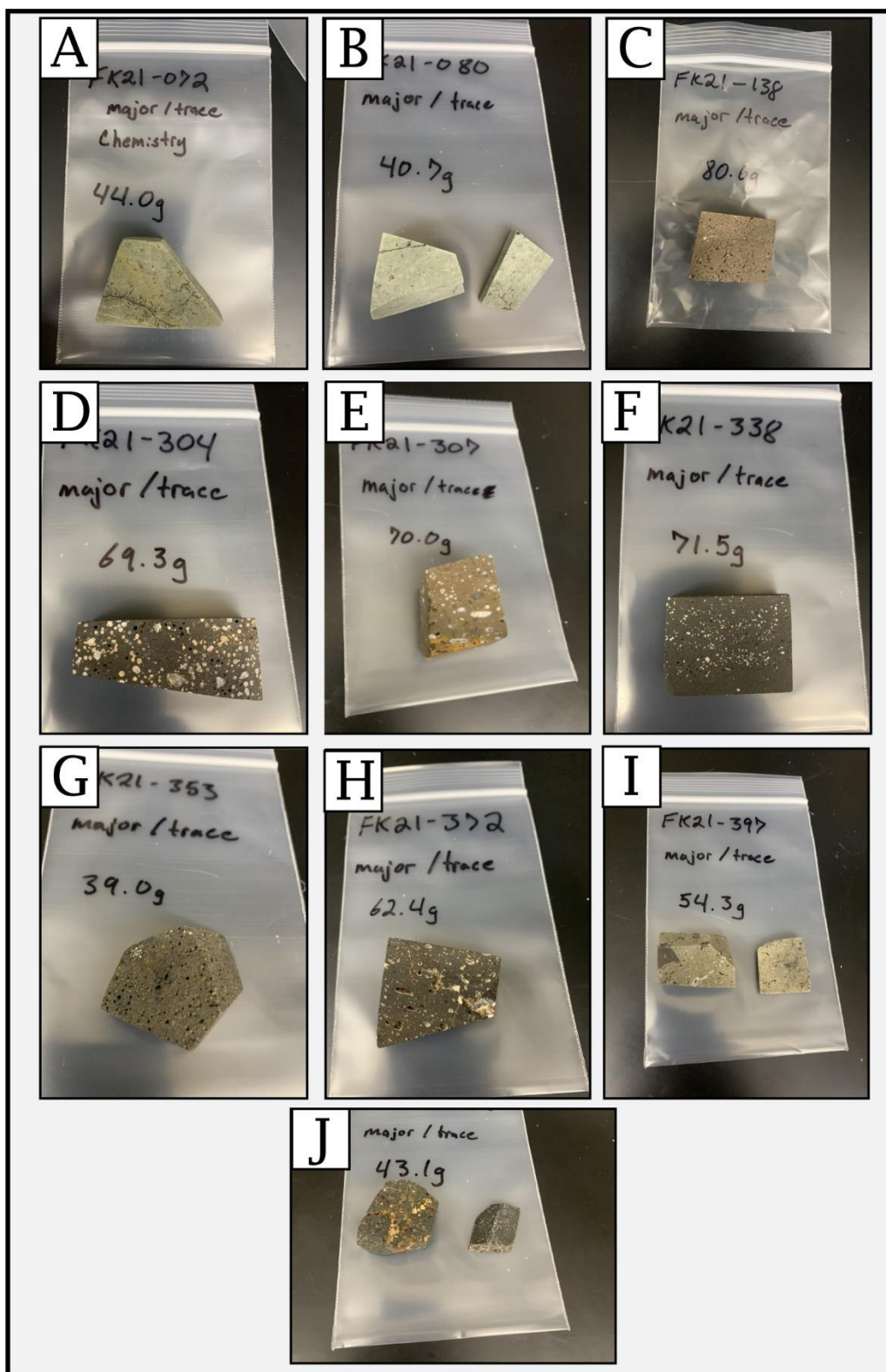


Figure 6: Hand samples images of representative core material gathered from seamounts during the FK210605 research cruise expedition. A = FK210605-072. B = FK210605-080. C = FK210605-138. D = FK210605-304. E = FK210605-307. F = FK210605-338. G = FK210605-353. H = FK210605-372. I = FK210605-397. J = FK210605-428.

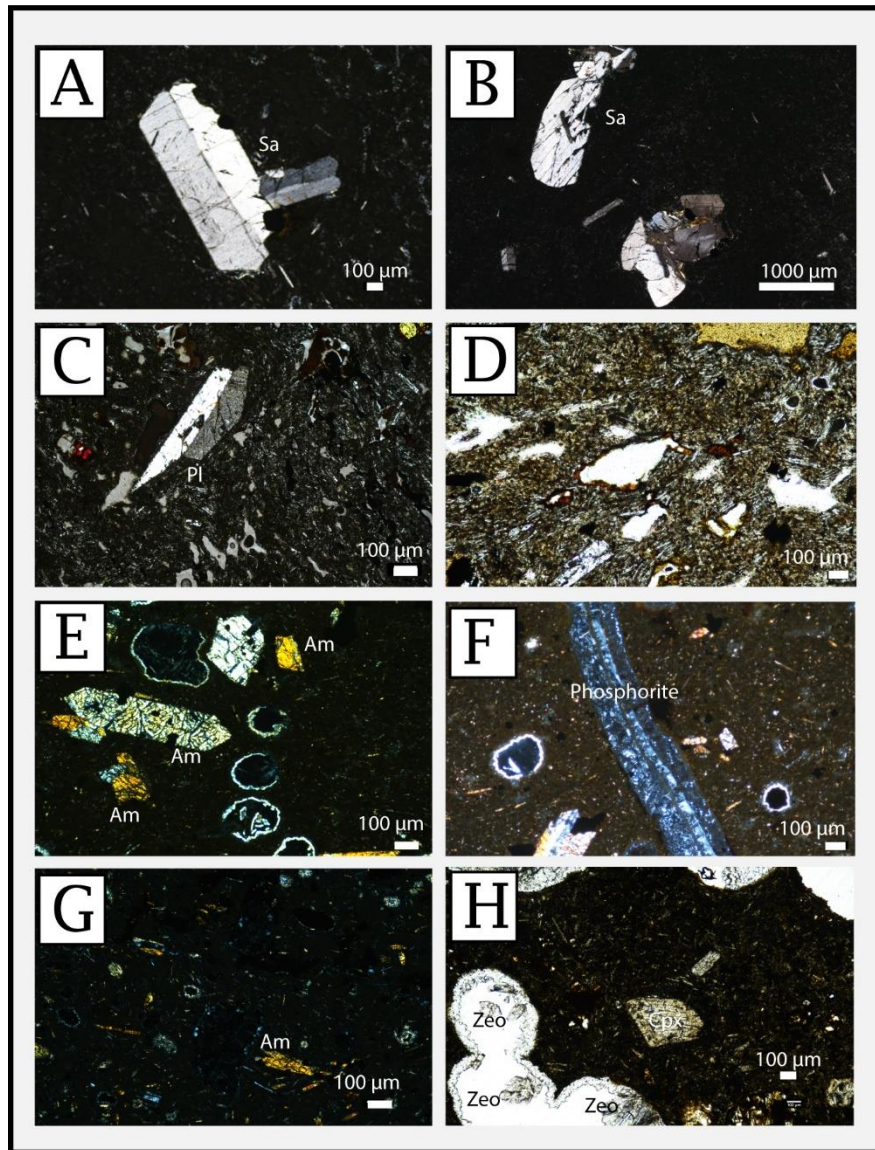


Figure 7: Representative XPL thin section images of sample phenocrysts and alteration effects from FK210605 and NA112. A = FK210605-072 Sanidine. B = FK210605-080 Sanidine. C = FK210605-138 Plagioclase. D = FK210605-138 Palagonite. E = FK210605-307 Hornblende. F = FK210605-373 Phosphorite vein. G = FK210605-397 Hornblende. H = NA112-001 Zeolite and Clinopyroxene.

Chapter 3: Results

3.1 Seamount descriptions

The following seamount morphology descriptions are accompanied by high resolution bathymetry maps of individual seamounts. Bathymetric rasters were generated using a variety of data compiled by the General Bathymetric Chart of the Oceans (GEBCO) database (GEBCO 2023 Grid, 2023). With the exception of Unnamed Seamount 1, contour lines are generated using available multibeam sonar data at 100 m intervals with 1000 m index contours. When shipboard data was not accessible, the 100 m contour lines were produced using GEBCO datasets.

Swains Island (11°07' S, 171°05' W) is a subaerially exposed seamount and atoll featuring a circular landmass surrounded by a coral lagoon and is located ~350 km north of America Samoa (Figure 8). Seven samples were picked from the seamount's southern flank during the NA112 expedition. The ROV began on the deep flank and moved up elevation northward and collected samples NA112-001, -002, -003, -004, -005, -006, and -008 in close (~1 km) proximity to each other. The explored southern flank ridge is bounded by a small slope failure terrace to the west, and a shallow saddle to the east.

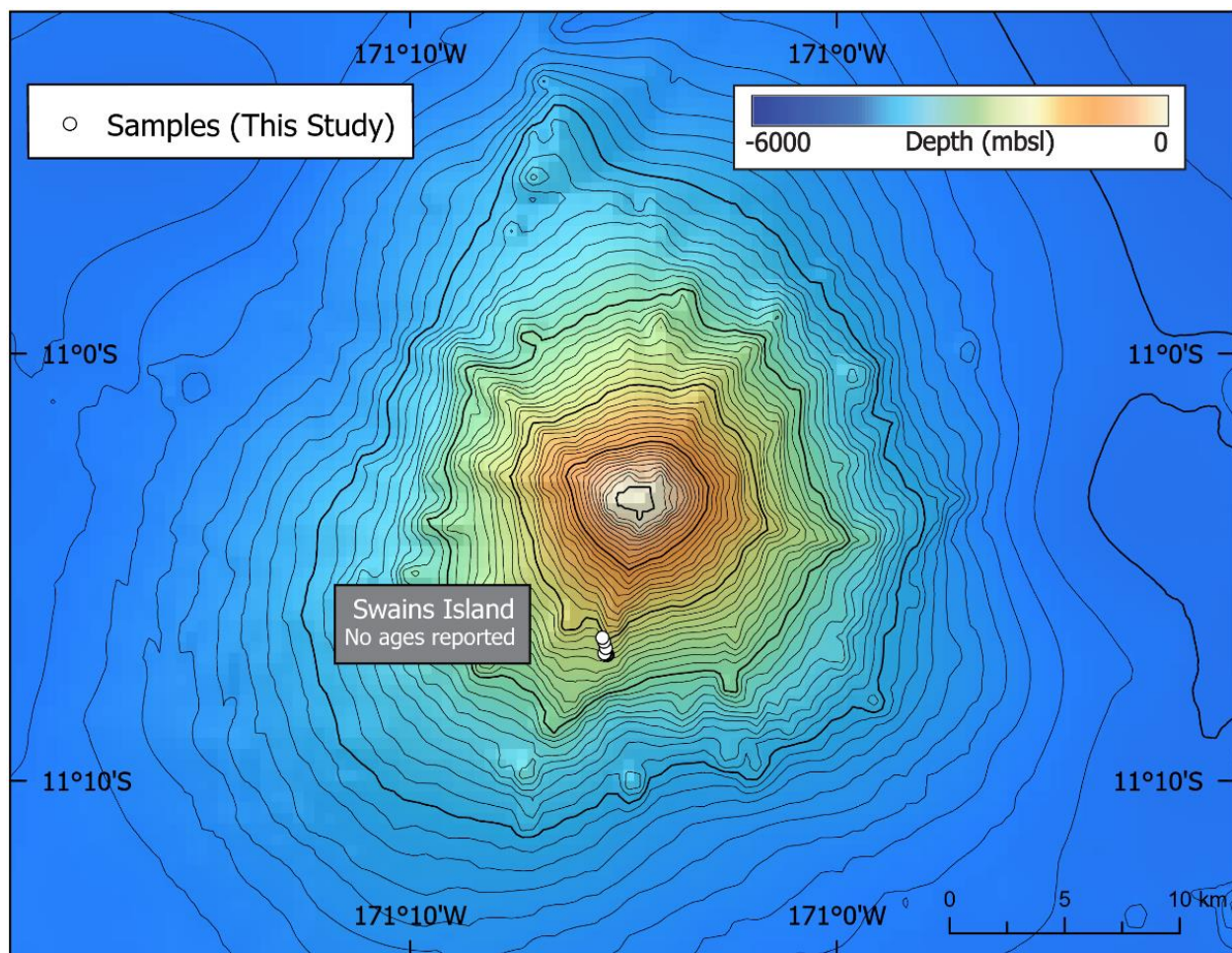


Figure 8: Colored bathymetry map lines of Swains Island and all sample locations collected from NA112 (NA112-001, -002, -003, -004, -005, -006, -008). Contour lines shown at 100 m intervals. Swains Island is a radially shaped seamount with a distinct eruptive center that is expected from intraplate submarine volcanism not affected by fracture zones or tectonics.

Howland Island (0°50' N, 176°35' W) is a subaerial seamount with an exposed coral atoll and is the maritime land boundary (along with Baker Island) defining the HBI EEZ (Maragos et al., 2008; Figure 9). The seamount is characterized by a central eruptive center, with three outward ridges. The single sample collected for this project from Howland Island, FK210605-138, was retrieved along the northern ridge. A recalculated age determination from Koppers et al. (2007) indicate the structure is 74.5 ± 0.7 Ma, an age which is within error of the new age reported in this study (73.57 ± 0.28 Ma; Figure 11C).

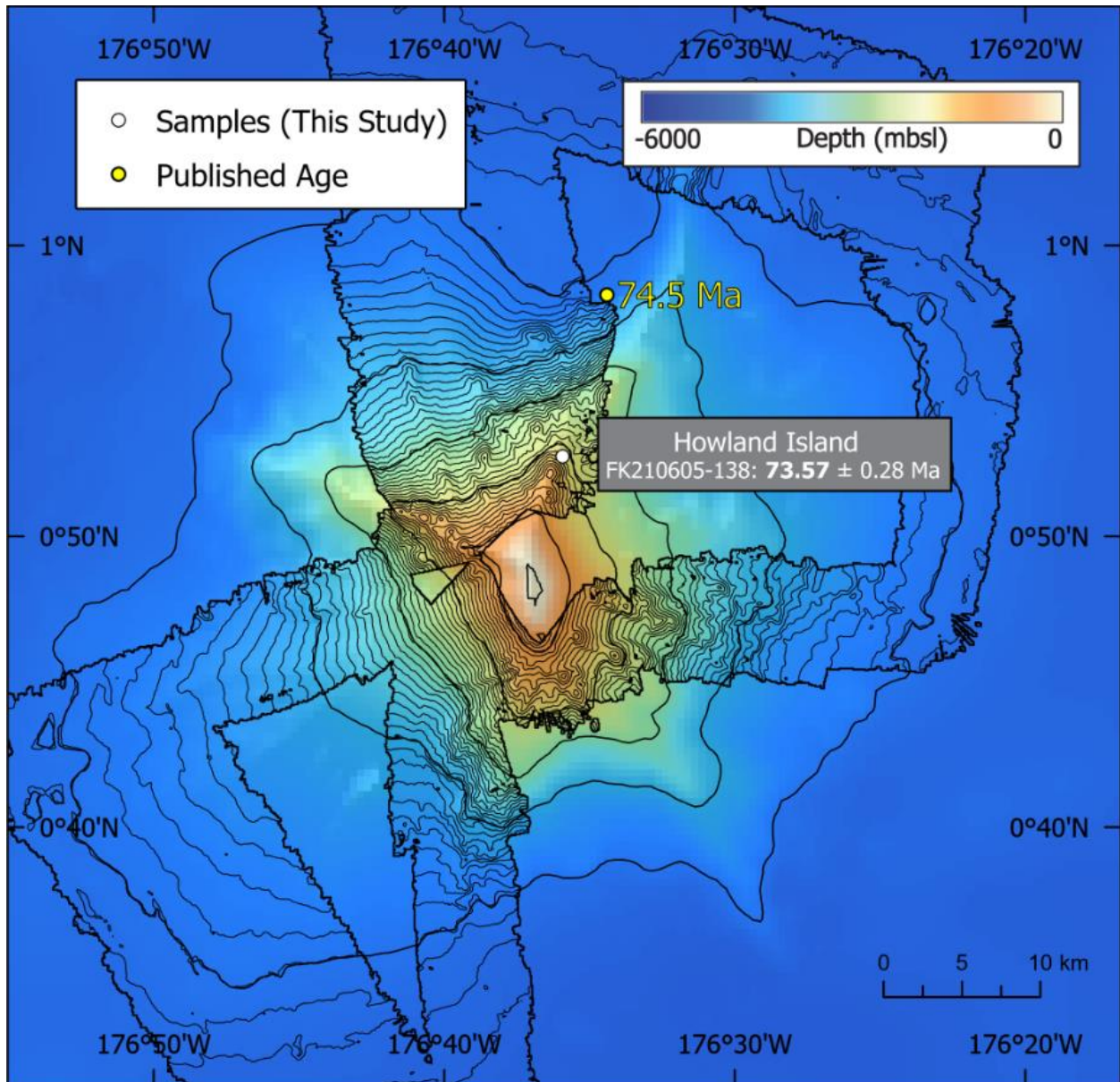


Figure 9: Colored bathymetry map of Howland Island. Contour lines shown as 100 m intervals. Howland Island's radial structure is highlighted by three prominently extending ridges. One sample was collected from the northern ridge (FK210605-138). Howland Island is one of two subaerial structures that defines the 200 nautical mile boundary of the HBI EEZ.

Unnamed Seamount 1 (3°52' N, 176°16' W) is a previously unsampled, submerged and relatively deep seamount (~2500 mbsl summit) that is located ~340 km north of Howland Island near the northern border of the HBI EEZ (Figure 10). The symmetrical and radial geometry of the seamount lacks distinguishable features due to the absence of high resolution multibeam data availability in the area. However, the surrounding bathymetry reveals a local and anomalous topographic swell of unknown origin (>5200 mbsl). The two samples collected from this location, FK210605-072 and FK210605-080 were both picked near the seamount's apex yet were unearthed significantly deeper than other samples used in this study (Table 1). The new age determinations from Unnamed Seamount 1 place the seamount in the Early Cretaceous (124.17 ± 0.12 Ma, 124.22 ± 0.13 Ma; Figure 11A and B), substantially older than other seamounts in this study.

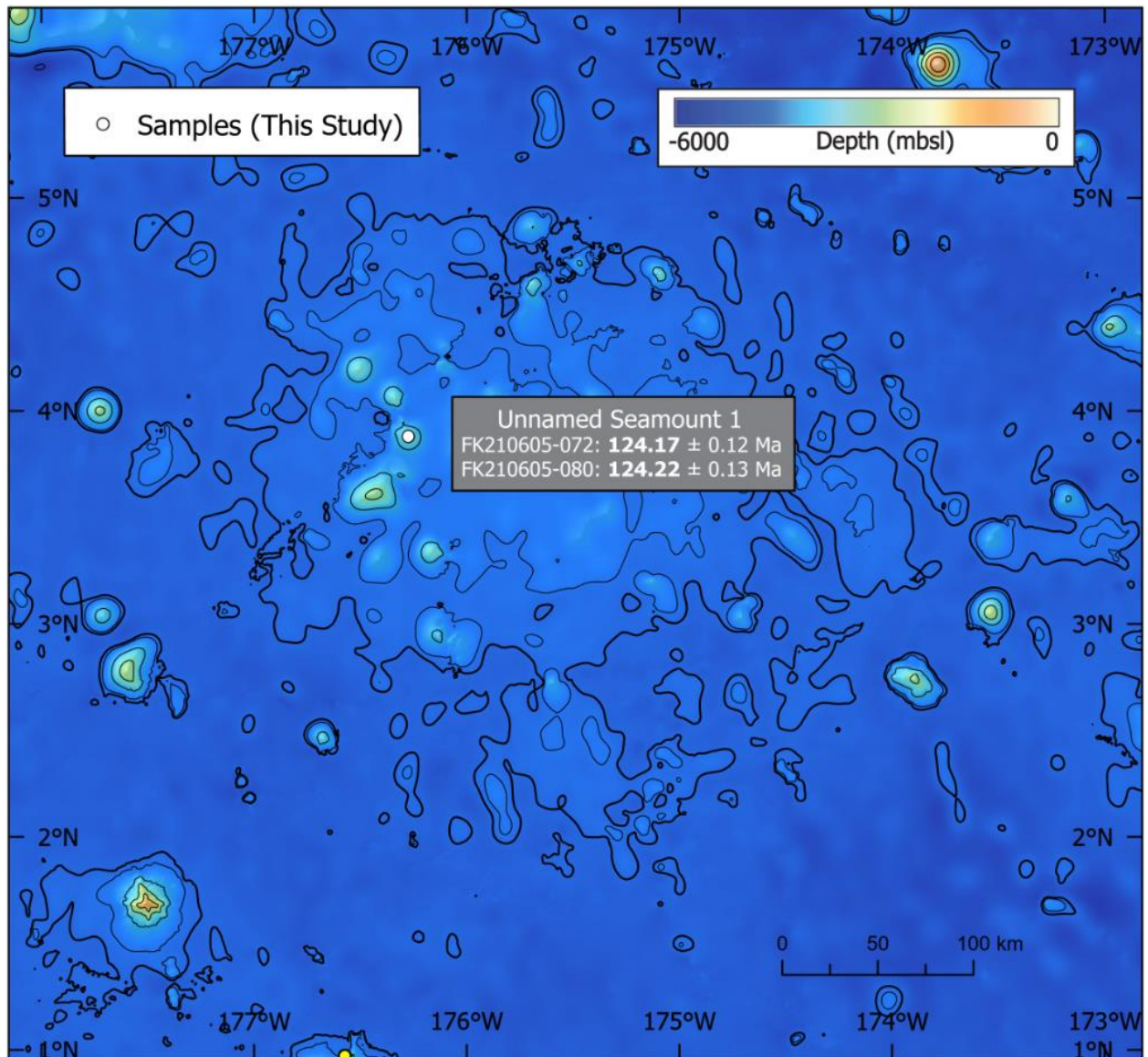


Figure 10: Colored bathymetry map of Unnamed Seamount 1. Contour lines shown as 1000 m intervals. Two samples were collected near seamount's apex (FK210605-072, -080). A local bathymetric swell of unknown origin is highlighted by a bold contour at 5200 mbsl.

Unnamed Seamount 2 (1°0' N, 179°18' W) and Unnamed Seamount 3 (0°51' N, 179°39' W) are previously unsampled seamounts located on the western edge of the HBI EEZ ~300 km west of Howland Island (Figure 11). The four samples collected from FK210605 at this site were originally assigned to a single seamount by exploration scientists (FK210605-304, -307, -338, -353). High resolution bathymetric data reveals two distinct peaks that are indicative of separate volcanic events and will be considered hereafter as individual seamounts. Unnamed seamount 2 is an elongated ridge oriented in a NE-SW direction with primary volcanic activity occurring towards the northwest. Unnamed Seamount 3 is a smaller, radially shaped structure and is separated from Seamount 3 by a ~5 km trough. Although two independent ages were obtained for the seamounts, the acceptable criteria required for age determinations was only achieved for Unnamed Seamount 2 (85.61 ± 0.14 Ma; Figure 11D).

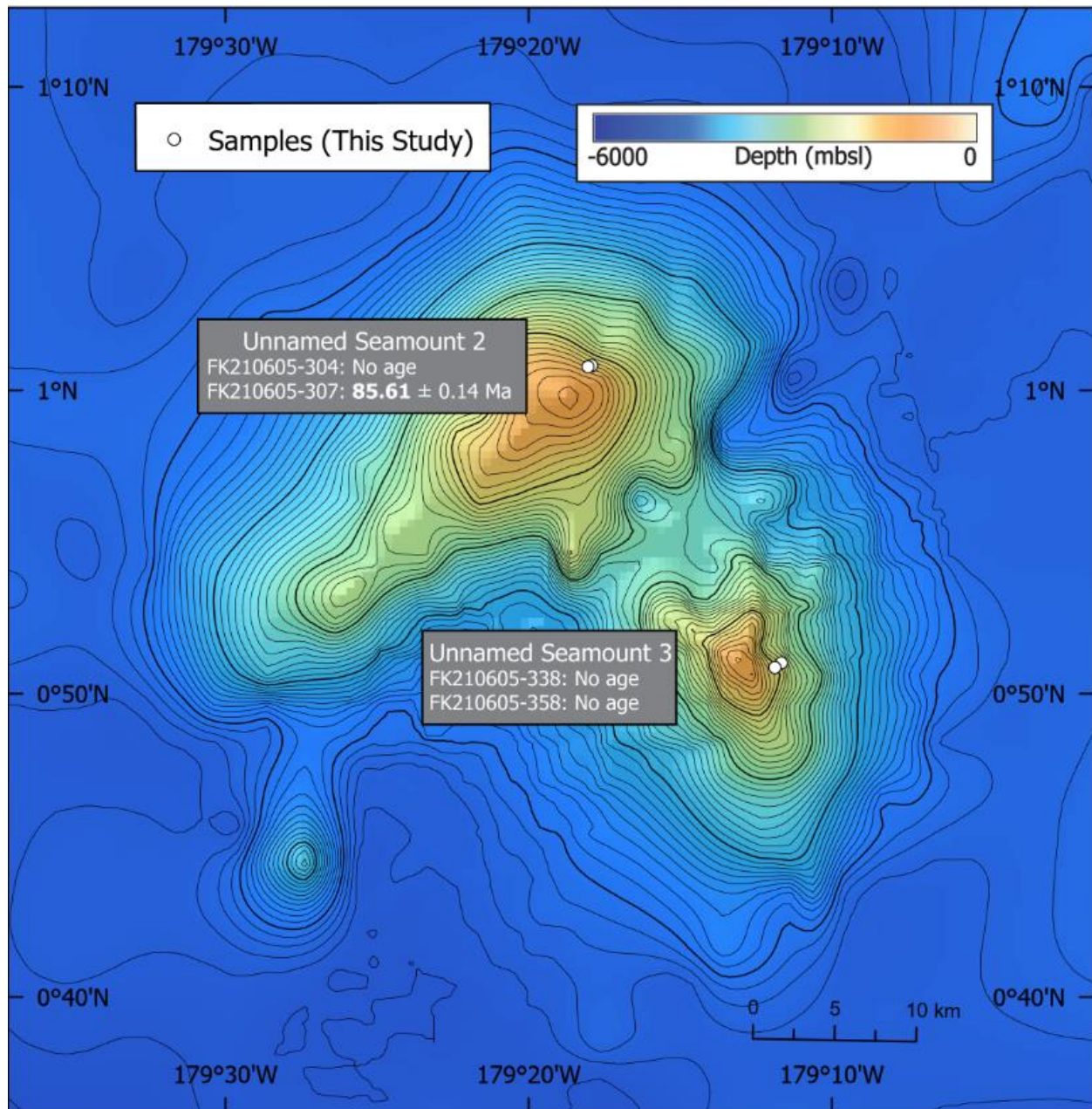


Figure 11: Colored bathymetry map of Unnamed Seamount 2 and Unnamed Seamount 3. Contour lines shown as 100 m intervals. Two samples were collected from Unnamed Seamount 2 (FK210605-304, -307) and another two from Unnamed Seamount 3 (FK210605-338, -353). A trough separates the two seamounts by ~5 km.

Titov Ridge (0°19' N, 176°03' W) is a previously unsampled seamount that is ~160 km south of Howland Island and exhibits an escarpment or slope failure morphology (Figure 12). The eastern flank is highlighted by a concave abscess separating the northern and southern flanks that is indicative of a large mass wasting or faulting event. There is a narrow, elongated ridge feature extending west and a nearby unsampled seamount further south. Of the two samples collected, only one contained the mineral separates required for analyses. The reported 71.46 ± 0.33 (Figure 12F) Ma age is an intermediary bound by previously published reported ages at Howland Island and Lelei.

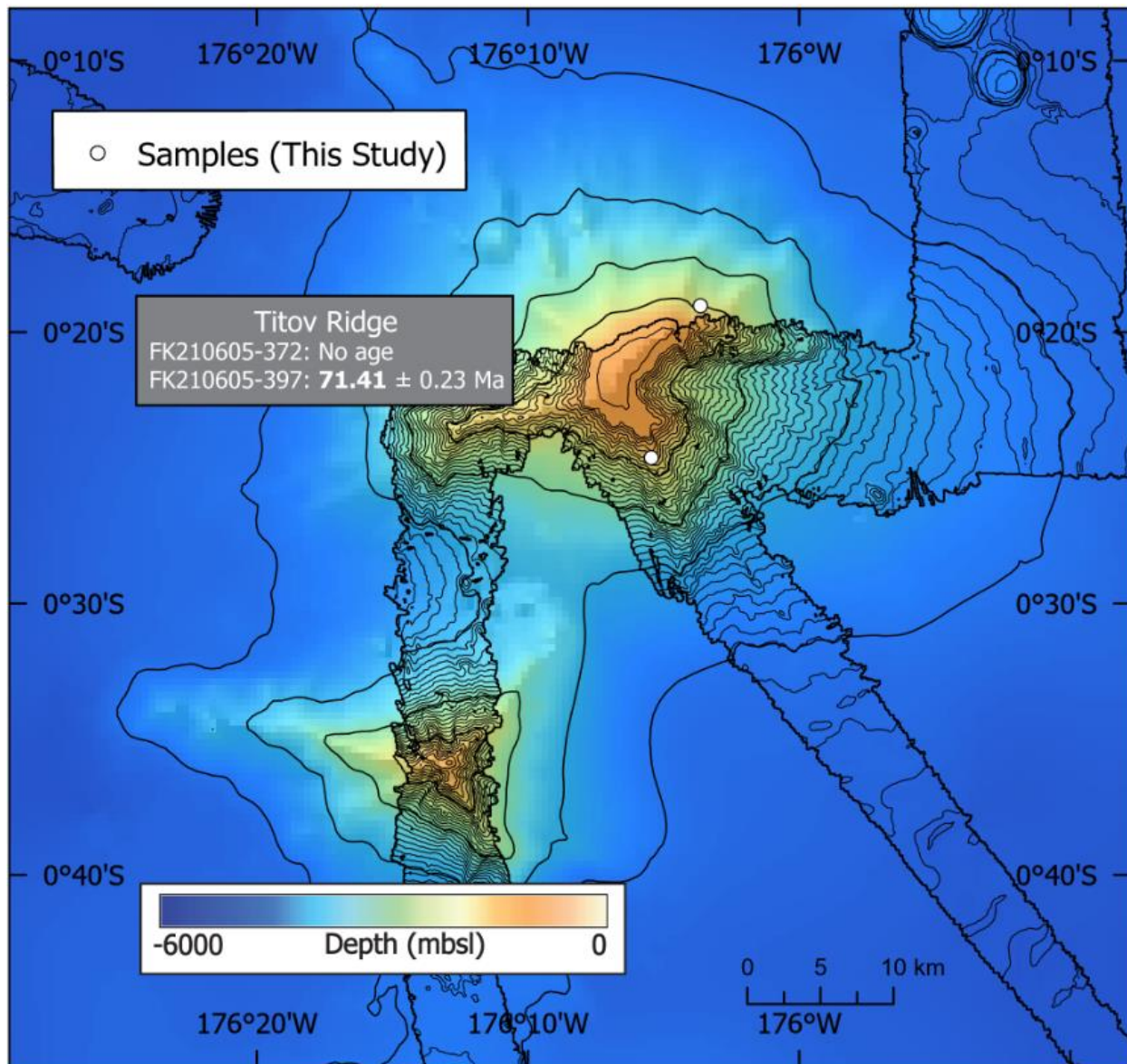


Figure 12: Colored bathymetry map of Titov Ridge. Contour lines shown as 100 m intervals. The ridge is characterized by a concave feature on the eastern flank and a narrow elongate ridge extending west. Two samples were recovered from the northern and southern flanks (FK21-397, -372).

Lelei (1°03' S, 176°10' W) is a star shaped submerged seamount with two volcanic peaks that is located ~220 km south of Howland Island (Figure 13). There is a small seamount structure to the northwest that may share a common source, though the seamount itself has yet to be sampled. An age determination of 70.2 ± 0.6 Ma was published by Koppers et al., (2007). The single sample recovered from Lelei for this project was collected along the southwest ridge. No new ages were obtained from Lelei, yet a recalculated age demonstrates the seamount is 70.4 ± 0.6 Ma.

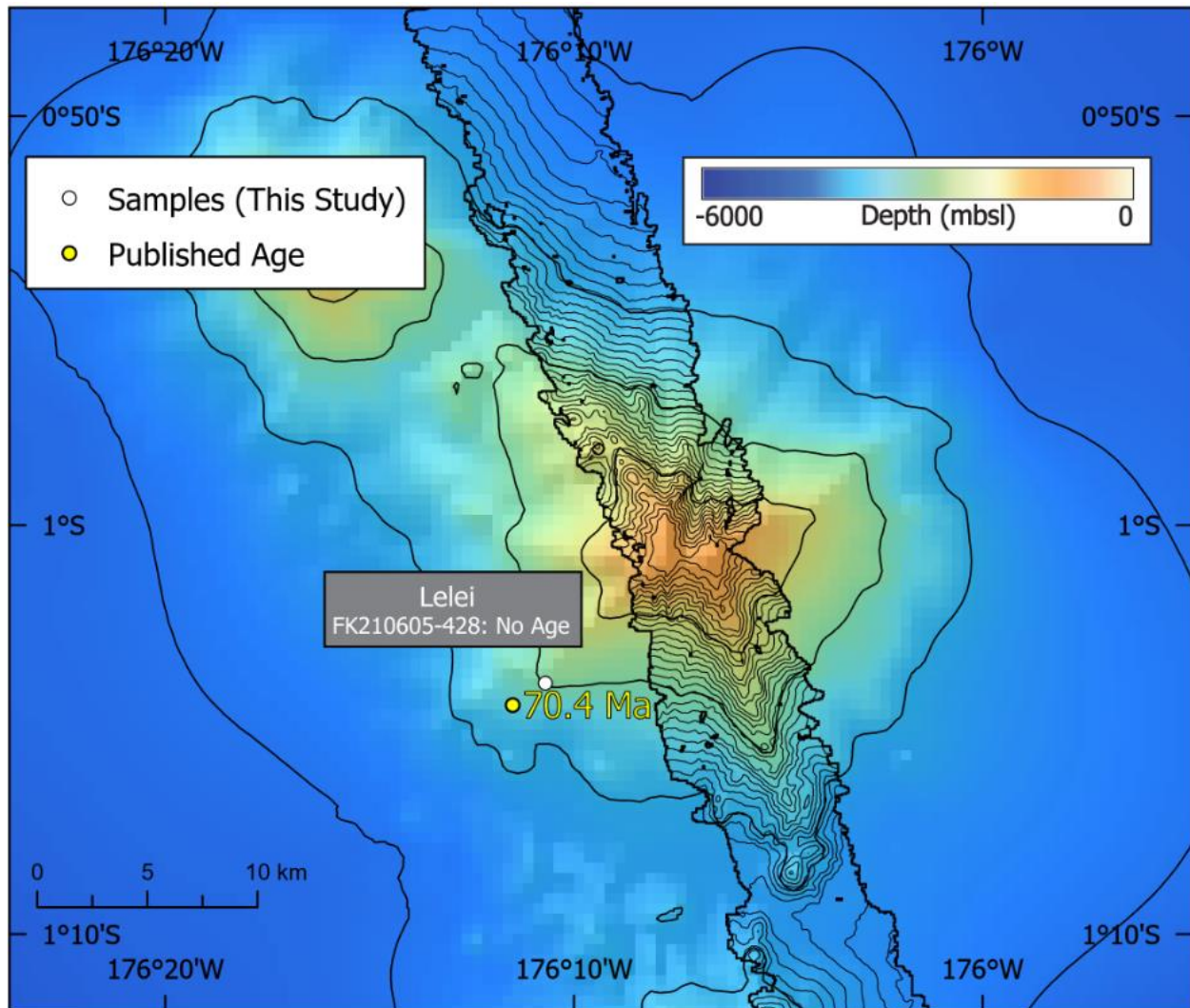


Figure 13: Colored bathymetry map of Lelei. Contour lines are shown at 100 m intervals. Lelei is characterized as a star shaped seamount with two volcanic peaks.

3.2 Major element geochemistry

Major element oxides of samples are presented in Table 2. Whole rock lithologies were classified according to the total alkali silica (TAS) scheme for classifying volcanic igneous rocks (Bas et al., 1986). The samples exhibit a range of compositions fluctuating from foidites to trachytes (Figure 14). Care should be taken when interpreting the accuracy of the TAS classification due to unrealistically low silica concentrations reported in a handful of samples due to visible alteration observed in the samples. All five samples that were analyzed from Swains Island (NA112-001, -002, -003, -005, -008), as well as samples from Titov Ridge (FK210605-372; Figure 6H) and Lelei (FK210605-428; Figure 6J) are reported as silica undersaturated foidites that hold <40 wt. % SiO₂. The second sample from Titov Ridge (FK210605-397; Figure 6I) exhibits a significantly higher SiO₂ content at 51.0 wt. % and is categorized as a trachy-andesite. A lone sample collected from Howland Island (FK210605-138; Figure 6C) shows an intermediate phonolite composition with 52.6 wt. % SiO₂ and elevated total alkali (Na₂O + K₂O) concentrations at 9.2 wt. %. Lava flows from Unnamed Seamount 1 reveal the most variable chemistries in the sample suite. Felsic volcanism is observed in both samples FK210605-072 (Figure 6A) and FK210605-080 (Figure 6B) with 64.2 and 64.7 wt. % silica proportions, respectively, and total alkali values reported at 11.9 and 11.8 wt. %. The two samples gathered from Unnamed Seamount 2 (FK210605-304; Figure 6D, FK210605-307; Figure 6E) both are slightly silica undersaturated. Additionally, these samples reveal slight silica undersaturation (43.4 - 46.0 wt. %) and alkali compositions (3.4 - 4.7 wt. %). Similarly, samples from Unnamed Seamount 3 (FK210605-338; Figure 6F, FK210605-353; Figure 6G) have slightly lower silica concentrations ranging from (41.94 - 44.8 wt. %) and lower alkali concentrations (4.3 - 4.7 wt. %).

Table 2: Major element oxides of selected samples reported as weight percent (wt. %) normalized to 100% totals. NA112 samples are from Swains Island.

Sample ID	Location	SiO ₂	TiO ₂	Al ₂ O ₃	Fe ₂ O ₃	MnO
NA112-001	Swains Island	40.1	5.0	10.5	16.3	0.2
NA112-002	Swains Island	39.9	4.8	10.4	15.7	0.2
NA112-003	Swains Island	38.5	5.2	10.2	16.9	0.3
NA112-005	Swains Island	38.7	4.7	10.4	15.5	0.2
NA112-008	Swains Island	38.9	4.3	9.8	16.8	0.3
FK21-072	Unnamed Smt 1	64.2	0.4	15.2	6.5	0.4
FK21-080	Unnamed Smt 1	64.7	0.4	15.5	6.1	0.1
FK21-138	Howland Island	52.6	0.6	16.5	7.6	0.4
FK21-304	Unnamed Smt 2	43.4	2.6	13.7	10.2	0.2
FK21-307	Unnamed Smt 2	46.0	2.8	19.9	11.8	0.3
FK21-338	Unnamed Smt 3	44.8	3.8	14.5	12.2	0.1
FK21-353	Unnamed Smt 3	41.9	3.3	14.4	8.9	0.5
FK21-372	Titov Ridge	37.7	4.3	16.2	13.0	0.2
FK21-397	Titov Ridge	51.0	2.3	18.3	9.5	0.5
FK21-428	Lelei	37.4	4.4	11.5	15.5	0.3

Sample ID	Location	MgO	CaO	Na ₂ O	K ₂ O	P ₂ O ₅
NA112-001	Swains Island	7.6	16.0	1.6	1.5	1.4
NA112-002	Swains Island	7.2	16.1	1.8	1.7	2.1
NA112-003	Swains Island	7.2	16.6	1.4	1.6	2.2
NA112-005	Swains Island	6.6	17.0	1.6	1.9	3.5
NA112-008	Swains Island	6.7	16.3	1.6	2.1	3.4
FK21-072	Unnamed Smt 1	0.7	0.7	7.0	4.9	0.1
FK21-080	Unnamed Smt 1	0.7	0.7	6.9	4.9	0.1
FK21-138	Howland Island	0.7	8.7	5.7	3.5	3.9
FK21-304	Unnamed Smt 2	2.3	19.5	3.3	2.7	2.0
FK21-307	Unnamed Smt 2	2.9	10.1	3.0	2.1	1.3
FK21-338	Unnamed Smt 3	3.2	14.2	2.8	1.9	2.5
FK21-353	Unnamed Smt 3	2.4	16.3	2.8	1.5	8.0
FK21-372	Titov Ridge	5.4	15.3	1.4	1.4	5.2
FK21-397	Titov Ridge	3.9	7.3	2.9	3.3	1.1
FK21-428	Lelei	3.7	15.0	1.9	2.6	7.8

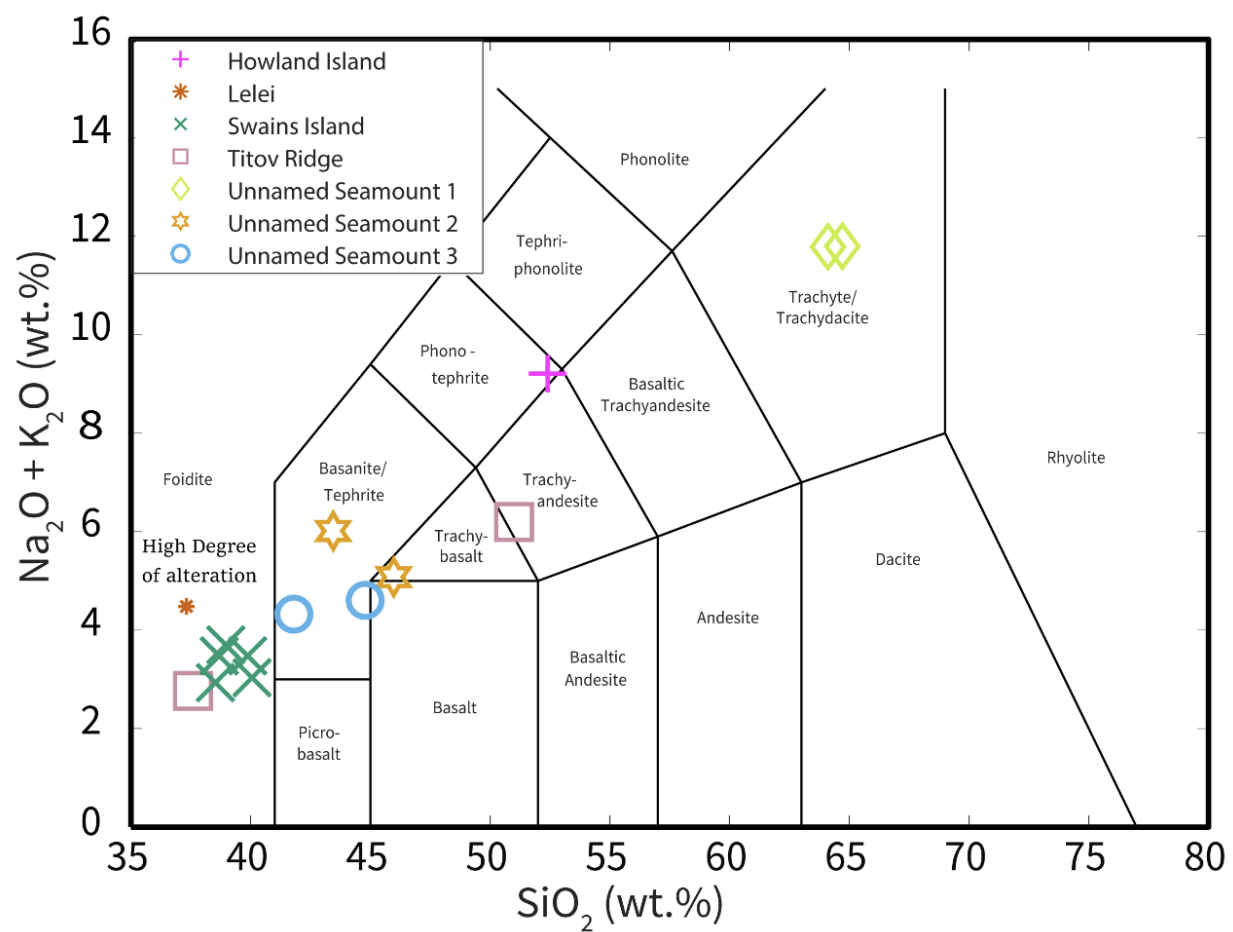


Figure 14: Total alkali silica chemical classification diagram for volcanic rocks (Bas et. al, 1987). Study samples are symbolized by individual seamounts.

3.3 Trace element geochemistry

Bulk rock geochemistry is presented in Table 3 and Table 4 that reveals three distinct trends of elemental concentrations. The trends are presented in the form of trace element diagrams normalized to established primitive upper mantle values (Figure 15; Sun and McDonough, 1989) and are categorized with respect to the proximity of the projected Macdonald Hotspot track. Figure 15A exhibits distinct U, Sr, and Ti depletion patterns from trachyte samples recovered from Unnamed Seamount 1 (FK210605-072, -080). However, there is a stark contrast in Ba enrichment observed in these two samples (2129 ppm and 21 ppm, respectively). The second set of samples in Figure 15B consist of samples retrieved from Unnamed Seamount 2 (FK210605-304, -307) and Unnamed Seamount 3 (FK210605-338, -353) shows a progressively shallowing and almost uniform decreasing slope. An enrichment in Y is observed in at Lelei (FK210605-428; Figure 15C), similar to two samples from Swains Island (NA112-005, -008) and both samples from Unnamed Seamount 1 (FK210605-072, -080).

Table 3: Whole rock trace element concentrations of selected samples reported in ppm. BDL signifies sample concentration is below instrumental detection limits.

Sample ID	Cs	Rb	Ba	Th	U	Nb	Ta	K	La
NA112-001	BDL	23	378	12	1.3	111	12	12037	129
NA112-002	BDL	26	434	11	1.7	107	11	13946	102
NA112-003	BDL	30	488	10	2.1	102	10	12535	109
NA112-005	BDL	31	603	10	2.0	97	11	15109	138
NA112-008	BDL	35	514	10	2.6	99	11	16603	113
FK21-072	0.18	45	2129	38	0.5	283	90	39183	312
FK21-080	0.13	45	21	40	0.4	321	86	39515	428
FK21-138	0.34	40	1177	16	1.4	139	21	27810	113
FK21-304	0.67	45	496	6	1.1	68	8	21169	56
FK21-307	0.97	34	729	11	1.5	121	12	16271	94
FK21-338	0.79	26	300	5	0.9	51	9	15026	41
FK21-353	0.86	29	650	3	2.9	38	8	12286	46
FK21-372	0.22	16	407	9	1.7	78	11	11041	80
FK21-397	0.21	35	1308	19	0.9	165	21	26482	97
FK21-428	1.24	47	476	5	2.0	50	9	20754	149

Sample ID	Ce	Pr	Pb	Nd	Sr	Zr	Hf	Sm	Eu
NA112-001	199	7.59	4	105	691	523	12	19	6
NA112-002	189	7.21	4	88	727	457	11	16	5
NA112-003	204	7.24	4	89	698	402	10	16	5
NA112-005	184	6.64	4	102	686	470	11	19	5
NA112-008	178	6.66	3	87	746	462	11	16	5
FK21-072	367	0.72	4	245	157	3979	90	46	5
FK21-080	347	0.67	4	316	27	3544	86	56	6
FK21-138	206	0.66	8	92	576	655	21	16	6
FK21-304	106	2.33	2	57	783	351	8	11	4
FK21-307	174	2.89	4	81	1182	582	12	14	5
FK21-338	82	3.15	2	51	815	370	9	11	4
FK21-353	71	2.42	3	49	1015	350	8	11	4
FK21-372	153	5.39	4	86	2257	478	11	17	5
FK21-397	242	3.85	8	87	2089	1054	21	15	5
FK21-428	91	3.67	5	93	415	411	9	18	6

Table 4: Whole rock trace element concentrations of selected samples reported in ppm.

Sample ID	Ti	Gd	Tb	Dy	Ho	Y	Er	Yb	Lu
NA112-001	28896	17	3	14	3	92	7	5	0.7
NA112-002	27697	13	2	10	2	52	4	3	0.5
NA112-003	30095	13	2	11	2	71	5	4	0.6
NA112-005	27098	17	3	16	3	157	9	8	1.3
NA112-008	24760	14	2	12	3	120	7	6	1.0
FK21-072	2038	41	7	39	8	214	21	22	3.2
FK21-080	2158	49	8	42	9	227	23	24	3.6
FK21-138	3417	14	2	11	2	66	5	4	0.6
FK21-304	14508	9	1	7	1	36	3	3	0.3
FK21-307	15647	10	2	7	1	37	3	2	0.3
FK21-338	22122	9	1	6	1	33	3	2	0.3
FK21-353	19544	9	1	7	1	62	4	3	0.5
FK21-372	24820	12	2	8	1	42	3	2	0.3
FK21-397	13369	10	1	7	1	37	3	2	0.3
FK21-428	25539	19	3	18	5	257	13	15	2.4

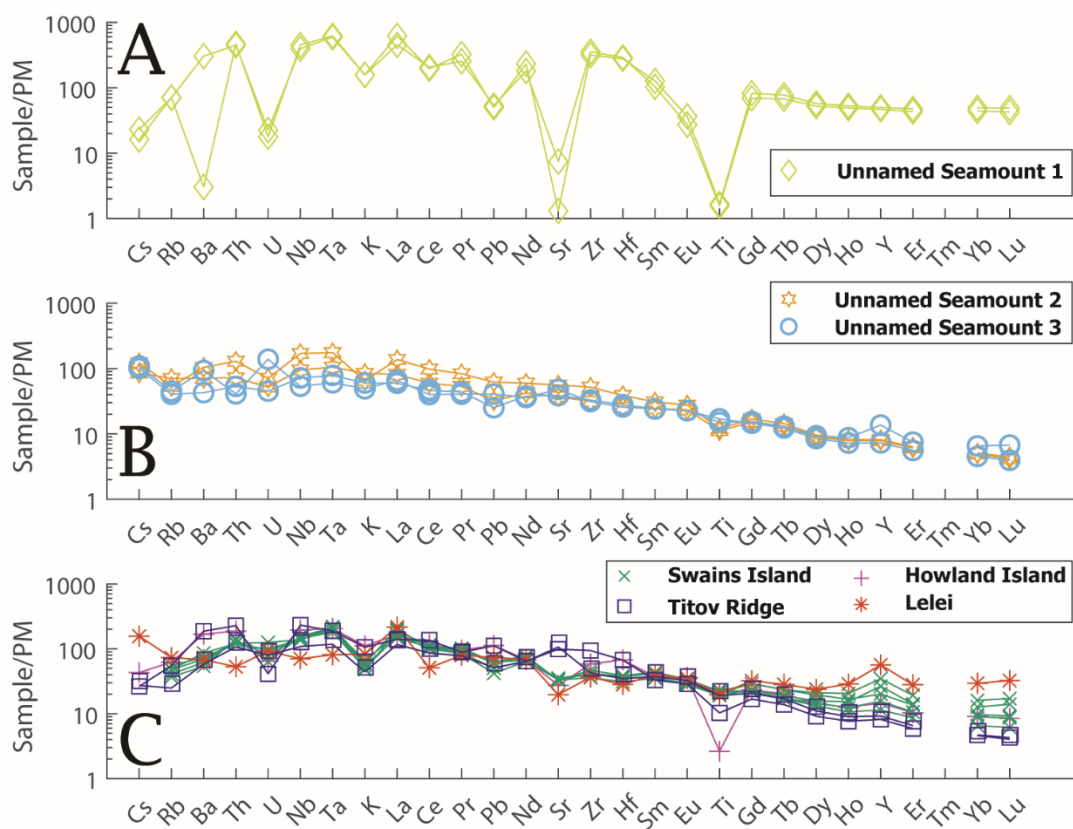


Figure 15: Trace element diagram normalized to primitive upper mantle values (Sun and McDonough, 1989) displaying three geochemical trends. Seamounts plots are arranged with respect to proximity of the projected Macdonald Hotspot track for clarity.

A rare earth element (REE) diagram highlights the decreasing slopes among the samples that represents enrichments in slightly more incompatible light rare earth element (LREE) than in heavy rare earth elements (HREE) (Figure 16). Europium negative anomalies (deviations of Eu concentrations relative to Sm and Gd) are present at Unnamed Seamount 1 (FK210605-072 $\text{Eu}/\text{Eu}^* = 0.1$, FK210605-080 $\text{Eu}/\text{Eu}^* = 0.1$) illustrating Eu incorporation during plagioclase crystallization. Slight HREE increases are observed at Lelei (FK210605-428), Unnamed Seamount 3 (FK210605-353) and Swains Island (NA112-005, -008). A range of La/Lu ratios are observed from 91-308 among all analyzed samples.

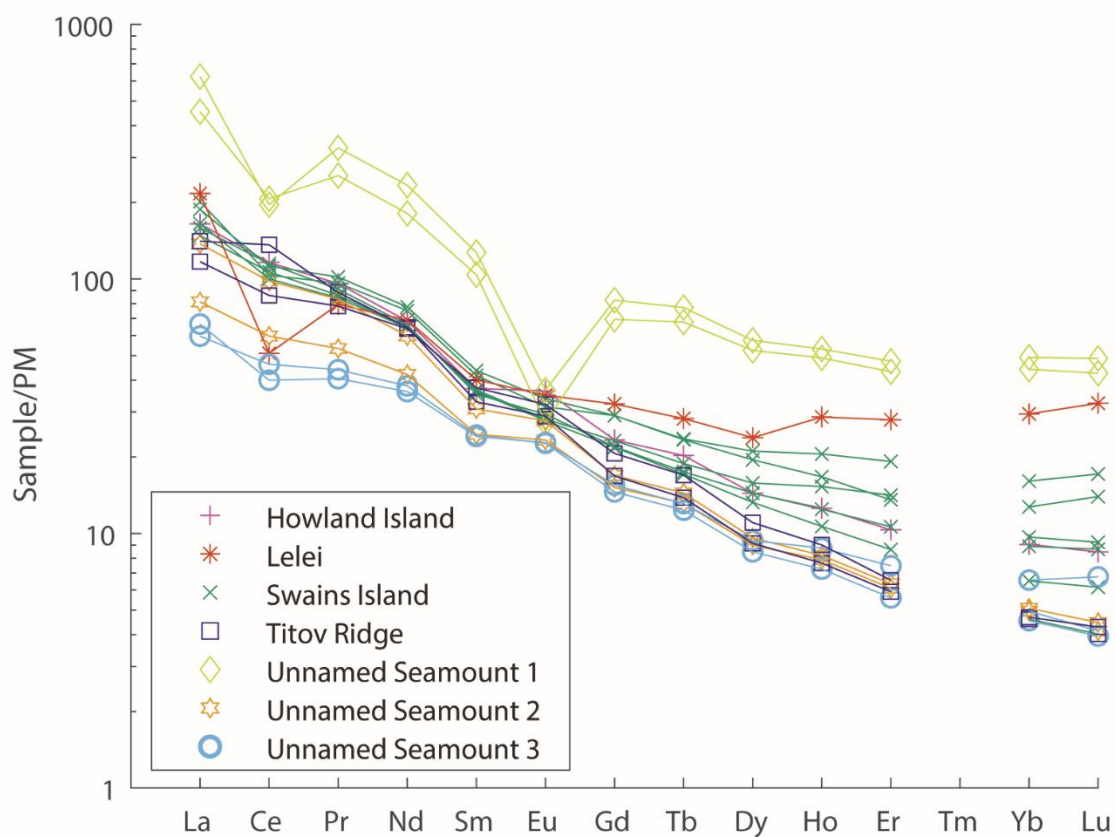


Figure 16: REE diagram illustrating enrichment patterns of lava flow samples. Eu anomalies are present in samples FK210605-072, -080 (Unnamed Seamount 1). An increase in HREE is observed in some samples between Yb and Lu.

3.4 $^{40}\text{Ar}/^{39}\text{Ar}$ geochronology

Incremental heating experiments were conducted on lava samples from NA112 and FK210605. Though experiments were attempted on five samples from Swains Island, the clinopyroxene phenocrysts (Figure 7H) did not contain adequate potassium concentrations required for reliable age plateaus. Therefore, the age determination experiments from Swains Island were unsuccessful and will not be discussed further here. Five new ages were resolved from four distinct seamounts in the HBI EEZ. The experimental results are summarized in Table 3. Samples that were selected for age determination experiments were chosen by the availability of targeted mineral phases after mineral separation and leaching. Following the protocol outlined in Schaen et al., (2021), concordant age plateaus are defined as containing $>50\%$ of the $^{39}\text{Ar}_{(\text{K})}$ released over five or more contiguous heating steps. Additionally, we include a requirement that the plateaus probability of fit must be $>5\%$ (Jiang and Jourdan, 2024).

The results of age determination experiments vary with respect to their locations within the Howland and Baker EEZ (Figure 17). Incremental heating experiments on sanidine phenocrysts (Figure 18A, 18B) from Unnamed Seamount 1 produced two concordant ages, both of which are within uncertainty. FK210605-072 produced a concordant plateau of 124.17 ± 0.12 Ma ($P = 5\%$, $\text{MSWD} = 1.70$, $^{39}\text{Ar}_{(\text{K})} = 56\%$, $^{40}\text{Ar}/^{36}\text{Ar}_0 = 235 \pm 102$) whereas FK210605-080 yielded an age of 124.22 ± 0.13 Ma ($P = 9\%$, $\text{MSWD} = 1.63$, $^{39}\text{Ar}_{(\text{K})} = 64\%$, $^{40}\text{Ar}/^{36}\text{Ar}_0 = 277 \pm 43$; Figure 18B). The K/Ca for FK210605-072 and -080 (54 ± 5 , 59 ± 6) are consistent with sanidine crystals. Howland Island plagioclase (Figure 7C) separates ($\text{K}/\text{Ca} = 1 \pm 0.001$) produced an age of 73.57 ± 0.28 Ma ($P = 7\%$, $\text{MSWD} = 2.15$, $^{39}\text{Ar}_{(\text{K})} = 64\%$, $^{40}\text{Ar}/^{36}\text{Ar}_0 = 350 \pm 150$; Figure 18C). Amphibole separates from sample FK210605-307 (Figure 7E) retrieved from Unnamed Seamount 2 revealed an intermediate age of 85.61 ± 0.14 Ma ($P = 73\%$, $\text{MSWD} = 0.75$, $^{39}\text{Ar}_{(\text{K})} = 99\%$, $^{40}\text{Ar}/^{36}\text{Ar}_0 = 279 \pm$

38; Figure 18D). The amphibole sample FK210605-397 (Figure 7G) at Titov Ridge is the youngest age of all samples at 71.41 ± 0.23 Ma ($P = 39\%$, $MSWD = 1.06$, $^{39}\text{Ar}_{(K)} = 89\%$, $^{40}\text{Ar}/^{36}\text{Ar}_0 = 356 \pm 45$; Figure 19F). While all previous samples produced concordant age plateaus, FK210605-397 age was recalculated using a non-atmospheric $^{40}\text{Ar}/^{39}\text{Ar}$ value of 356. A final experiment was attempted on plagioclase separates from sample FK210605-338 (115.44 ± 1.38 Ma, $P = 41\%$, $MSWD = 0.88$, $^{39}\text{Ar}_{(K)} = 55\%$, $^{40}\text{Ar}/^{36}\text{Ar}_0 = 267 \pm 236$; Figure 19E). The results from this experiment did not produce a concordant plateau consisting of five continuous steps and is not reported as a final result.

Table 5: $^{40}\text{Ar}/^{39}\text{Ar}$ age determination incremental heating experiments summary from samples recovered from FK210605. Plateau ages are reported as having >50% cumulative ^{39}Ar released over at least five successive heating steps with a probability of fit >5%. Uncertainties are reported at 95% confidence levels. Plateau ages with asterisks indicate recalculated ages using non-atmospheric $^{40}\text{Ar}/^{36}\text{Ar}$ (295.98). SAN = Sanidine, PLG = Plagioclase, HBL = Hornblende. ^{39}Ar is the cumulative $^{39}\text{Ar}_{(\text{K})}$ gas released included in plateau calculations. MSWD = Mean square of weighted deviates. P = Probability of fit. n = Number of cumulative heating steps used in plateau calculation. N = Total number of heating steps.

Sample ID	Seamount	Phas	Plateau Age (Ma)	$^{39}\text{Ar}_{(\text{K})}$	MSWD
FK210605-072	Unnamed Smt 1	SAN	124.17 ± 0.12	56	1.7
FK210605-080	Unnamed Smt 1	SAN	124.22 ± 0.13	64	1.6
FK210605-138	Howland Island	PLG	73.57 ± 0.28	64	2.2
FK210605-307	Unnamed Smt 2	HBL	85.61 ± 0.14	99	0.8
FK210605-397	Titov Ridge	HBL	$71.41 \pm 0.23^*$	89	1.1

Sample ID	K/Ca	P	n	N	$^{40}\text{Ar}/^{36}\text{Ar}$
FK210605-072	53.9 ± 5.0	5	14	36	235.22 ± 102.12
FK210605-080	58.7 ± 5.8	9	11	18	276.59 ± 42.78
FK210605-138	0.095 ± 0.001	7	5	15	350.18 ± 150.39
FK210605-307	0.064 ± 0.009	73	15	21	279.15 ± 38.13
FK210605-397	0.135 ± 0.024	39	11	19	356.01 ± 45.48

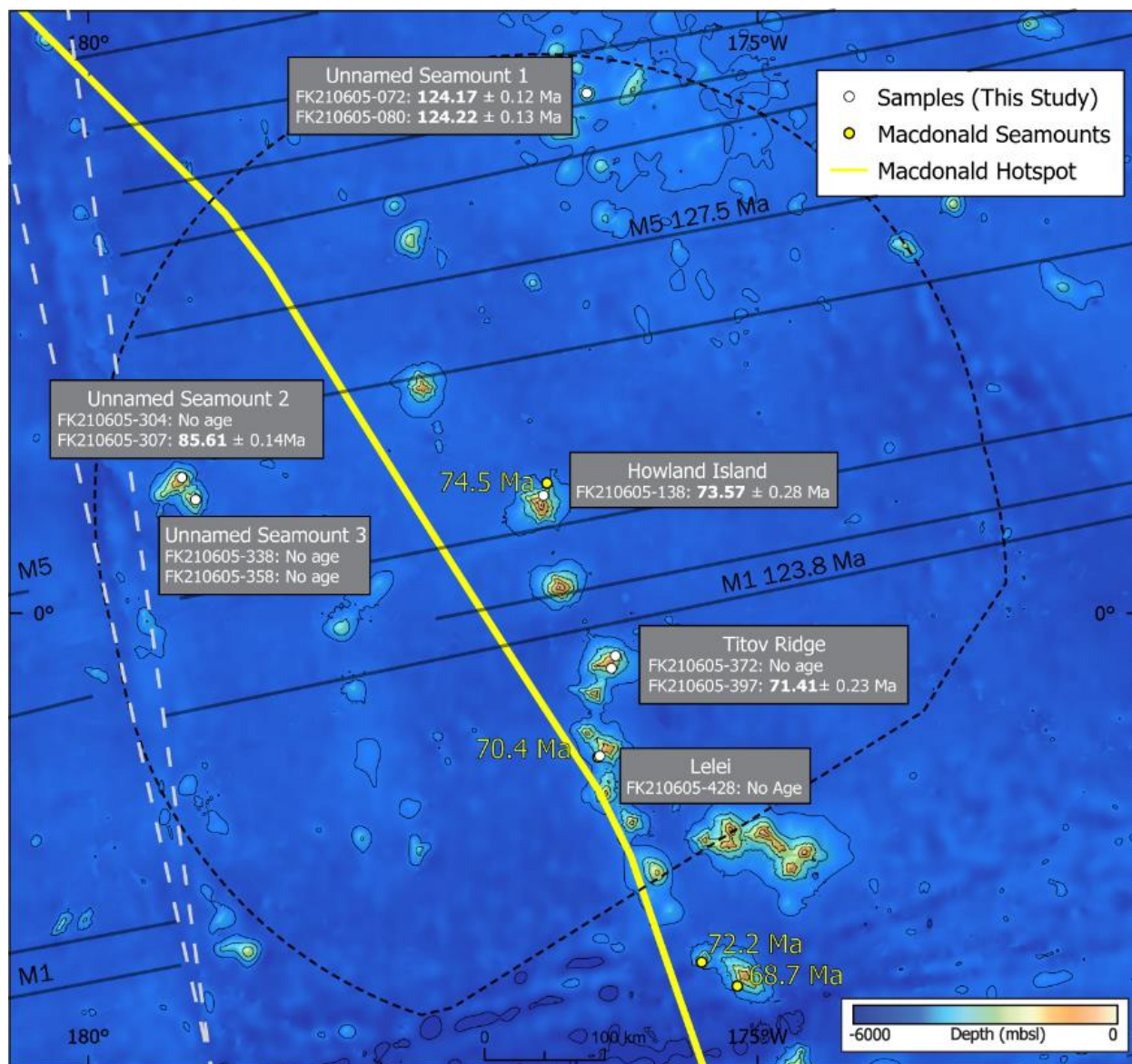


Figure 17: Map of the Howland and Baker Island EEZ with new $^{40}\text{Ar}/^{39}\text{Ar}$ age determinations outlined in grey boxes.

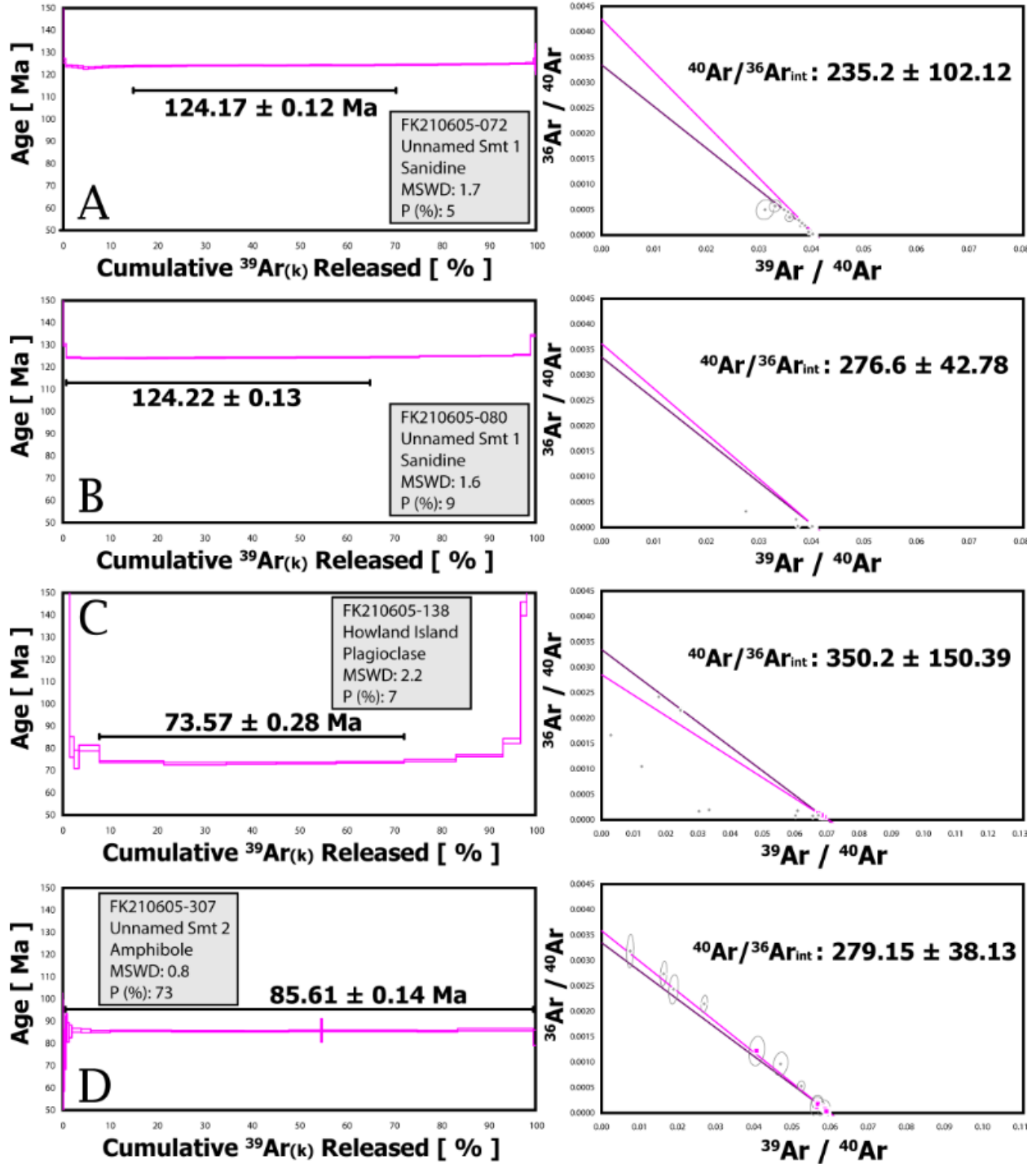


Figure 18: Age determinations and inverse isochron results from incremental $^{40}\text{Ar}/^{39}\text{Ar}$ heating experiments. Uncertainties are reported at the 95% confidence level. Purple rectangular segments in the left column represent individual heating steps and the corresponding dark line segments represent concordant age plateaus. Purple lines on the right column are inverse isochrons that represent sample $^{40}\text{Ar}/^{36}\text{Ar}$ values. The black lines reference $^{40}\text{Ar}/^{36}\text{Ar}$ atmospheric value isochrons. The pink squares are individual sample values shown with error ellipses. Grey circles are heating steps outside of 2σ and thus excluded from isochron interpretations. (A) FK210605-072, (B) FK210605-080, (C) FK210605-138, (D) FK210605-307.

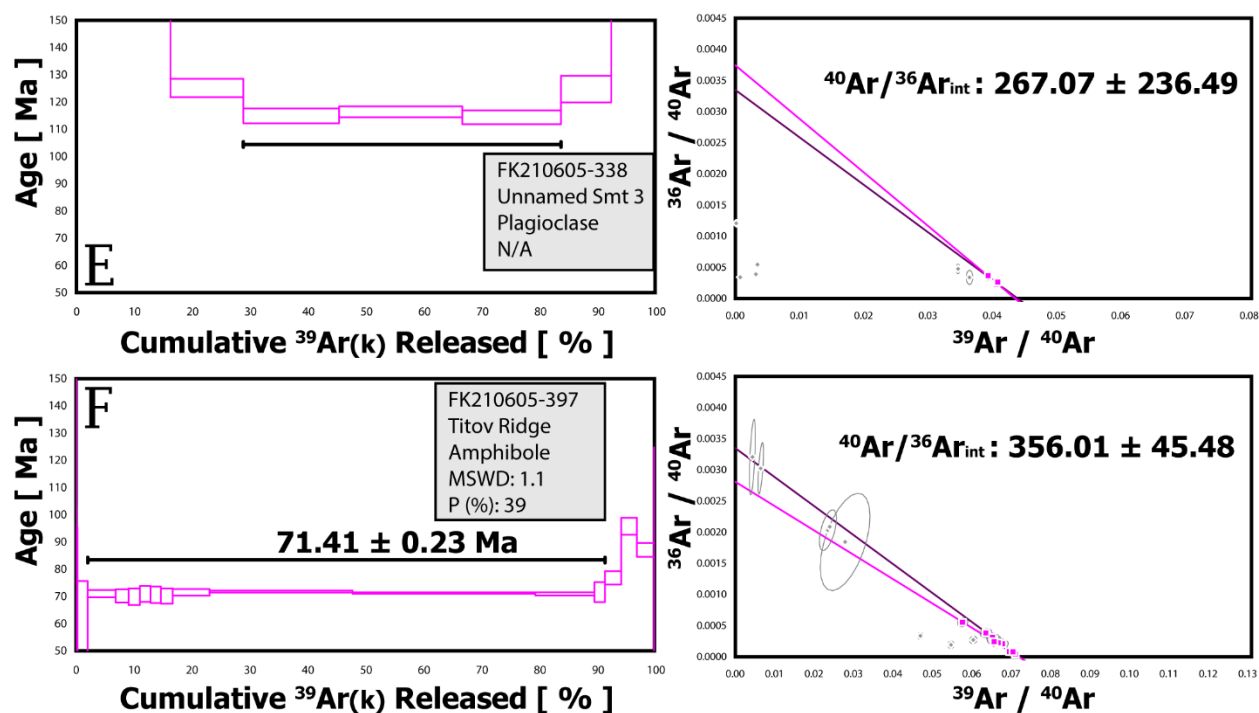


Figure 19: Age determinations and inverse isochron results from incremental $^{40}\text{Ar}/^{39}\text{Ar}$ heating experiments. Uncertainties are reported at the 95% confidence level. Purple rectangular segments in the left column represent individual heating steps and the corresponding dark line segments represent concordant age plateaus. Purple lines on the right column are inverse isochrons that represent sample $^{40}\text{Ar}/^{36}\text{Ar}$ values. The black lines reference $^{40}\text{Ar}/^{36}\text{Ar}$ atmospheric value isochrons. The pink squares are individual sample values shown with error ellipses. Grey circles are heating steps outside of 2σ and thus excluded from isochron interpretations. (E) FK210605-338, (F) FK210605-397.

Chapter 4: Discussion

4.1 Geochemical trends

Geochemical interpretations often rely on unaltered rock samples to accurately discern valuable information regarding the mantle source behavior and processes. However, secondary mineralization, such as phosphorization, amygdule growth (e.g., zeolite and carbonate minerals) and Fe-Mn crustal accumulation were prevalent in all hand samples (Figure 6). Pervasive alteration of olivine phenocrysts into iddingsite was common and palagonized glass (Figure 7E) is abundant in petrographic thin sections, as well as the presence of secondary calcite and zeolite amygdule mineralization (Figure 7H). The conversion from basalt glass to palagonite in a low-temperature submarine environment has been shown to reduce SiO₂ concentrations, while increasing the concentration of other elements (e.g., Ti₂O, Al₂O₃,) (Staudigel and Hart, 1983; He et al., 2022). Therefore, the effects of palagonite can affect the classification of submarine lava flows. Figure 20 illustrates palagonization effects on major elements concentrations as a function of TiO₂ concentrations. The presence of palagonite is shown to decrease both Al₂O₃ (Figure 20A) and SiO₂ (Figure 20B) while increasing TiO₂. A lack of excess MnO with respect to TiO₂ demonstrates that the samples lack evidence of FeMn crustal contamination as a control on palagonization (Figure 20C).

Phosphorite mineralization (Figure 7F) is another low-temperature seawater control process that may affect whole rock chemistry. This alteration process can enrich HREE, influencing garnet stability field interpretations based on REE patterns (Geldmacher et al., 2023). Calculations of $Y/Y^* (Y_{PM} / \sqrt{(Dy * Ho)_{PM}})$ illustrate the preferential partition of Y with respect to Dy and Ho, which has similar compatibilities in dry mantle melting. The concentration of

yttrium (Y) is however more affected by the presence of phosphorite, thus generating Y anomalies when present. There is no clear relationship between individual seamount structures and phosphorite contamination in the sample suites (Figure 21). The Y/Y^* values for HBI seamounts range from 0.91 to 2.17. All values greater than 1.2 are then classified as altered by means of phosphorite contamination and are marked with red symbols in Figure 21 that include NA112-005, -008 (Swains Island) FK210605-353 (Unnamed Seamount 3), and FK210605-448 (Lelei). There is a trend between high Y/Y^* and decreasing $(Dy/Yb)_{PM}$, which indicates that the HREE slopes are flattened and even turned positive (Figure 16) by phosphorization of these lava flows and REE trends should not be used to interpret mantle melting dynamics. The other lava flows in this study are not affected by phosphorite and their high field strength element (HFSE) systematics are likely reflective of the original lava flow.

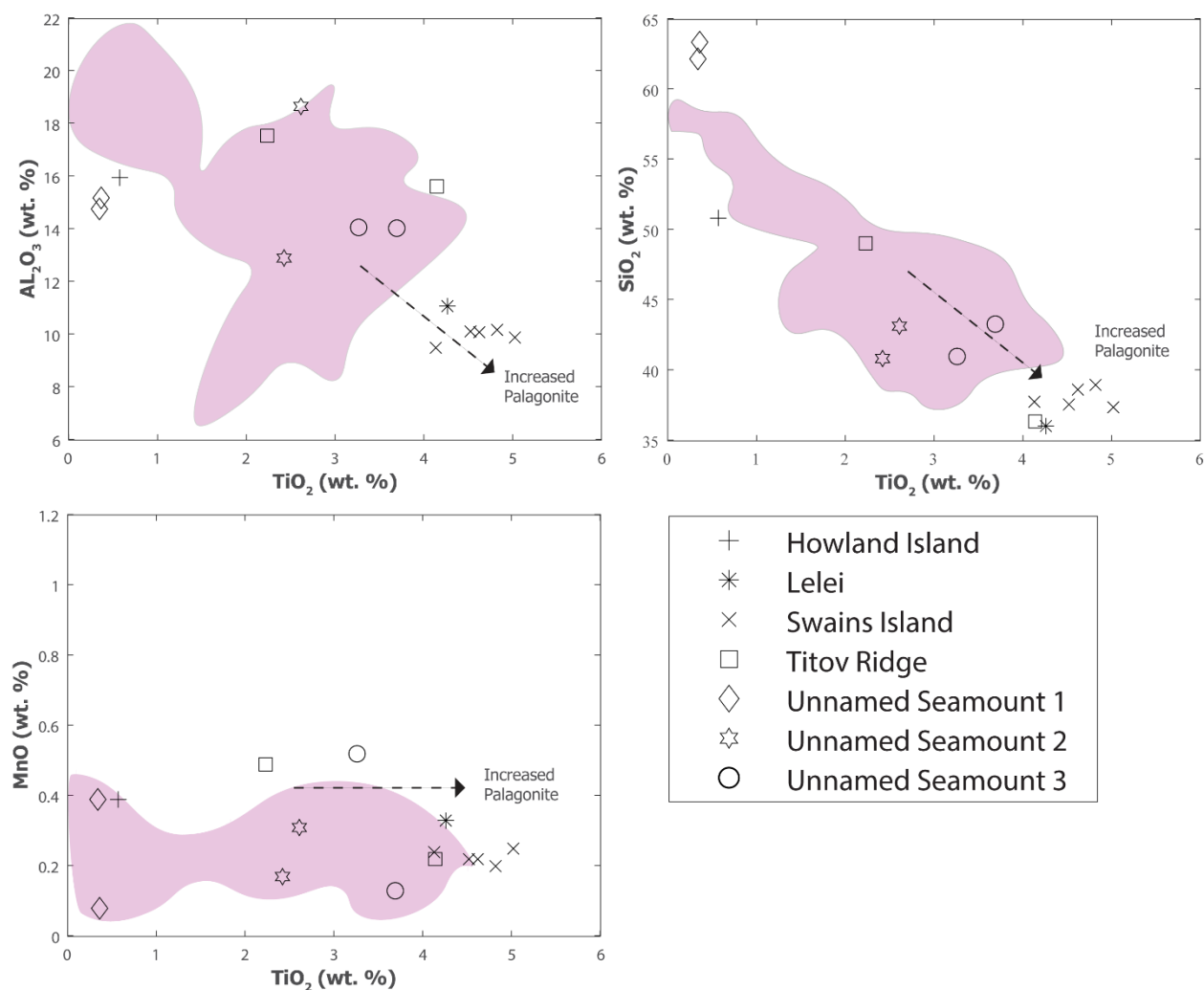


Figure 20: Scatter plots illustrating the effects of seawater alteration on whole rock chemistry. Pink fields represent a range of Cook-Austral Islands OIBs that were downloaded from the GEOROC database (<https://georoc.eu/>). Dashed arrows point in the direction of increased palagonization as a function of an increase in TiO_2 concentrations and a decrease in Al_2O_3 and SiO_2 concentrations. Low MnO suggests no FeMn crustal contamination.

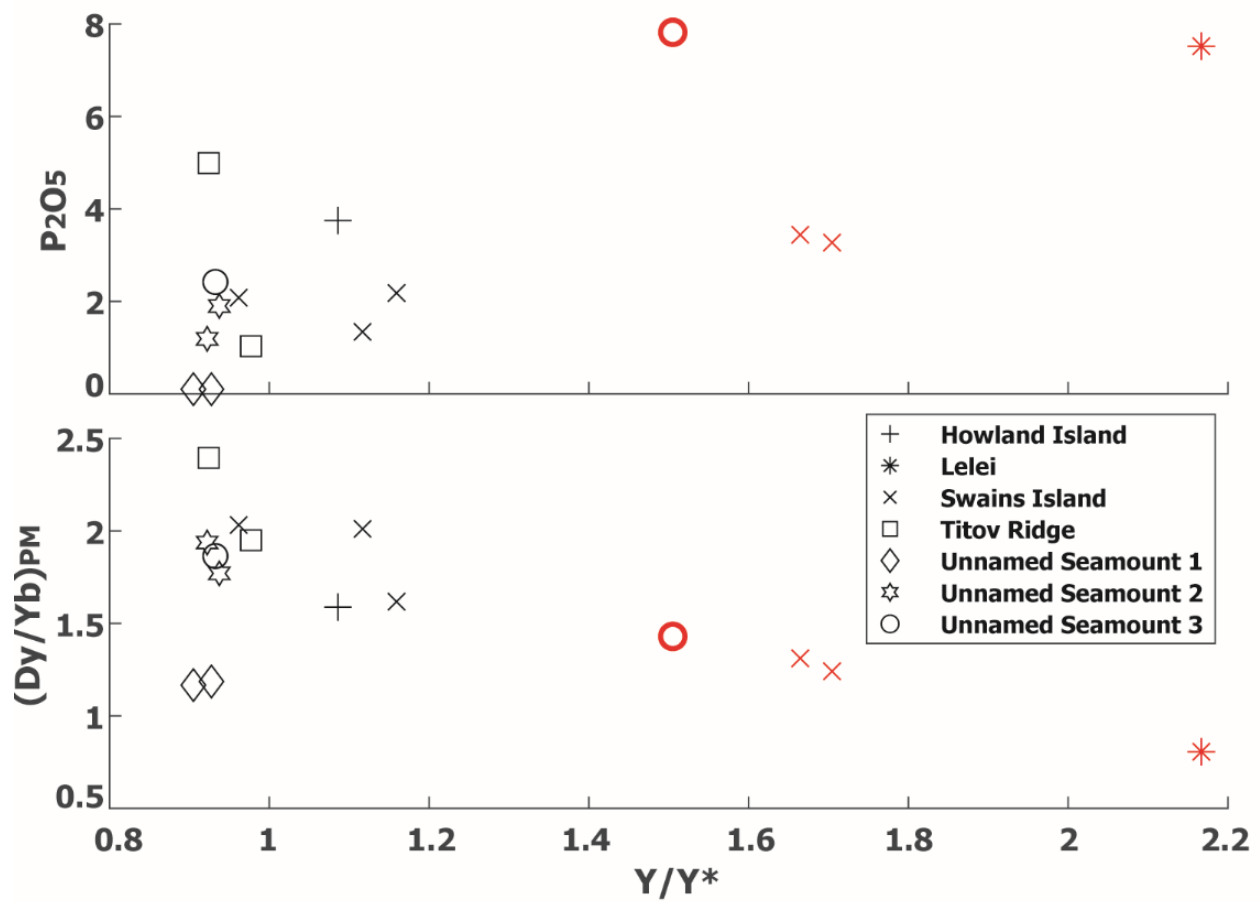


Figure 21: Y/Y^* plots illustrating phosphorization effects on lava flow samples in red markings. Yttrium concentrations increase with respect to dysprosium and holmium concentrations due to the preferential partition of yttrium into phosphorite. Red symbols indicate samples with significant phosphorite contamination.

New trace element concentration data from Swains Island and the Howland and Baker EEZ may provide insight into the magmatic processes that formed them. The severity of seawater alteration, however, considerably inhibits chemical interpretations involving large ion lithophile elements (LILEs). This is largely due to the LILEs higher solubility in seawater and affinity for clay and carbonate minerals. Observations of fluid-immobile HFSEs provide the essential context of more stable element behavior that can be evaluated to better understand these processes, including mantle melting depth and the degree of mantle melting. The depth of melting is interpreted from the fractionation and relative depletion of HREEs, due to the tendency of those elements to partition into the garnet residuum at greater depths (McKenzie and O’Nions, 1991). Similarly, the degree of melting is interpreted from fractionation and depletion of LREEs. The proxies for these systems are shown as Dy/Yb and La/Sm, respectively, and normalized to primitive mantle values (Figure 22; Sun and McDonough, 1989). The high Dy/Yb (~1.6) are consistent with deeper melting mineral phases (e.g., garnet lherzolite). However, phosphate minerals may also incorporate HREEs, leading to false interpretations. With the exception of the trachytes found at Unnamed Seamount 1, samples with Dy/Yb ratios under 1.6 are affected by phosphorite and are considered contaminated and thus not reliable when interpreting relative melting depth (Red Symbols; Figures 21 to 23). Excluding the samples recovered from Unnamed Seamount 3, all of the samples exhibit high La/Sm normalized to primitive mantle values (>3.0). The high La/Sm ratios indicate a lower degree of melting that is associated with incompatible element enriched mantle reservoirs (O’Neill, 2016). However, care must be taken when interpreting these first-order observations due to limited sample size.

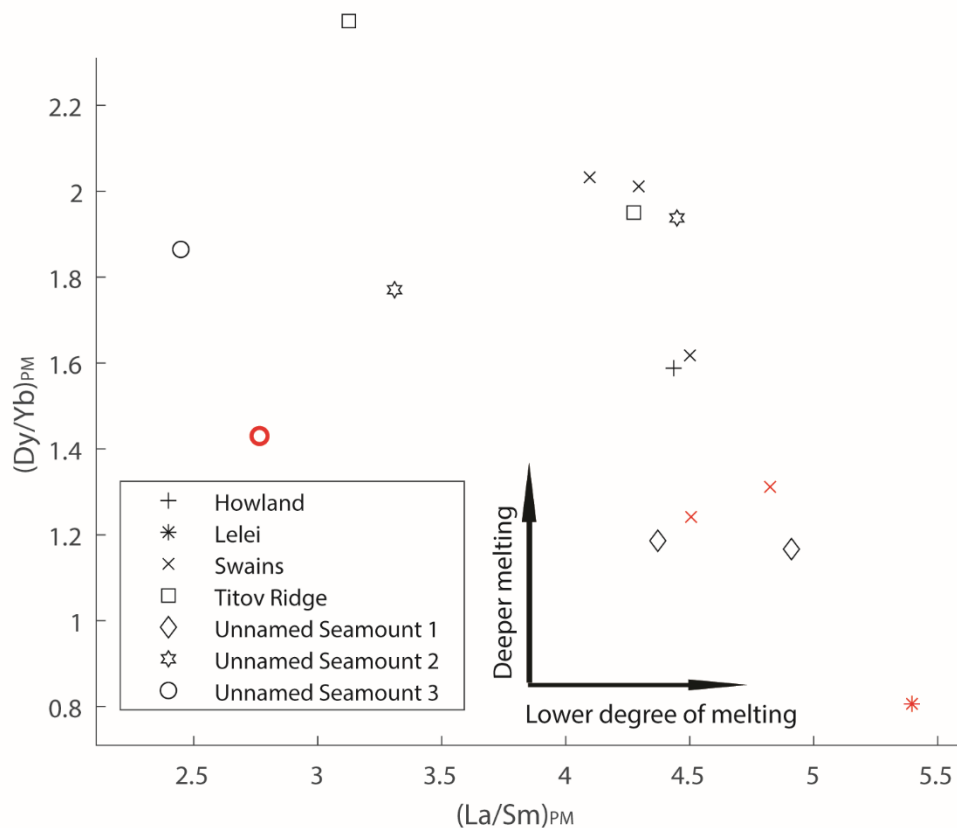


Figure 22: Depth of melting and degree of melting fractionation trends of HREEs and LREEs for the Swains Island and the Howland and Baker Island EEZ seamounts using the $(Dy/Yb)_{PM}$ vs. $(La/Sm)_{PM}$ system. PM is normalized values to primitive mantle (Sun and McDonough, 1989). Directional annotations represent first-order trends and do not fully capture the complexity of source reservoir variation. Symbols labeled in red are considered contaminated by phosphorite and are unreliable for mantle interpretations.

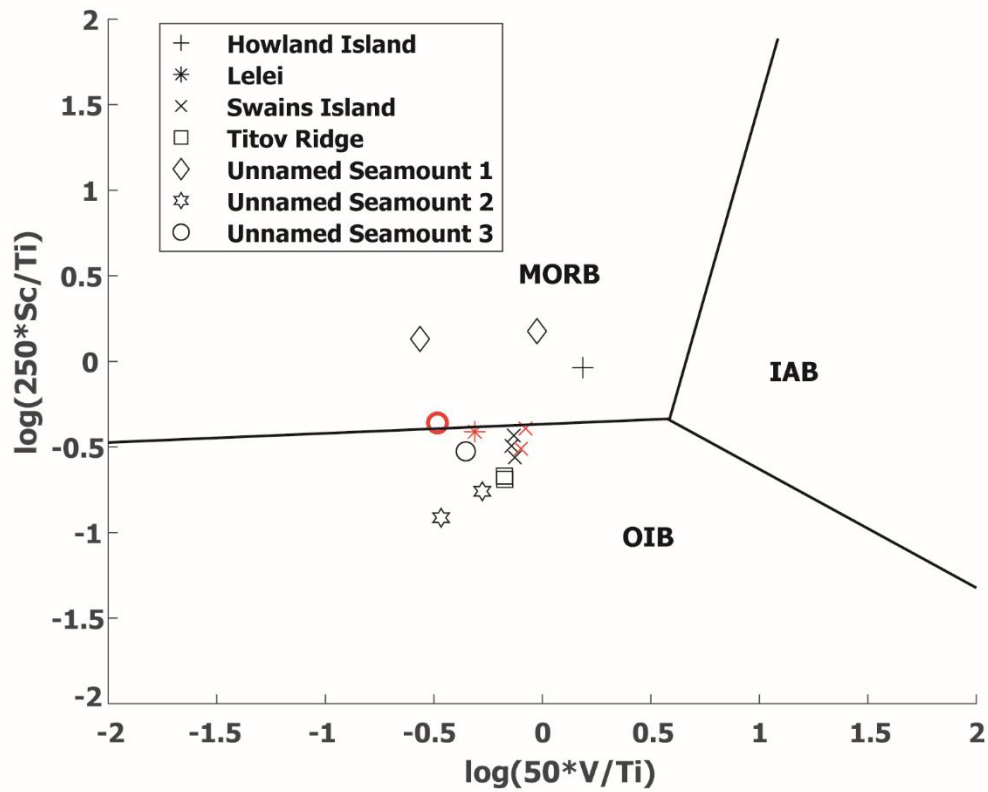


Figure 23: Linear discrimination analysis of ocean basalt fields and a first order classification for categorizing seamounts. MORB = mid-ocean ridge basalt. OIB = ocean island basalt. IAB = island arc basalt.(Vermeesch, 2006).

To better understand mantle sources of the samples, an evaluation of statistically derived discrimination diagrams can be utilized. Linear discrimination analyses of Ti-V-Sc systematics in oceanic basalts have been shown to discern tectonic affinity (Vermeesch, 2006). The majority of the samples used in this study fall within, or near the OIB field when plotted in log-ratio space, with the exception of samples from Unnamed Seamount 1 and Howland Island (Figure 23). The classifications of the MORB designated samples are likely the result of Ti depletions in those samples that are not reflective of a reservoir source. An alternative approach to discerning the degree of partial melting in the mantle is to compare the elemental ratios of Th/Yb and Nb/Yb (Figure 24). In dry melting scenarios, Th concentrates in residual melt phases and Nb is depleted in arc volcanism settings. Therefore, increasing Nb and Th with respect to Yb can be used to interpret lower degrees of melting (Pearce, 2007). With the expectation of the phosphorite contaminated sample at Lelei, the seamounts in this study appear to originate from a low degree of melting that is consistent with OIBs.

To summarize, the suite of seamounts appears to originate from an OIB source with relatively deep melting (~80-90 km). The exception is Unnamed Seamount 1, which represents shallow mantle melting of an enriched reservoir. Howland Island, Titov Ridge, Swains Island, Unnamed Seamount 2, and Unnamed Seamount 3 signatures are consistent with a plume source. Therefore, it is likely that Unnamed Seamount 1 has a different origination mechanism. These trace element fractionation patterns can be coupled with high precision age determination interpretations to better discern seamount sources.

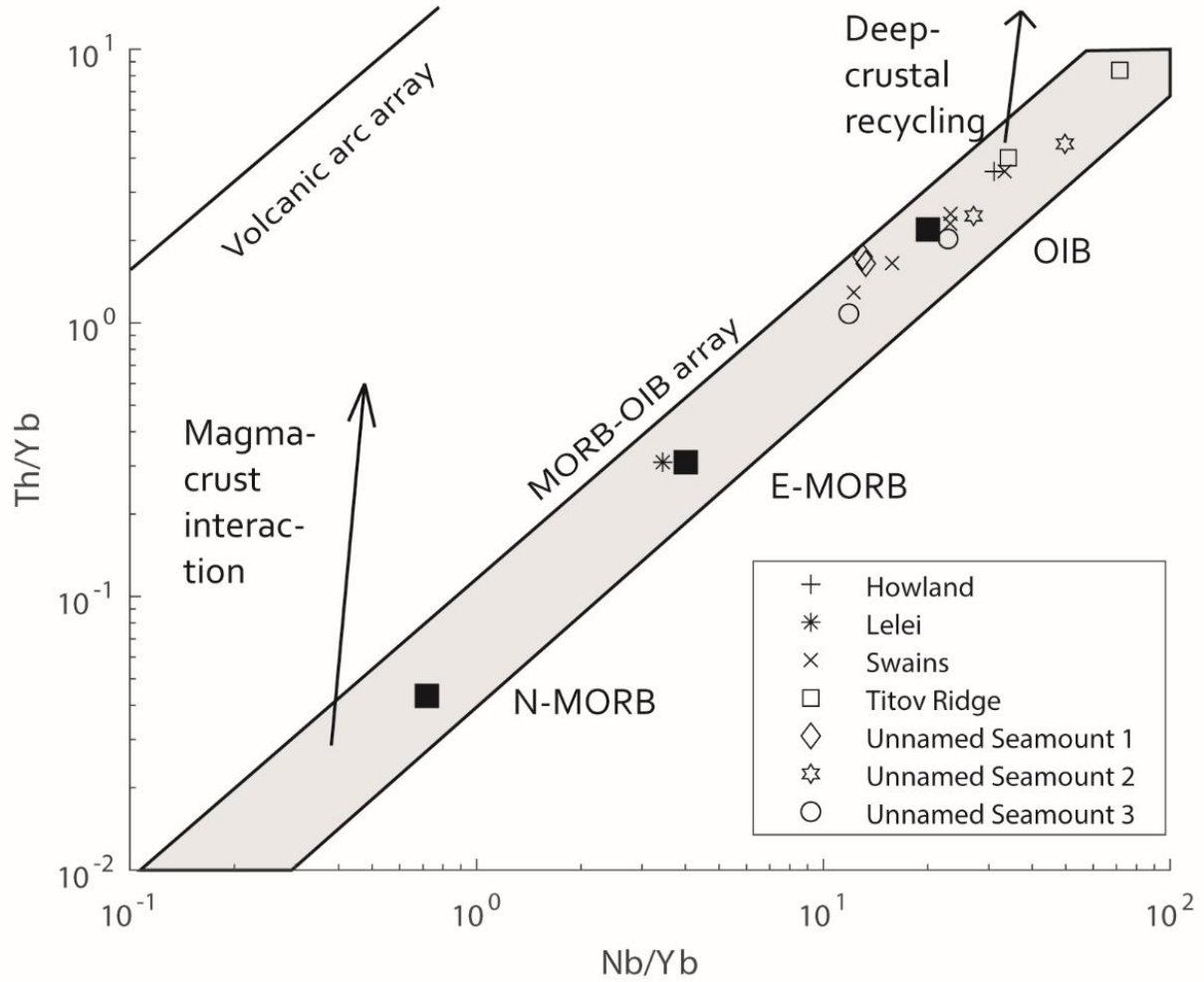


Figure 24: Th/Yb and Nb/Yb ratios compared to MORB and OIB arrays. Nb depletion patterns with respect to Th enrichment indicates crustal component interactions. Annotations and fields after Pearce (2007). N-MORB = normal mid-ocean ridge basalt. E-MORB = enriched mid-ocean ridge basalt. E-MORB is a relatively more enriched depleted MORB source that has slightly elevated alkali concentrations.

4.2 $^{40}\text{Ar}/^{39}\text{Ar}$ geochronology

The lava flow ages in the Howland and Baker EEZ cover a large temporal range from 124.2 to 70.4 Ma (Koppers et al., 2007; This Study). Variations in age plateaus are observed to some degree in all samples. Figure 18A and Figure 18B illustrate the effects of older apparent ages at both low and high temperature steps due to the presence of non-atmospheric initial radiogenic ^{40}Ar . The addition of potassium from secondary mineralization phases leads to excess ^{40}Ar that degasses at lower temperatures, thus ^{40}Ar released at lower heating steps can be attributed to the presence of residual clays post leaching (Schaen et al., 2021). Similarly, excess ^{40}Ar can be trapped within melt inclusions in the crystal lattice. Subsequent heating steps of melt inclusions then leads to older apparent ages during higher temperature degassing. The effects of excess ^{40}Ar at low and high temperatures are emphasized in plagioclase separates (Figure 18C). An additional control on age plateaus is the loss of ^{40}Ar during partial degassing. The younger ages in lower heating steps shown in Figure 18D and Figure 19F are attributed to a loss of ^{40}Ar after crystallization and is indicative of the ^{40}Ar clock resetting after a thermal diffusion event. Lastly, Figure 19E exhibits a saddle shape plateau with only three contiguous heating steps.

Sample FK210605-338 from Unnamed Seamount 3 (Figure 17) did not produce a concordant age plateau that fulfilled the requirement of five continuous heating steps (Figure 19E). The older age is likely recording alteration from low temperature heating steps. Due to the scarcity of plagioclase crystals in this sample, a markedly small fraction of mineral separate (~1.0 mg) was analyzed. As a result, the presented *ca.* 115 Ma age is not reported as a final age and is instead attributed to an alteration age resulting from excess ^{40}Ar . However, the neighboring Unnamed Seamount 2 (FK210605-307) produced a concordant age of 85.61 ± 0.14 Ma. Though Unnamed Seamount 2 and Unnamed Seamount 3 are classified in this study as separate structures (Figure 17), their close proximity and similar whole rock major and trace element signatures (Figure 14, 15B) suggest a common origin.

The remaining samples from the HBI EEZ produced concordant age plateaus that can be used to constrain the timing of volcanism. Samples from Howland Island (FK210605-138) and Titov Ridge (FK210605-397) fit the first order geometric and temporal constraints for the Macdonald Hotspot (Figure 17) and are discussed further in Chapter 4. Samples from Unnamed Seamount 1 (FK210605-072, -080) reveal older ages (~124 Ma) and felsic compositions with unusually high silica concentrations for submarine lava flows (Figure 14). The origin of this seamount is presented in Chapter 5.

4.3 The origin of Unknown Seamounts 2 and 3

Unnamed Seamount 2 and Unnamed Seamount 3 are located near the western reaches of the HBI EEZ (Figure 17). The lava flows recovered from both seamounts have REE patterns indicating relatively deep melting of an enriched mantle source (Figure 16; Figure 22; O'Neill, 2016). The HFSE discrimination diagrams indicate the lava flows have OIB-like affinity as well

(Figure 23-24). An amphibole phenocryst separate from FK210605-307 provided a concordant age of 85.61 ± 0.14 Ma for the Unnamed Seamount 2 lava flow. No age determinations are reported from Unnamed Seamount 3 but the proximal location to Unnamed Seamount 2, coupled with very similar lava flow trace element concentrations and patterns (Figure 15B), indicate the seamounts likely share a similar geodynamic driver. However, the timing of emplacement of Unnamed Seamount 3 remains unresolved and further sampling is required to confirm associated emplacement. Resolving the formation mechanism of these seamounts remains an outstanding question, largely due to the absence of proximal active volcanism at the time of their formation. The seamounts are fairly isolated and there are no nearby seamounts that suggest common emplacement, however, a few hypothetical origination mechanisms are provided below.

One possible mechanism for the emplacement of the seamounts is lithospheric extension-driven volcanism. During periods of extensional deformation, the lithosphere may thin, resulting in asthenosphere rising and melting via decompression (McKenzie and Bickle, 1988). This process typically generates small volumes of melt, except when coupled with tectonic driven upwelling at mid-ocean ridges. The Unnamed Seamounts 2 and 3 reside next to the Central Pacific Fracture Zone (Figure 17), which is an ancient transform fault that once offset a segment of the Pacific-Phoenix spreading center (Nakanishi et al., 1992). Thus, the preexisting lithosphere weakness may have provided pathways to enhance melt emplacement during a pulse of localized extension. Currently, no other seamounts proximal to the fracture zone have been mapped or sampled that may provide additional insight into low volume decompression melting in the area. However, the OIB-like chemical compositions (Figure 15B) infer a deeper and more enriched melting source then would be provided by shallow asthenosphere decompression during extension. The lava flow

chemistry, coupled with the lack of evidence for an event that would cause significant thinning in the lithosphere indicate that extension was likely not the driver of volcanism.

A second hypothesis is that distal channelization of plume melts drove the formation of the seamounts. Plume channelization is a process in which thin plume-fed partial melt channels form at the lithosphere-asthenosphere boundary and migrate distally from the plume (Naif et al., 2023). The channels are thought to be widespread and long-lived features in which the partial melting of plume material sources distal intraplate volcanism that escaped from the channel to the surface through a major tectonic event. In the case of Unnamed Seamount 2 and Unnamed Seamount 3, the feeder source for channelization could be the Macdonald plume, which would reside to the northeast of Unnamed Seamount 2 and 3 in agreement with the 85.61 ± 0.14 Ma age plateau, or the Rurutu-Arago plume, which would have been residing beneath the lithosphere farther to the West. This hypothesis remains speculative due to a lack of major tectonic events in the region during the seamounts' emplacement that would have triggered channelized melt to escape.

A third potential mechanism could be poorly understood episodes of mantle melting, which are compositionally similar to plumes but very short-lived. The HBI EEZ region represents a late Cretaceous analog to the modern Cook-Austral Islands region (Koppers et al., 2007; Konter et al., 2008) (discussed further in Chapter 5). Within the modern Cook-Austral region resides short-lived melting anomalies, such as the Rarotonga 'hotspot', which only appears to have sourced volcanism in a restricted region (one or two seamounts) over a short period of time (<3 Ma) (e.g., Dalrymple et al., 1975; Rose and Koppers, 2019; Jackson et al., 2020). The origin of these Rarotonga-type hotspots is debated, as it may represent a new or poorly expressed mantle hotspot (Chauvel et al., 1997) or melting of small diffuse mantle anomalies "seeded" by a local lithospheric instability or structural variation (Lassiter et al., 2003). Unnamed Seamount 2 and 3 are likely Cretaceous

analogs for similar processes, however, without further geochemical constraints or sampling of proximal seamounts it is impractical to classify their origin further. Therefore, the remainder of this study focuses on the seamounts ascribed to hotspot volcanism (Chapter 5) and the enigmatic 124 Ma Unnamed Seamount 1 (Chapter 6).

Chapter 5: The Surface Expression of the Macdonald Hotspot from Cretaceous to Modern Day

5.1 Plume and age progressions within the Cook-Austral Islands

The Cook-Austral Islands volcanic chain consists of multiple trends identified by independent age progressions and isotopic variations among erupted lava flows (Figure 3; Figure 25). Located in the South Pacific (~25°S, 150°W) and west of the East Pacific Rise, the Cook-Austral Islands span roughly 2000 km and trend in a NW-SW orientation. With the advancement of $^{40}\text{Ar}/^{39}\text{Ar}$ geochronology, four trends have been identified by age and chemical variations (Macdonald, Rurutu, Raivavae, and Rarotonga), with at least two clearly resolvable hotspot tracks (Rose and Koppers, 2019). Currently, the Raivavae and Rarotonga trends remain speculative as they are based off one or two seamounts and will not be considered further here. The two resolvable hotspots are sourced from the Rurutu-Arago plume that currently underlies Arago seamount (23° S, 150° W; Bonneville et al., 2002) and the Macdonald plume underlying Macdonald seamount (29° S, 140° W; Rose and Koppers, 2019). The Macdonald is often overprinted by the Rurutu-Arago (e.g., young Rurutu and older Rurutu). This study recognizes the Macdonald plume for producing volcanism on Marotiri, Raivavae, Tubuai, older Rurutu lava flows, Rimatara and Mangaia Islands (Figure 25). The Rurutu-Arago hotspot trend includes young Rurutu, Mauke, Mitiaro and Atiu islands. Both plumes show evidence of being active from at least the Miocene to the present (McNutt et al., 1997; Bonneville et al., 2006; Koppers et al., 2007; Hanyu et al., 2013; Rose and Koppers, 2019; Buff et al., 2021).

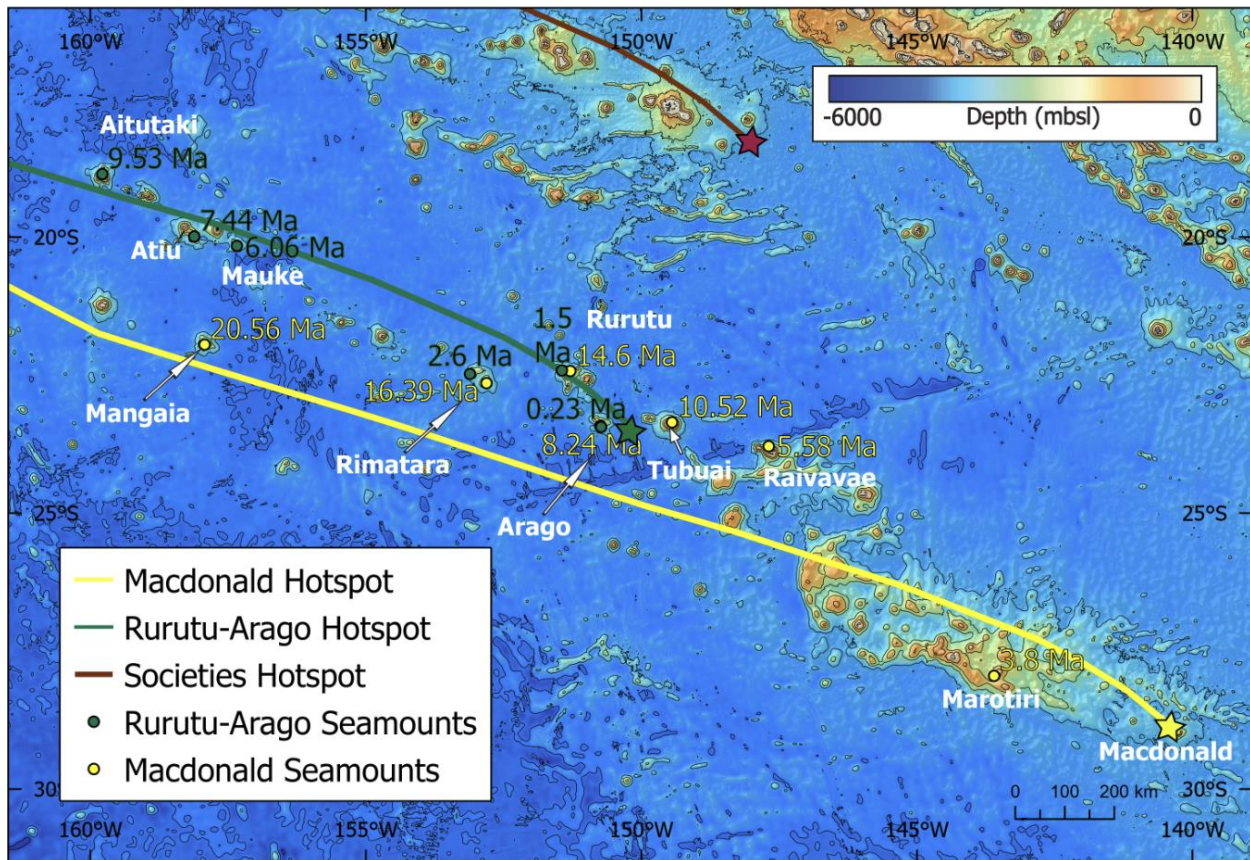


Figure 25: Regional map of the Cook-Austral Islands. Contour intervals are shown at 1000 m intervals. Yellow circles are age determinations representing the Macdonald hotspot derived seamounts and green circles are age determinations representing seamounts sourced from the Rurutu-Arago hotspot. The Macdonald hotspot is responsible for the older volcanism on Rurutu island as well as Marotiri, Raivavae, Rimatara, and Mangaia islands and is volcanically active at the Macdonald seamount. The nearby Rurutu-Arago hotspot is volcanically active at the Arago seamount and includes the younger Rurutu lava flows, Mauke, and Atiu islands. A westward age progression for both hotspots is resolvable from the Miocene to the present.

The Rurutu-Arago and Macdonald hotspot tracks are age-progressive seamount chains hosting volcanoes that exhibit HIMU compositions, with the Macdonald hotspot producing the most radiogenic Pb isotopic signatures found in the Pacific basin (Chauvel et al., 1992; Jackson et al., 2020). These isotopic characteristics are attributed to ancient (>2 Ga) subducted lithosphere that has been reincorporated into the deepest portions of the mantle (e.g., Willbold and Stracke, 2006). Lava flows from Mangaia Island, which is inferred to have been formed from the Macdonald plume, contains some of the most radiogenic HIMU signatures of any mantle-derived OIB (e.g. $^{206}\text{Pb}/^{204}\text{Pb} > 21$) (Woodhead, 1996). The only other region within the ocean basins where lava flows $^{206}\text{Pb}/^{204}\text{Pb}$ above 21 is found is in Bermuda (Mazza et al., 2019). The driver of volcanism in Bermuda is hypothesized to be related to a pulse of mantle upwelling driven by a slab penetrating through the mantle transition zone (Mazza et al., 2019; Huang et al., 2020). Thus, the Bermuda region of extreme HIMU isotopic signatures is correlated with a short-lived (<10 Ma) pulse of hotspot volcanism. Work on mapping the extent of Rurutu-Arago derived volcanism has resulted in a continuous seamount track extending from the Cook-Austral (Rose and Koppers, 2019), into the Eastern Samoa Seamount Province (Buff et al., 2021), Tuvalu Islands (Konrad et al., 2018), and Gilbert Ridge (Koppers et al., 2007). However, much less focus and sample availability has existed for the Macdonald hotspot track. Konter et al., (2008) suggest that the Macdonald hotspot is a long-lived (>50 Ma) feature that has been producing similar HIMU isotopic lava flows in the Tokelau Islands region of the Pacific (70-61 Ma; Koppers et al., 2007). The findings from these studies warranted further exploration of the Macdonald hotspot track beyond the Tokelau into the HBI region.

5.2 Linking old to young Macdonald (Tokelau Ridge)

Tokelau Ridge is a linear chain of islands, atolls, and seamounts located northwest of Samoa (Figure 26). Notable nearby features include the Manihiki Plateau, a LIP to the southeast that was once part of the larger Ontong-Java-Nui LIP (Taylor, 2006), and the Western Pacific Seamount Province to the northwest. Most of the lithosphere beneath the Tokelau seamounts was formed during the Cretaceous magnetic quiet superchron (123-83 Ma; Olierook et al., 2019), making plate reconstructions during this period and region difficult. However, much of the Tokelau Chain overprints the complex Ellice Basin region, which experienced independent spreading, rotations and then reannealing to the Pacific plate during the Cretaceous normal superchron (Benyshek et al., 2019; Davidson et al., 2023a), further complicating regional lithospheric age determinations. Thus far, all dated seamount lava flows along the Tokelau Chain post-date the end of the superchron, indicating that intraplate volcanism occurred while the region was rotating as part of the Pacific plate (Koppers et al., 2007; Konter et al., 2008).

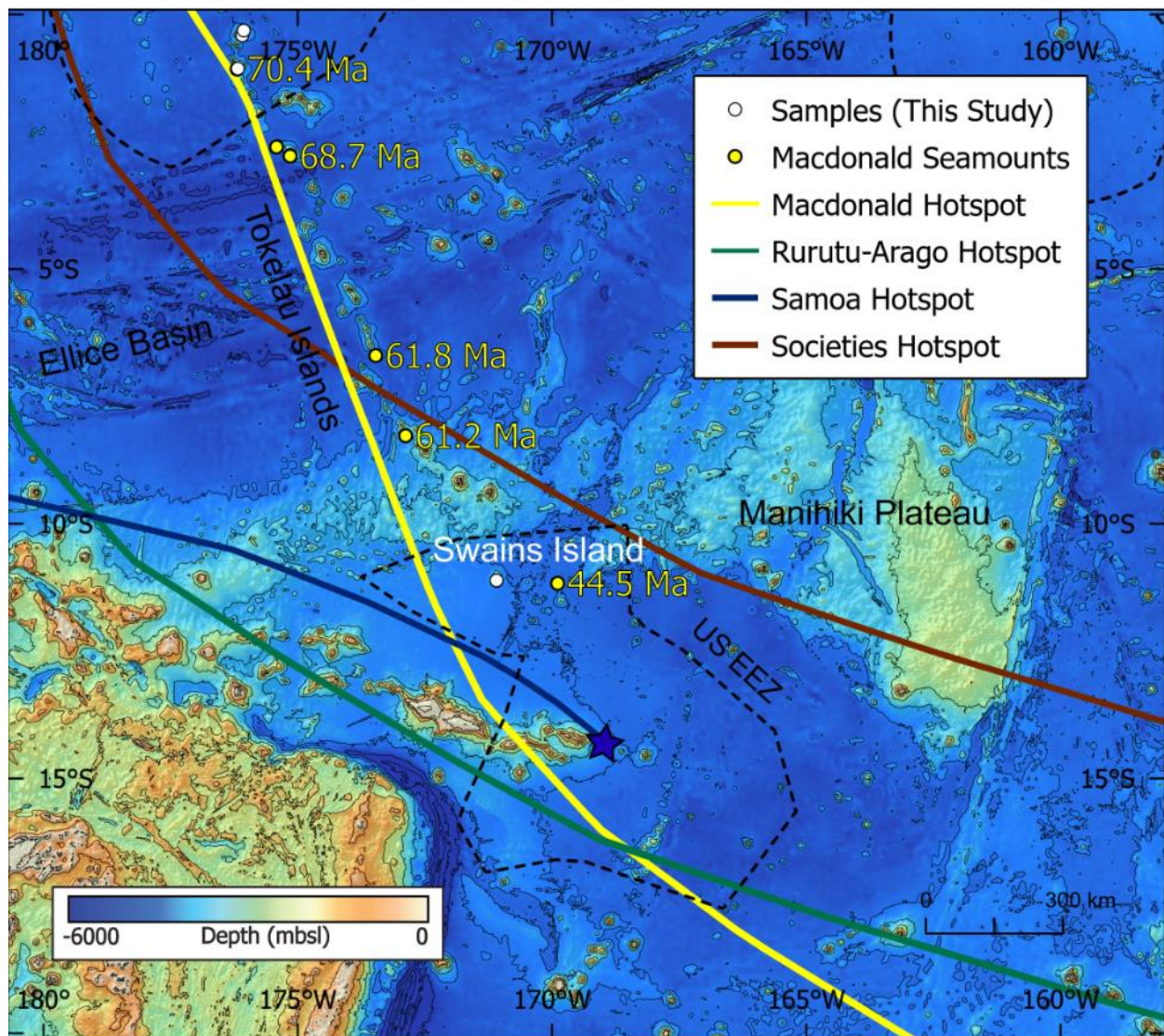


Figure 26: Regional map of the Tokelau Islands and nearby geographic features. Contour intervals are shown at 1000 m intervals. The Macdonald hotspot trajectory records Pacific plate motion and is contemporaneous to the Hawaiian-Emperor bend during the Eocene. The American Samoa unit of the US EEZ is highlighted including the Swains Island sample location. The “Hotspot Highway” lies near Samoa where the Samoan, Rurutu-Arago, and Macdonald plumes have each produced volcanism.

Lead isotopes from lava flows recovered from several Tokelau chain seamounts reveal HIMU-like isotopic signatures (e.g. $^{206}\text{Pb}/^{204}\text{Pb}$ up to 20.77), similar to those observed among younger Macdonald plume sourced volcanism ($^{206}\text{Pb}/^{204}\text{Pb}$ up to 21.92; Woodhead, 1996), suggesting a geochemical relationship between the Tokelau Islands and the Cook-Austral Islands (Konter et al., 2008). Available age determinations from dredged lava flows of the Tokelau Chain range from 74.2 ± 0.7 Ma to 57.7 ± 0.8 Ma (19 experiments; 6 seamounts) and are sparse due to insufficient sampling in the area, a lack of K-bearing phenocrysts and common low temperature aqueous hydrothermal alteration.

A pivotal research area for linking the old and young Macdonald is in the American Samoa unit of the U.S. EEZ (Figure 26). Here, APM models reveal the Macdonald hotspot track changed trajectory due to Pacific plate reorganization at *ca.* 50 Ma (Torsvik et al., 2017). The only lava flow with both Macdonald-like HIMU isotopic signatures and an age determination from this pivotal hotspot track ‘bend’ region comes from Moki Seamount. Unfortunately, the available $^{40}\text{Ar}/^{39}\text{Ar}$ age determination phase from Moki seamount was a low-K clinopyroxene, which resulted in an age of 44.5 ± 10 Ma (Buff et al., 2021). The 45 Ma Moki lava flow age fits the Macdonald age progression, as predicted by APM models (Wessel and Kroenke, 2008; Buff et al., 2021), but the large age uncertainty still calls into doubt the link between the 20-0 Ma Cook-Austral Islands and the 58-74 Ma Tokelau Seamounts. This study sought to bridge the gap through age determinations of Swains Island lava flows collected during expedition NA112. Unfortunately, the Swains Island clinopyroxene age determinations did not contain significant $^{39}\text{Ar}_{(\text{K})}$ and corresponding $^{40}\text{Ar}^*$ to produce concordant age plateaus. Therefore, bridging the gap between the Cook-Austral Islands and Tokelau Islands will require a more rigorous sampling campaign in the region.

5.3 Howland and Baker Island EEZ interpretations

New age determinations from Howland Island (FK210605-138; 73.57 ± 0.28 Ma) from this study and Titov Ridge (FK210605-397; 71.41 ± 0.23 Ma) fit the expected linear progression of hotspot volcanism that is supported by previously published ages and interpretations (Figure 17). However, to better evaluate the relationship between the model and individual seamounts, it is prudent to compare the model used in this study, among others, with all seamounts that are hypothesized to originate from the Macdonald hotspot. One approach is to visualize the data by comparing seamount ages to their great circle distance from the hotspot (Figure 27). All figures in this study used the WK08-A model (Wessel and Kroenke, 2008) for hotspot projection. In comparison, the K01 (Koppers et al., 2001) APM model uses fewer stage poles than the WK08-A model. Unlike the previous models that generate best fit Euler poles using the chronology and morphology of hotspot tracks present on the Pacific plate, assuming no independent plume motion, the D12 model (Doubrovine et al., 2012) uses global tomography models to determine independent plume motion, then correct for that motion when generating a hotspot track APM model. The D12 model (Figure 27) produces a strong mismatch to the observed Macdonald hotspot track, indicating (1) the D12 model overcorrects for hotspot motion in the Pacific or (2) the Macdonald hotspot experienced independent plume motion, and the independent motion and aligns well with the fixed hotspot models (WK08-A, K01).

Another method to analyze the geometric relationship between seamounts and a hotspot with which they presumably originate from is to use a technique called hotspotting (Wessel and Kroenke, 1998). The hotspotting technique ‘back-tracks’ seamounts by rotating stage poles to recreate the original seamount coordinates at the time of an age dated lava flow’s emplacement. Since Pacific APM models are built off the assumption of fixed (e.g., Koppers et al., 2001; Wessel

and Kroenke, 2008) or model corrected hotspot tracks (Doubrovine et al., 2012), seamounts of various ages should hotspot back to the active latitude/longitude of volcanism today (Figure 28; Wessel, 2008). All seamounts that are suspected to originate from the Macdonald hotspot, as well as the two samples from this study (Howland Island and Titov Ridge) fall within a close range (~500 km) of the Macdonald seamount, and the presumed present-day location of the Macdonald hotspot. The offsets in the eruptive locations are best explained by both uncertainties in the APM model as well as available lava flows not forming when the seamount was exactly overriding the mantle hotspot. Volcanism among the seamounts can persist for a few million years after the volcano drifts off the apex of the hotspot (e.g., Clague and Dalrymple, 1987). The hotspotting technique assumes the lava flow was emplaced when the seamount was directly over the hotspot. Therefore, if a late stage or post-erosional lava flow (that tends to produce a more readily sample-able veneer over the volcano) is dated, the modeled eruptive location will typically be to the west (emplaced within the last 50 m.y.) and north (emplaced post 50 m.y.) of the current hotspot location. The observed scatter in the hotspotting results (Figure 28) is consistent with this observation and support a long-lived fixed Macdonald origin for the HBI seamounts.

In summary, there appears to be a clear age progression in the Late Cretaceous (up to 74.5 Ma) that is likely to originate from the Macdonald hotspot. Geochemical signatures from Howland Island and Titov Ridge suggest a deep mantle source and ocean island basalt origin. However, future work on the samples used in this study will incorporate Sr-Nd-Pb isotopes to assist in determining a partially recycled mantle source. Now that a long-lived and relatively fixed Macdonald hotspot track has been confirmed, the new data can be used to test the relative fixity of other hotspots.

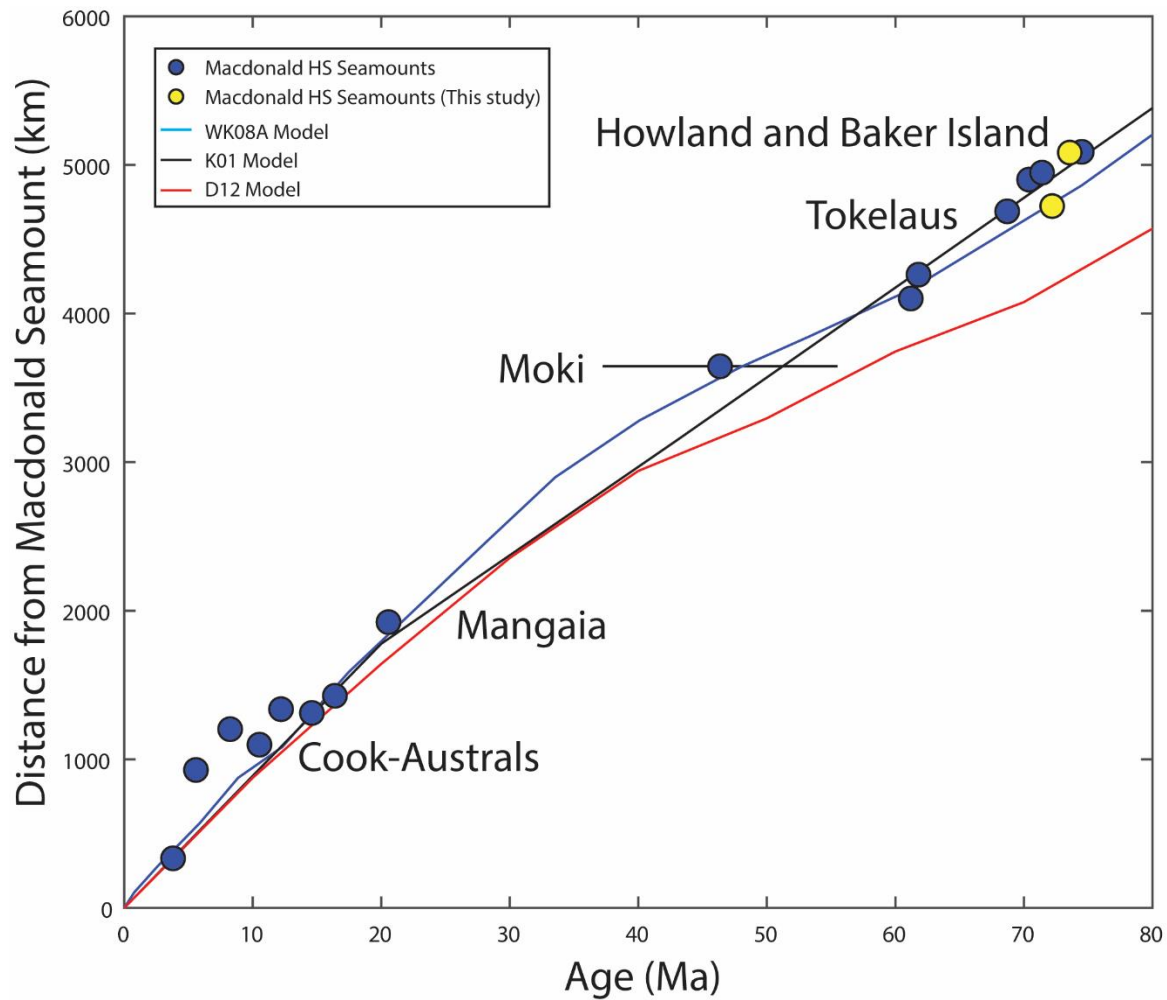


Figure 27: Age distance plot of seamounts suspected to originate from the Macdonald hotspot. Blue circles are individual seamounts from previous studies. Yellow circles are individual seamounts from this study. Solid lines are projected APM models that represent various interpretations of the Macdonald hotspot. Blue line = Wessel & Kroenke (2008). Black line = Koppers et al. (2001). Red line = Doubrovine et al. (2012).

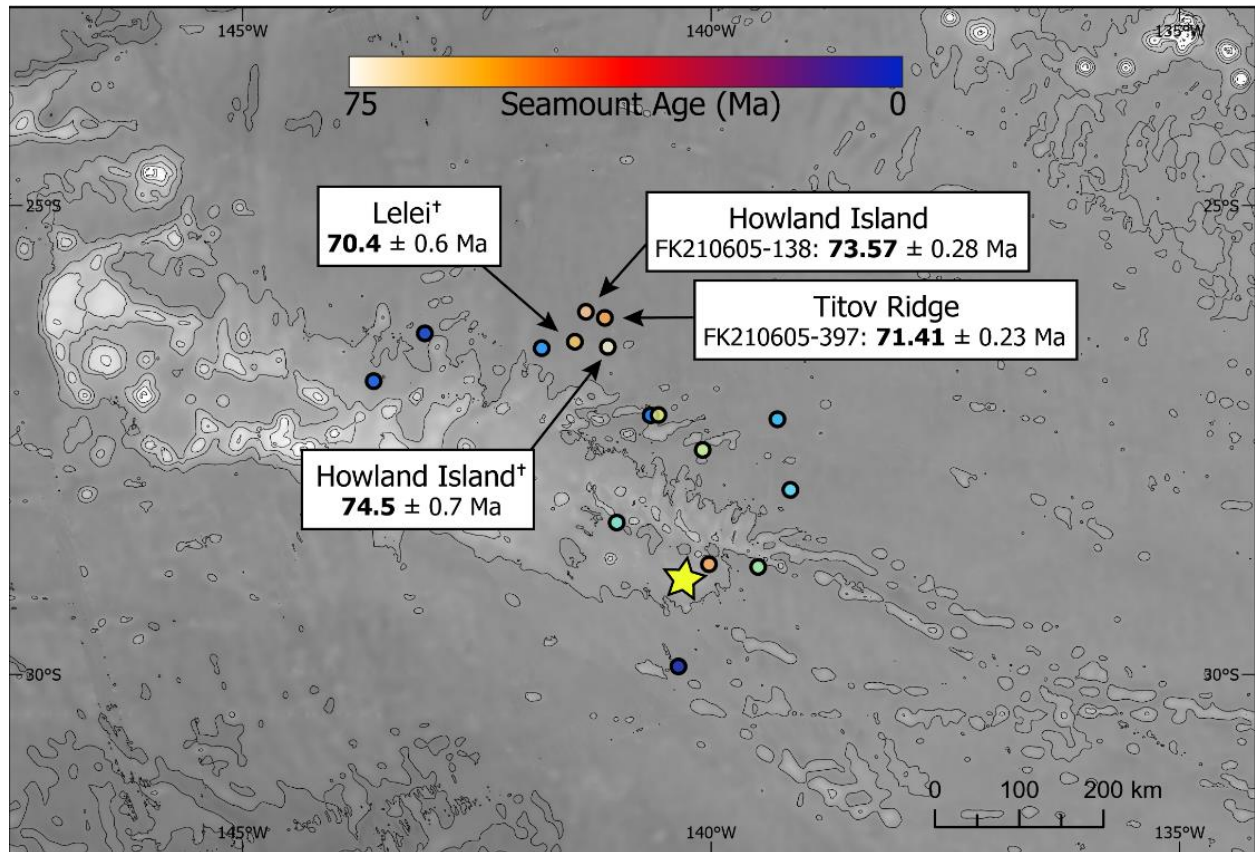


Figure 28: Map of the South Pacific illustrating the hot spotting analytical technique (Wessel and Kroenke, 1998). Stage poles from Wessel and Kroenke (2008) rotate present day seamount coordinates to their eruptive locations. The yellow star indicates the current eruption coordinates of the Macdonald hot spot at the Macdonald seamount. Colored circles specify presumed Macdonald seamounts extending back to the Late Cretaceous. Seamounts with daggers indicate recalculated ages.

5.4 Relative Pacific Plume motion

One of the main axioms this thesis assumes, and presents evidence supporting, is that the Macdonald hotspot stems from a mantle plume that is fixed relative to the convecting asthenosphere and lithosphere. The initial observation of the Hawaiian-Emperor chain's geometry and age progression was interpreted as a fixed plume documenting changes in the Pacific plate motion over time (Morgan, 1972). However, the recognition of plume fixity remains a contentious topic of discussion due to the inherent challenges of observing mantle plumes through time. Pioneering geodynamic mantle flow modeling by Steinberger and O'Connell (1998) indicated that mantle plume conduits are likely advected by mantle flow fields through time and that the surface expression of hotspots likely shift. This model was tested during Ocean Drilling Program leg 197, wherein Emperor seamounts (believed to be sourced from the Hawaiian plume) were drilled. The combined age determinations and paleomagnetic reconstructions of lava flow emplacement latitude indicate that the Hawaii plume was initially $\sim 15^\circ$ north of its current location during the Cretaceous (Tarduno et al., 2003). Tarduno et al., (2003) went on to suggest that the HEB was likely a function of plume motion rather than a significant change in plate motion at *ca.* 50 Ma. The plume motion proposal was challenged by potential observations of true polar wander at that time (e.g., Zheng et al., 2018), increased sampling and age determinations around the HEB (Sharp and Clague, 2006) and observations of coeval 'bends' in other hotspot tracks on the Pacific plate (e.g., Finlayson et al., 2018). However, the debate over how much, if at all, the Hawaiian plume moved is still ongoing.

Recent studies have favored some motion of the Hawaii plume based on available paleomagnetic observations and comparisons to coeval hotspot tracks. In Steinberger et al. (2004), the HEB is suggested to have formed from plate motion coupled with convective mantle flow.

Another initiation mechanism for setting a plume in motion and causing the HEB involves plume capture by a spreading ridge (Tarduno et al., 2009). Finally, deep mantle flow caused by subduction has been hypothesized to alter the geometry of the Pacific LLSVP, thus affecting plume tilt and altering the HEB path (Hassan et al., 2016). Konrad et al. (2018) sought to answer the question of Hawaiian plume motion independent of paleomagnetic interpretations. The authors calculated relative inter-hotspot distances using a best fit interpolated model for dated and undated seamounts along the Hawaii, Louisville, and Rurutu-Arago tracks (Konrad et al., 2018). The distance between the tracks was then calculated as a function of age. Minimal changes in motion were observed before 48 Ma, however, there is a notable change in motion (~1000 km) observed between the Hawaii to Louisville and Hawaii to Rurutu-Arago tracks at 60-50 Ma. Konrad et al., (2018) interpreted the observation as independent movement of the Hawaii plume in the Early Cenozoic, consistent with paleomagnetic observations of Tarduno et al., (2003, 2009).

Contrary to the above work, some studies have suggested that true polar wander during the Early Cenozoic/Late Cretaceous (Gaastra et al., 2022), as well as limited age determinations among the Emperor Seamounts, has resulted in the overestimation of independent Hawaii plume motion. For example, the assessed uncertainties (e.g., along-track uncertainties) in inter-hotspot distances calculated by Gaastra et al., (2022) yield greater errors for inter-hotspot motions than earlier interpretations (Konrad et al., 2018). As a result, fixed hotspot approximations may not be excluded from seamounts extending further back in time (80-48 Ma) as the apparent motion between Hawaii and Louisville are within uncertainty of zero. Therefore, the question of hotspot fixity through time remains open and more data points are required to better refine uncertainties in hotspot track age progressions and geometric reconstructions.

This study adds to the debate surrounding the fixity of Pacific hotspots evaluating the inter-hotspot distances between the Macdonald hotspot (assuming it was active since the Late Cretaceous) and the other established long-lived Pacific seamount trails (i.e., Hawaii, Louisville, Rurutu-Arago; Figure 29). Using a combination of age determinations from this study coupled with those compiled in Konrad et al. (2018), interpolated inter-hotspot distances are calculated using the methods from both Konrad et al. (2018; blue lines Figure 30) and Bono et al. (2019; black circles Figure 30). Bono et al. (2019) employed a simple method to test for inter-hotspot motion by taking a seamount of a given age from one track and calculating the distance to a seamount that was emplaced within 3 Ma on a different track. This results in a lower density of points, but provides the same first order results as Konrad et al.'s. (2018) interpolated hotspot track method (Figures 29 and 30). Moki seamount (44.5 ± 10 Ma; Buff et al., 2021) is excluded from the Macdonald track calculations due to the high age uncertainty. The inter-hotspot distances between the Hawaii and Louisville tracks (Figure 30B) match the results presented in Konrad et al., (2018) and Bono et al. (2019), which indicate that calculations used here are valid.

The Macdonald-Hawaii inter-hotspot distance changed about 500 km (~9% difference) sometime between 60 and 20 Ma (Figure 30A) as compared to the ~1000 km (~12.5% difference) in motion observed between the Hawaii and Louisville tracks during the same time interval (Figure 30B). Similar to the Macdonald-Hawaii results, nominal changes occur between the Macdonald and Louisville hotspots (~300 km, or 12%; Figure 30C), while no significant motion is detected between the Macdonald and Rurutu hotspots (Figure 30D). The observation that the Macdonald plume shows similar relative changes in motion change between both the Hawaii and Louisville plume calls into question the conclusion that the Hawaiian plume moved in the late Cenozoic while the Louisville plume was stationary (Konrad et al., 2018; Bono et al., 2019).

Paleomagnetic analysis of recovered lava flows from the late Cretaceous and early Cenozoic Louisville seamounts (IODP expedition 330) indicates minimal latitudinal shifts for the Louisville plume at the time (Koppers et al., 2012). However, plume motion modeling based on tomography-derived regional mantle flow indicates the plume should have a strong eastward (longitudinal) drift from the Cretaceous to the Eocene (Steinberger, 2000; Koppers et al., 2001). Therefore, based on the relative plume motions calculated here (Figure 30), it appears that the relative motion between the Louisville and Hawaii is likely exaggerated by the independent motion of both plumes, as opposed to just Hawaii plume motion. Thus, these new results support the assessment of Gaastra et al. (2022), that independent plume motion is not as significant as initially proposed in earlier studies. Provided that the maximum difference in inter-hotspot distances between the Cretaceous to modern day are on the order of 9-13% for each comparison (Figure 30), it is likely that individual plumes only experienced a <10% shift in hotspot location from the late Cretaceous to modern day. When considering the large uncertainties involved in APM reconstructions (e.g., O'Neill et al., 2005), this work supports the notion that APM models can be reconstructed accurately from Pacific seamount tracks without correcting for modeled independent plume motion.

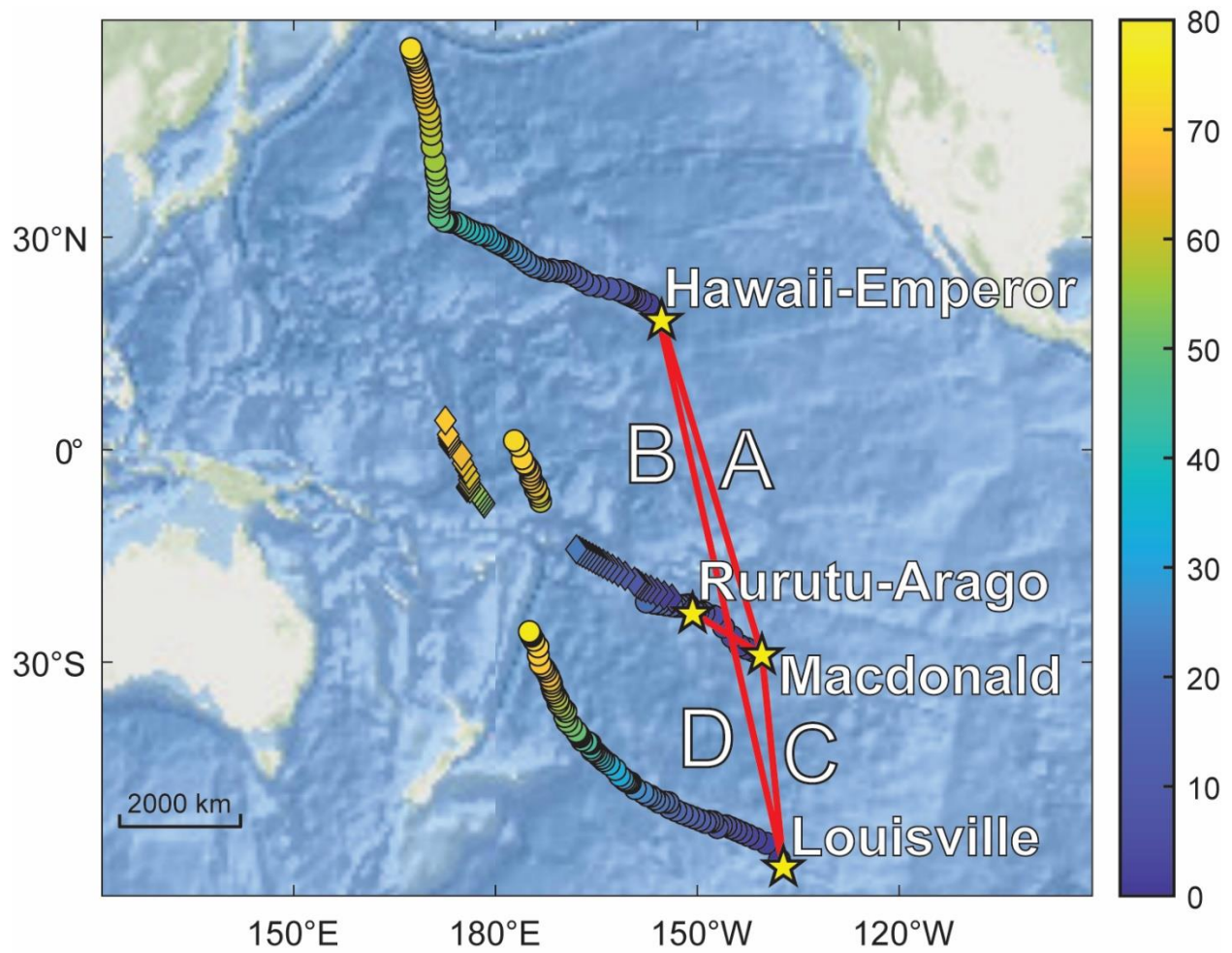


Figure 29: Map of potential long-lived hotspots in the South Pacific. Yellow stars indicate coordinates for active volcanism at a given hotspot. Red lines indicate inter-hotspot distances between present-day volcanism. A = Hawaii-Emperor-Rurutu-Arago. B = Hawaii-Emperor-Louisville. C = Macdonald-Louisville. D = Macdonald-Rurutu-Arago.

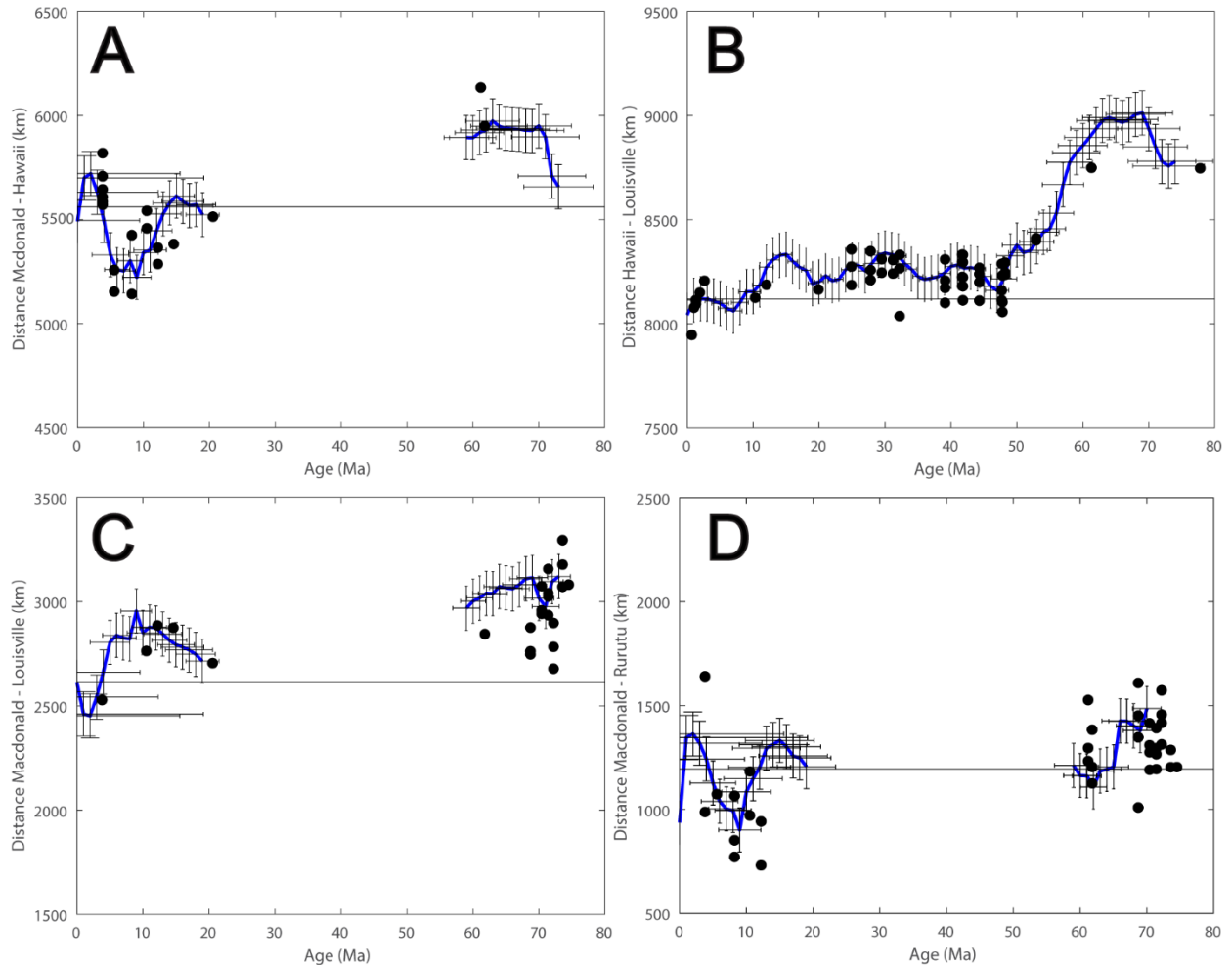


Figure 30: Calculated distances between hotspots as a function of time interpolated model with error bars. Blue lines are calculated distances. Black circles are coeval volcanoes that are separated by less than 3 Ma. Solid Black line is the present-day distance between hotspot tracks. The large data gaps (A, C, D) are unsampled absences in the Macdonald track.

Chapter 6: On the Origin of Barremian-aged Felsic Volcanism in the Howland and Baker Island Region

While the geochemical data and age determinations from Howland Island and Titov Ridge support the hypothesis that the Macdonald is an age-progressive hotspot extending from the Late Cretaceous to the Cenozoic, samples from Unnamed Seamount 1 have a more enigmatic origin. Unnamed Seamount 1 is a volcanic structure located on a bathymetric swell that is best highlighted by a 5200 m contour (Figure 31). The ROV traversed rubbly terrain with rare outcropping lava flows, progressing from volcano flanks to the summit. Two rock samples were collected from the rubble at depths of 2597 and 2498 mbsl. The samples FK210605-072 and FK210605-080 exhibit similar chemistries. Both are felsic trachytes with elevated silica (64.2-64.7 wt.%) and alkali (12.8 wt.%) concentrations and have tephra-like morphologies (Figure 6A, 6B). Trace element concentrations indicate the samples erupted from a shallow melting source ($Dy/Yb < 1.6$). However, the source reservoir chemical characteristics remains unclear. A linear discrimination diagram assigns the samples to the MORB field (Figure 23), yet the Th/Nb enrichment array hints at an OIB source (Figure 24). Separated sanidine crystals from the two-tephra produced concordant age plateaus of 124.17 ± 0.12 (FK210605-072) and 124.22 ± 0.13 (FK210605-080) Ma. The ages clearly do not fit age progression models associated with the Macdonald hotspot (*ca.* 78 Ma) and require a separate interpretation. Furthermore, the felsic nature of the samples and relatively shallower depths of mantle melting are not commonly associated with hotspot volcanism. Therefore, in order to assess the geodynamic process that sourced the seamount, a tectonic reconstruction of the local Pacific basin at *ca.* 124 Ma is required.

Seafloor fabrics, coupled with magnetic lineations, record ancient seafloor spreading directions and can provide insight into paleo-plate boundary configurations. The Pacific plate

records ancient seafloor spreading ranging as far back as the Middle Jurassic (Koppers et al., 2003), and is believed to originate as an ocean transform triple junction between the ancient Farallon, Phoenix, and Izanagi plates (Boschman and Van Hinsbergen, 2016; Tominaga et al., 2021). From *ca.* 180 Ma until *ca.* 140 Ma, the Pacific plate grew from the Pacific-Izanagi, Pacific-Phoenix, and Pacific-Farallon spreading centers in the northwest, south and northeast, respectively (e.g., Torsvik et al., 2019). At approximately 137 Ma, the Magellan spreading center became active, which generated the Magellan microplate in the region proximal to the Unnamed Seamount 1 (Tamaki and Larson, 1988; Figure 31). The spreading ceased during the M9 chron at *ca.* 130 Ma (Tamaki and Larson, 1988; Ogg, 2020). The apparent cessation of regional spreading occurs ~6 Ma prior to the eruption at Unknown Seamount 1, and therefore, is likely unrelated to the eruption at Unnamed Seamount 1. However, crustal formation during the M2n chron (124-125 Ma) is present within the heavily deformed lithosphere to the east of the paleo-Magellan microplate. Thus, it is possible there was widespread lithospheric deformation in the region associated with the adhesion of the Magellan microplate back onto the larger Pacific plate. This deformation may have resulted in regions of increased lithospheric thinning and as such, low-volume decompression melting. One outstanding observation that remains unresolved is the formation of felsic volcanism in low-volume melting scenarios. Although highly speculative provided the limited mapping of the Magellan microplate region coupled with zero seafloor rock sampling, deformation driven volcanism from the potential slow (130-124 Ma) adherence of the Magellan microplate is feasible. However, other major events occurred on the Pacific plate during the Barremian that may also provide clues into the origin of this enigmatic volcanic event.

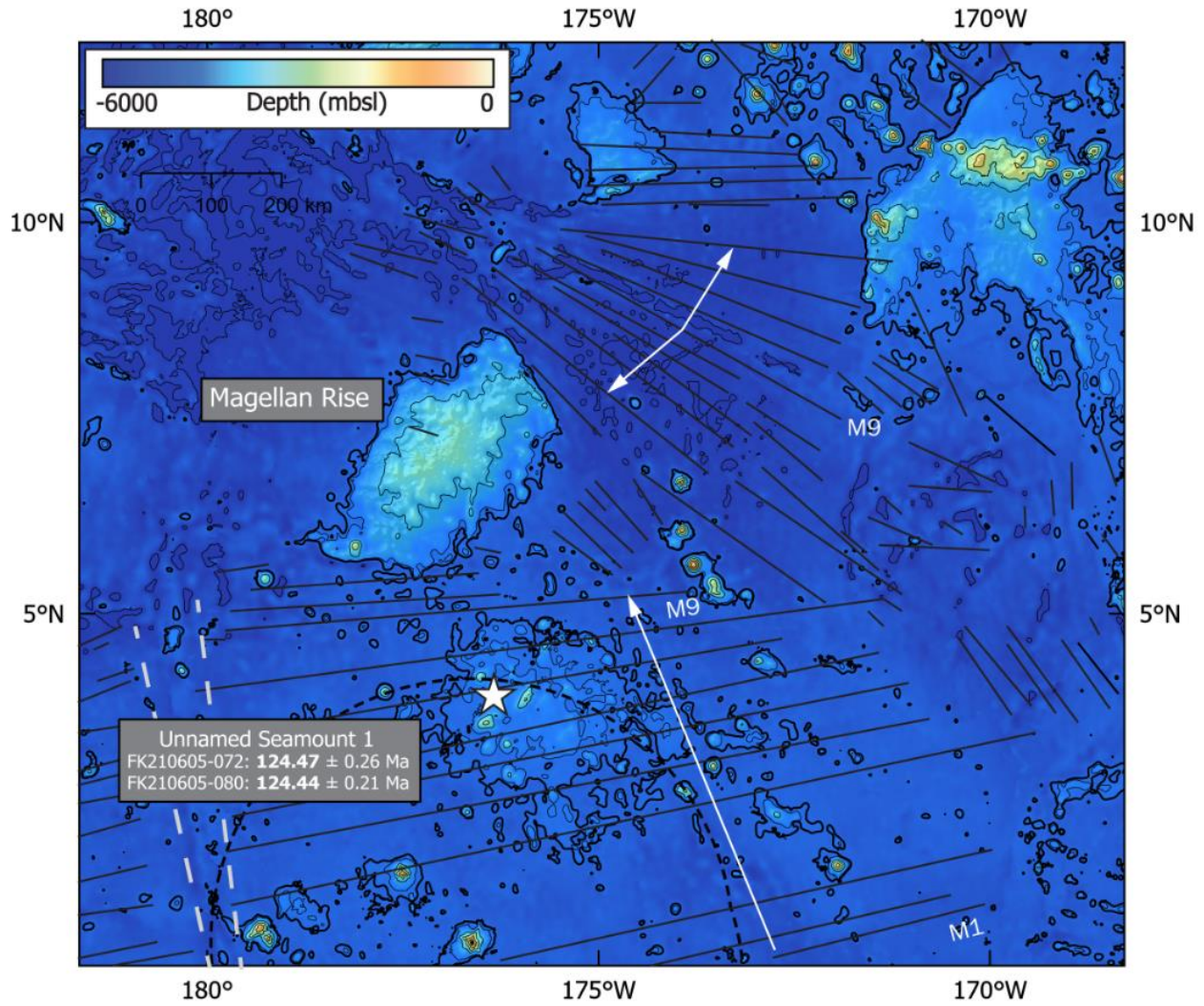


Figure 31: Bathymetric map of Magellan Rise and surrounding area. Contour lines are shown at 1000 m intervals. The bold contour highlights a local swell at 5200 mbsl below Unnamed Seamount 1 (white star). The Magellan microplate ceased spreading at the M9 chron and spreading directions are indicated by the white arrows.

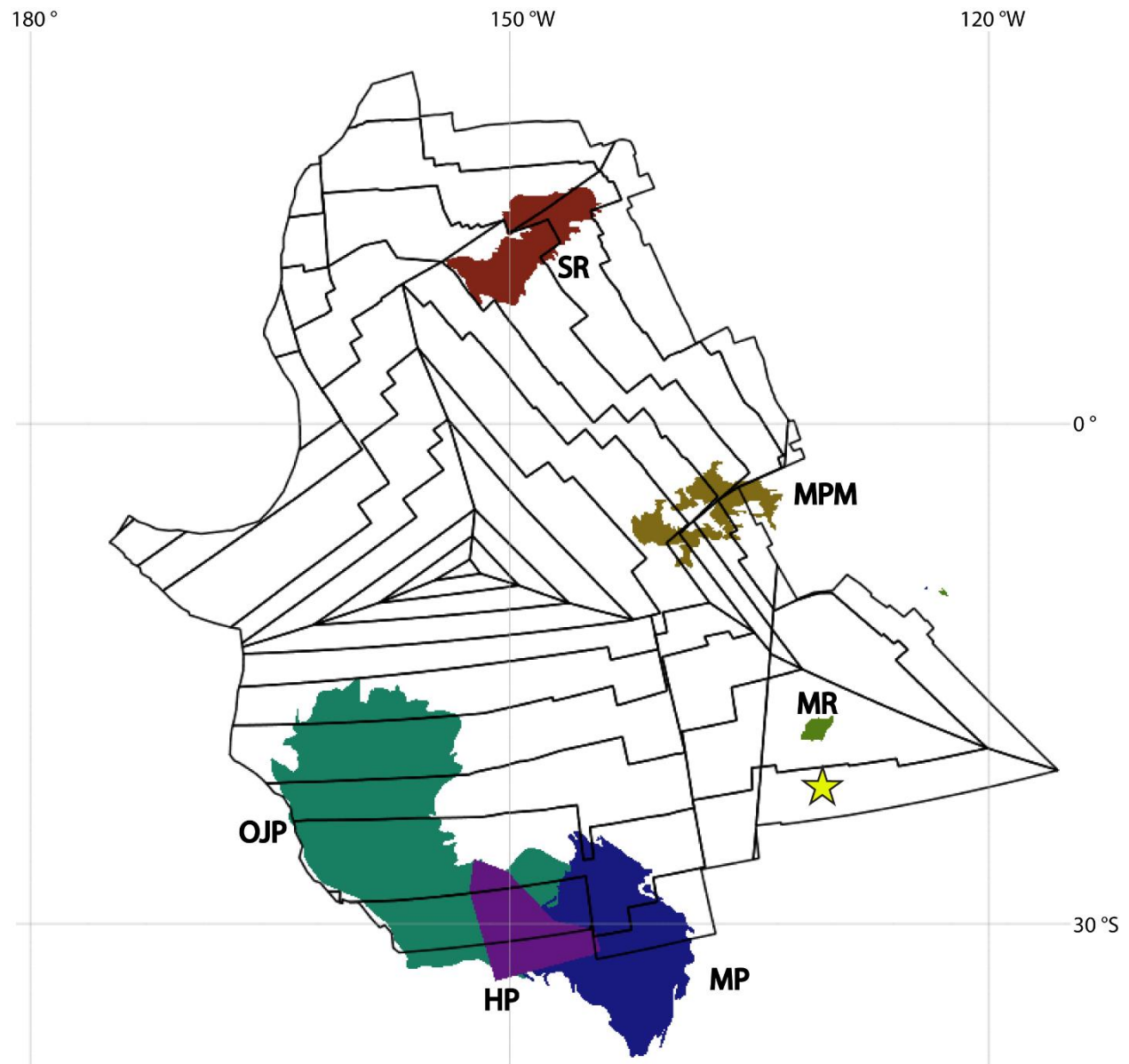


Figure 32: Reconstruction of the Pacific plate with various LIPs *ca.* 124 Ma. Yellow Star = Unnamed Seamount 1. SR = Shatsky Rise, MPM = Mid-Pacific Mountains, MR = Magellan Rise, HP = Hikurangi Plateau, OJP = Ontong Java Plateau. LIP margins from Johansson et al. (2018). Stage pole rotations and isochrons from Müller et al. (2018).

If Unnamed Seamount 1 was not sourced from hotspot volcanism, then perhaps it is related to a contemporaneous tectonomagmatic event. The Ontong Java, Manihiki, and Hikurangi Plateaus are believed to have been emplaced as a single massive LIP called Ontong Java-Nui (OJN; Taylor, 2006; Chandler et al., 2012; Figure 32). The large volumes of melt produced at OJN may make the feature the largest LIP in Earth's history (Sano et al., 2021). The exact age, as well as the time interval during construction of the LIP is still debated, with ages ranging from 126 to 116 Ma (Taylor, 2006; Hoernle et al., 2010; Timm et al., 2011; Davidson et al., 2023b). However, the initiation of the spreading centers that separated the plateau into three distinct LIPs was well under way at 119 Ma and believed to have initiated sometime around 123 Ma (Davidson et al., 2023a). Therefore, the bulk of the massive plateau ($59\text{-}90 \times 10^6 \text{ km}^3$; roughly the size of Alaska; Neal et al., 2019) was likely emplaced prior to 123 Ma and would have affected the regional lithosphere, as well as mantle behavior.

The rapid emplacement of the Ontong Java-Nui plateau would have placed enormous stress on the underlying lithosphere. For example, Bianco et al., (2005) generated numerical models that explained the anomalous 'arch volcanism' located near Hawai'i was produced from decompression via flexural uplift of the lithosphere as a result of the emplacement of the large Hawaiian Islands. If this mechanism is scaled to account for localized subsidence of the lithosphere from the OJN, it would be expected that regional displaced mantle beneath the structure would flex upward at a distance and generate large arch volcanic fields. To date, no research has modeled the potential arch volcanic responses to a LIP emplacement as of yet and as such, this hypothesis remains highly speculative. To test this hypothesis additional geophysical modeling is required, as well as a dedicated campaign on volcanoes residing at similar distances from OJN.

Chapter 7: Summary and Conclusions

New insights into the tectonomagmatic history of the South Pacific basin have been elucidated using new $^{40}\text{Ar}/^{39}\text{Ar}$ age determinations and major and trace element geochemistry of lava flows. The results indicate that at least three unique volcanic events are evident at the HBI EEZ:

1. Erupted tephra found at Unnamed Seamount 1 (124.17 ± 0.12 Ma; 124.22 ± 0.13 Ma) are felsic trachytes with trace element patterns that are indicative of shallow melting. The seamount and underlying bathymetric swell are likely related to flexural stress on the lithosphere during the emplacement of the OJN oceanic plateau or during the annealing of the Magellan microplate to the Pacific. Future bathymetric mapping and geophysical modeling of the area will be needed to provide additional insight into the processes that sourced Unnamed Seamount 1.
2. Lava flows recovered from Unnamed Seamount 2 (85.61 ± 0.14 Ma) and Unnamed Seamount 3 (no age) produced alkalic basalt samples with similar trace element patterns that likely share a similar geodynamic origin. Although key high field strength element ratios for these structures reveal a deep melting source ($\text{Dy}/\text{Yb} = 1.7\text{-}2.0$), the emplacement age does not match any modern hotspot. Provided the lack of evidence for a seamount chain in the region, it remains unclear if the seamounts were formed from lithospheric extension, distal plume channelization, or as an anomalous and extremely short-lived plume derived volcano.
3. The age progression observed in the eastern HBI EEZ, and Tokelau chain to the south, is a Cretaceous analog for hotspot-sourced intraplate volcanism in the Cook-Austral Islands region today. Titov Ridge (71.41 ± 0.23 Ma) and Howland Island (73.57 ± 0.28 Ma) exhibit

trace element ratios consistent with deep melting OIBs and are among the oldest known lava flows sourced from the Macdonald plume.

4. Inter-hotspot distances between coeval seamounts formed from the Macdonald hotspot and other long-lived systems reveal new insights into the relative motions between Pacific mantle plumes. The calculated distance between the Macdonald and Rurutu-Arago hotspots from 75 Ma to modern day is negligible, while the distance between the Macdonald and Louisville hotspots changed by around ~12.5% and Macdonald to Hawaii distance changed by ~9% from 70 Ma to modern day. The results indicate that it is possible both Louisville are moving independently, thus exaggerating the relative inter-hotspot distances that were previously interpreted. These observations call into question the deduction that the Hawaii plume moved significantly in the late Cenozoic. The results also indicate that the assumption of fixed hotspots into deep time is likely accurate to ~10% and as such they can be used to develop absolute plate motion models.

Appendices

Appendix A: $^{40}\text{Ar}/^{39}\text{Ar}$ results from incremental heating experiments.

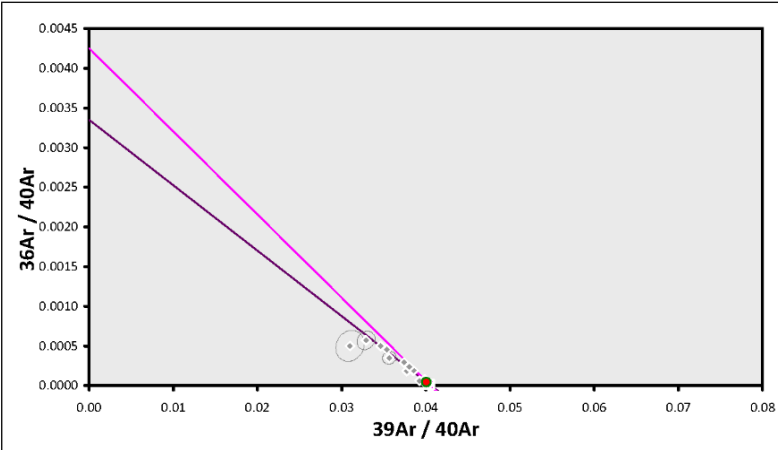
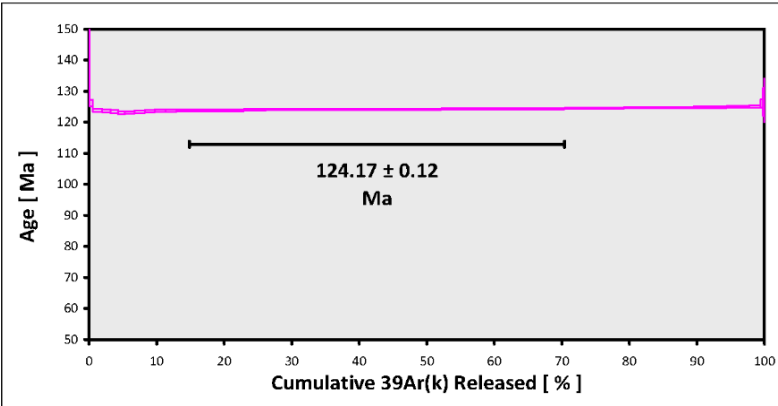
EXP#FK210605-072 > FK210605-072 >
HOWLAND AND BAKER ISLAND > HOWLAND AND BAKER ISLAND
UNLV-131-2 > Sample > Plagioclase > Kevin Konrad

Information on Analysis
and Constants Used in Calculations

Project =
Sample = FK210605-072
Material = Plagioclase
Location = Howland and Baker Island
Region = Howland and Baker Island
Analyst = Kevin Konrad
Irradiation = UNLV-131-2
Position = X: 0 | Y: 0 | Z/H: 35 mm
FCT-NM Age = 28.201 ± 0.023 Ma
FCT-NM Reference = Kuiper et al. (2008)
FCT-NM 40Ar/39Ar Ratio =
FCT-NM J-value = 0.00285038 ± 0.00000114
Air Shot 40Ar/36Ar = 307.0640 ± 0.8506
Air Shot MDF = 0.99306741 ± 0.00072014 (LIN)
Experiment Type = Sample
Extraction Method = Furnace Heating
Heating = 840 sec
Isolation = 20.00 min
Instrument = NGX
Preferred Age = Plateau Age
Age Classification = Crystallization Age
IGSN = Undefined
Rock Class = Igneous>Volcanic>Mafic
Lithology = Trachyte
Lat-Lon = Undefined - Undefined
Age Equations = Min et al. (2000)
Negative Intensities = Allowed
Collector Calibrations = 36Ar
Decay 40K(total) = 5.463 ± 0.107 E-10 1/a
Decay Activity 40K([EC,β⁺]) = 3.310 ± 0.060 1/gs
Decay Activity 40K([β⁻]) = 27.890 ± 0.300 1/gs
Decay 39Ar = 2.940 ± 0.016 E-07 1/h
Decay 37Ar = 8.230 ± 0.012 E-04 1/h
Decay 36Cl = 2.257 ± 0.015 E-06 1/a
Production 39/37(ca) = 0.0006890 ± 0.0000562
Production 38/37(ca) = 0.0000362 ± 0.0000113
Production 36/37(ca) = 0.0002941 ± 0.0000086
Production 38/39(k) = 0.012320 ± 0.000060
Production 36/38(cl) = 262.80 ± 1.71
Scaling Ratio K/Ca = 0.430
Abundance Ratio 40K/K = 1.1700 ± 0.0100 E-04
Atomic Weight K = 39.0983 ± 0.0001 g
Trapped 40/36(a) = 298.56 ± 0.31
Trapped 38/36(a) = 0.1885 ± 0.0003
Standard MDF 40/36(a) = 298.56 ± 0.31
Standard MDF Reference = Lee et al 2006

Sample produced a concordant age plateau that
incorporated 56% of 39Ar released.

Results	40(a)/36(a) ± 2σ	40(r)/39(k) ± 2σ	Age ± 2σ (Ma)	MSWD	39Ar(k) (%,n)	K/Ca ± 2σ
Age Plateau		24.62503 ± 0.01609 ± 0.07%	124.17 ± 0.12 ± 0.10% Full External Error ± 5.06 Analytical Error ± 0.08	1.70 5% 1.78 1.3040	55.60 14 2σ Confidence Limit Error Magnification	53.9 ± 5.0
Total Fusion Age		24.64795 ± 0.00960 ± 0.04%	124.29 ± 0.11 ± 0.09% Full External Error ± 5.06 Analytical Error ± 0.05		36 50.5 ± 3.4	
Normal Isochron Error Chron	119.48 ± 134.87 #####	24.68619 ± 0.04909 ± 0.20%	124.47 ± 0.26 ± 0.21% Full External Error ± 5.08 Analytical Error ± 0.24	2.06 2% 1.82 1.4343	55.60 14 2σ Confidence Limit Error Magnification	
Inverse Isochron Clustered Points	235.22 ± 102.12 ± 43.41%	24.64585 ± 0.04693 ± 0.19%	124.28 ± 0.25 ± 0.20% Full External Error ± 5.07 Analytical Error ± 0.23	1.75 5% 1.82 1.3233	55.60 14 2σ Confidence Limit Error Magnification Spreading Factor	



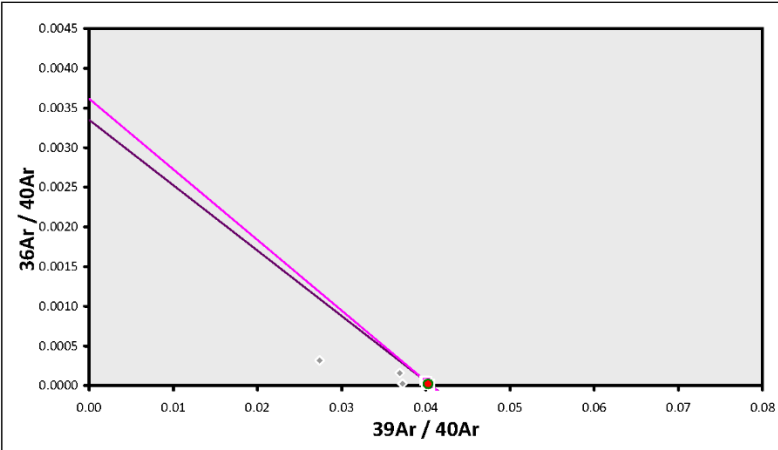
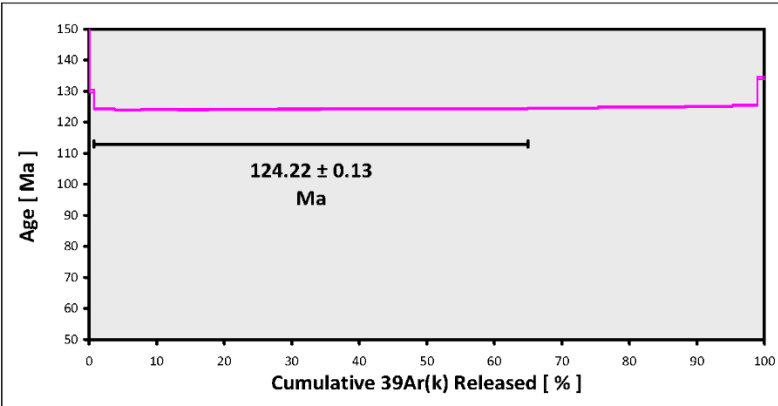
EXP#FK210605-080 > FK210605-080 >
HOWLAND AND BAKER ISLAND > HOWLAND AND BAKER ISLAND
UNLV-131-2 > Sample > Plagioclase > Kevin Konrad

Information on Analysis
and Constants Used in Calculations

Project =
Sample = FK210605-080
Material = Plagioclase
Location = Howland and Baker Island
Region = Howland and Baker Island
Analyst = Kevin Konrad
Irradiation = UNLV-131-2
Position = X: 0 | Y: 0 | Z/H: 40 mm
FCT-NM Age = 28.201 ± 0.023 Ma
FCT-NM Reference = Kuiper et al. (2008)
FCT-NM 40Ar/39Ar Ratio =
FCT-NM J-value = 0.00285397 ± 0.00000114
Air Shot 40Ar/36Ar = 306.9710 ± 1.0161
Air Shot MDF = 0.99314115 ± 0.00084471 (LIN)
Experiment Type = Sample
Extraction Method = Furnace Heating
Heating = 840 sec
Isolation = 20.00 min
Instrument = NGX
Preferred Age = Plateau Age
Age Classification = Crystallization Age
IGSN = Undefined
Rock Class = Igneous>Volcanic>Mafic
Lithology = Trachyte
Lat-Lon = Undefined - Undefined
Age Equations = Min et al. (2000)
Negative Intensities = Allowed
Collector Calibrations = 36Ar
Decay 40K(total) = 5.463 ± 0.107 E-10 1/a
Decay Activity 40K(EC,β⁺) = 3.310 ± 0.060 1/gs
Decay Activity 40K(β⁻) = 27.890 ± 0.300 1/gs
Decay 39Ar = 2.940 ± 0.016 E-07 1/h
Decay 37Ar = 8.230 ± 0.012 E-04 1/h
Decay 36Cl = 2.257 ± 0.015 E-06 1/a
Production 39/37(ca) = 0.0006890 ± 0.0000562
Production 38/37(ca) = 0.0000362 ± 0.0000113
Production 36/37(ca) = 0.0002941 ± 0.0000086
Production 38/39(k) = 0.012320 ± 0.000060
Production 36/38(cl) = 262.80 ± 1.71
Scaling Ratio K/Ca = 0.430
Abundance Ratio 40K/K = 1.1700 ± 0.0100 E-04
Atomic Weight K = 39.0983 ± 0.0001 g
Trapped 40/36(a) = 298.56 ± 0.31
Trapped 38/36(a) = 0.1885 ± 0.0003
Standard MDF 40/36(a) = 298.56 ± 0.31
Standard MDF Reference = Lee et al 2006

Sample produced a concordant age plateau that
incorporated 64% of 39Ar released.

Results	40(a)/36(a) ± 2σ	40(r)/39(k) ± 2σ	Age ± 2σ (Ma)	MSWD	39Ar(k) (%,n)	K/Ca ± 2σ
Age Plateau		24.60335 ± 0.01675 ± 0.07%	124.22 ± 0.13 ± 0.10% Full External Error ± 5.06 Analytical Error ± 0.08	1.63 9% 1.2777	64.26 11 2σ Confidence Limit Error Magnification	58.7 ± 5.8
Total Fusion Age		24.69202 ± 0.01173 ± 0.05%	124.65 ± 0.11 ± 0.09% Full External Error ± 5.08 Analytical Error ± 0.06		18 58.5 ± 2.7	
Normal Isochron Error Chron	236.18 ± 54.28 ± 22.98%	24.64918 ± 0.03759 ± 0.15%	124.44 ± 0.21 ± 0.17% Full External Error ± 5.07 Analytical Error ± 0.18	2.50 1% 1.5809	64.26 11 2σ Confidence Limit Error Magnification	
Inverse Isochron Clustered Points	276.59 ± 42.78 ± 15.47%	24.61613 ± 0.03044 ± 0.12%	124.28 ± 0.18 ± 0.14% Full External Error ± 5.06 Analytical Error ± 0.15	1.63 10% 1.2776	64.26 11 2σ Confidence Limit Error Magnification Spreading Factor	



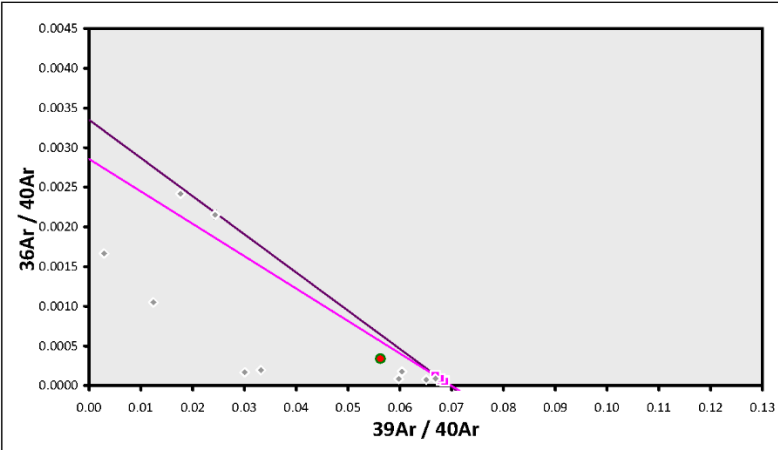
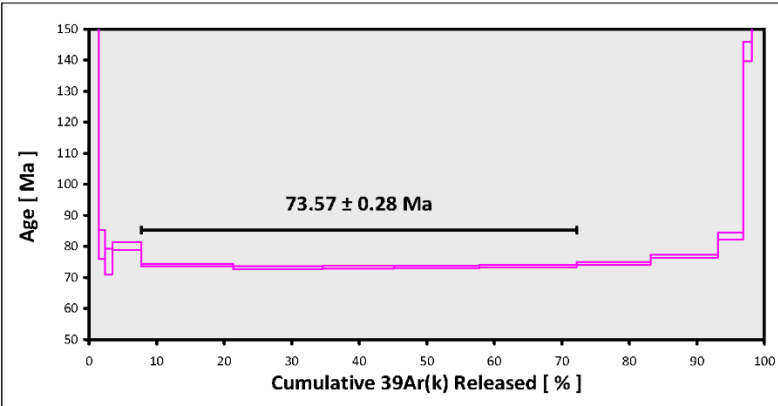
EXP#FK210605-138 > FK210605-138 >
HOWLAND AND BAKER ISLAND > HOWLAND AND BAKER ISLAND
UNLV-131-2 > Sample > Plagioclase > Kevin Konrad

Information on Analysis
and Constants Used in Calculations

Project =
Sample = FK210605-138
Material = Plagioclase
Location = Howland and Baker Island
Region = Howland and Baker Island
Analyst = Kevin Konrad
Irradiation = UNLV-131-2
Position = X: 0 | Y: 0 | Z/H: 41 mm
FCT-NM Age = 28.201 ± 0.023 Ma
FCT-NM Reference = Kuiper et al. (2008)
FCT-NM 40Ar/39Ar Ratio =
FCT-NM J-value = 0.00285420 ± 0.00000114
Air Shot 40Ar/36Ar = 307.0020 ± 0.9701
Air Shot MDF = 0.99311657 ± 0.00080986 (LIN)
Experiment Type = Sample
Extraction Method = Furnace Heating
Heating = 840 sec
Isolation = 20.00 min
Instrument = NGX
Preferred Age = Plateau Age
Age Classification = Crystallization Age
IGSN = Undefined
Rock Class = Igneous>Volcanic>Mafic
Lithology = Phonolitic-Tephrite
Lat-Lon = Undefined - Undefined
Age Equations = Min et al. (2000)
Negative Intensities = Allowed
Collector Calibrations = 36Ar
Decay 40K(total) = 5.463 ± 0.107 E-10 1/a
Decay Activity 40K(EC,β⁺) = 3.310 ± 0.060 1/gs
Decay Activity 40K(β⁻) = 27.890 ± 0.300 1/gs
Decay 39Ar = 2.940 ± 0.016 E-07 1/h
Decay 37Ar = 8.230 ± 0.012 E-04 1/h
Decay 36Cl = 2.257 ± 0.015 E-06 1/a
Production 39/37(ca) = 0.0006890 ± 0.0000562
Production 38/37(ca) = 0.0000362 ± 0.0000113
Production 36/37(ca) = 0.0002941 ± 0.0000086
Production 38/39(k) = 0.012320 ± 0.000060
Production 36/38(cl) = 262.80 ± 1.71
Scaling Ratio K/Ca = 0.430
Abundance Ratio 40K/K = 1.1700 ± 0.0100 E-04
Atomic Weight K = 39.0983 ± 0.0001 g
Trapped 40/36(a) = 298.56 ± 0.31
Trapped 38/36(a) = 0.1885 ± 0.0003
Standard MDF 40/36(a) = 298.56 ± 0.31
Standard MDF Reference = Lee et al 2006

Sample produced a concordant age plateau that incorporated 64.5% of 39Ar released. Sample was slightly discordant but still falls within the 95% certainty of a single population (PoF=7%).

Results	40(a)/36(a) ± 2σ	40(r)/39(k) ± 2σ	Age ± 2σ (Ma)	MSWD	39Ar(k) (%),n	K/Ca ± 2σ
Age Plateau		14.36786 ± 0.05509 ± 0.38%	73.57 ± 0.28 ± 0.38% Full External Error ± 3.04 Analytical Error ± 0.28	2.15 7% 5	64.49 5	0.095 ± 0.001
Total Fusion Age		15.98524 ± 0.03879 ± 0.24%	81.67 ± 0.20 ± 0.25% Full External Error ± 3.36 Analytical Error ± 0.19		15	0.095 ± 0.000
Normal Isochron	321.82 ± 138.58 ± 43.06%	14.33274 ± 0.18123 ± 1.26%	73.39 ± 0.91 ± 1.24% Full External Error ± 3.16 Analytical Error ± 0.91	2.27 8% 5	64.49 5	2.63 2σ Confidence Limit 1.5063 Error Magnification
Inverse Isochron Clustered Points	350.18 ± 150.39 ± 42.95%	14.30398 ± 0.19544 ± 1.37%	73.25 ± 0.98 ± 1.34% Full External Error ± 3.17 Analytical Error ± 0.98	2.45 6% 5	64.49 5	2.63 2σ Confidence Limit 1.5650 Error Magnification 3% Spreading Factor



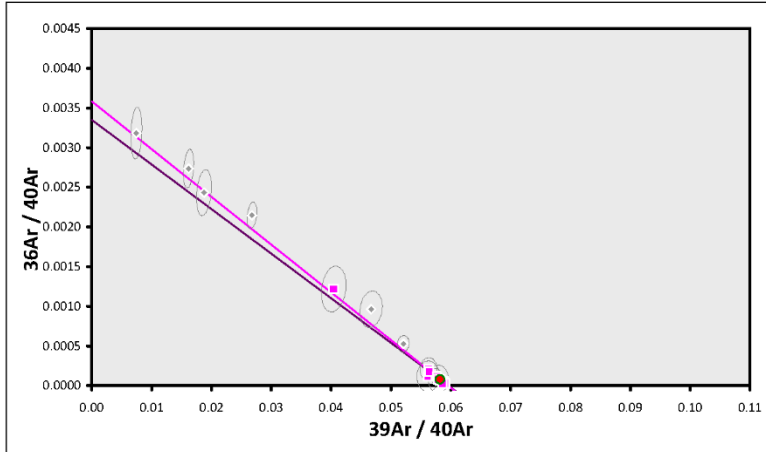
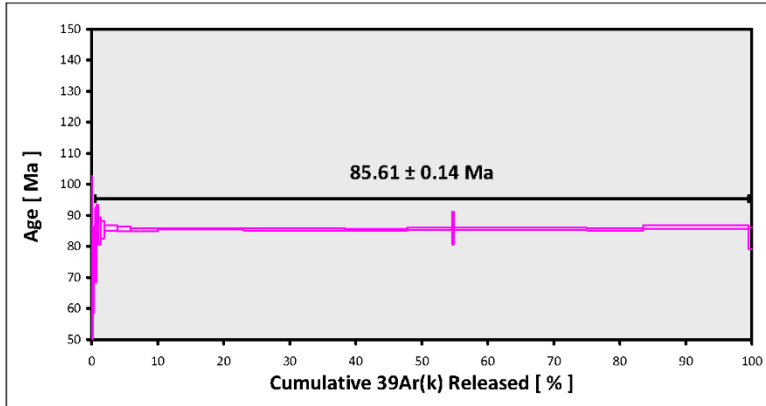
EXP#FK210605-307_HBL > FK210605-307_HBL >
HOWLAND AND BAKER ISLAND > HOWLAND AND BAKER ISLAND
UNLV-131-2 > Sample > Amphibole > Kathy Zanetti

Information on Analysis
and Constants Used in Calculations

Project =
Sample = FK210605-307_HBL
Material = Amphibole
Location = Howland and Baker Island
Region = Howland and Baker Island
Analyst = Kathy Zanetti
Irradiation = UNLV-131-2
Position = X: 0 | Y: 0 | Z/H: 47 mm
FCT-NM Age = 28.201 ± 0.023 Ma
FCT-NM Reference = Kuiper et al. (2008)
FCT-NM 40Ar/39Ar Ratio =
FCT-NM J-value = 0.00285217 ± 0.00000143
Air Shot 40Ar/36Ar = 306.4780 ± 0.8949
Air Shot MDF = 0.99353279 ± 0.00075587 (UN)
Experiment Type = Sample
Extraction Method = Furnace Heating
Heating = 840 sec
Isolation = 20.00 min
Instrument = NGX
Preferred Age = Plateau Age
Age Classification = Crystallization Age
IGSN = Undefined
Rock Class = Igneous>Volcanic>Mafic
Lithology = Trachybasalt
Lat-Lon = Undefined - Undefined
Age Equations = Min et al. (2000)
Negative Intensities = Allowed
Collector Calibrations = 36Ar
Decay 40K(total) = 5.463 ± 0.107 E-10 1/a
Decay Activity 40K(EC,β⁺) = 3.310 ± 0.060 1/g
Decay Activity 40K(β⁻) = 27.890 ± 0.300 1/g
Decay 39Ar = 2.940 ± 0.016 E-07 1/h
Decay 37Ar = 8.230 ± 0.012 E-04 1/h
Decay 36Cl = 2.257 ± 0.015 E-06 1/a
Production 39/37(ca) = 0.0006890 ± 0.0000562
Production 38/37(ca) = 0.0000362 ± 0.0000113
Production 36/37(ca) = 0.0002941 ± 0.0000086
Production 38/39(k) = 0.012320 ± 0.000060
Production 36/38(cl) = 262.80 ± 1.71
Scaling Ratio K/Ca = 0.430
Abundance Ratio 40K/K = 1.1700 ± 0.0100 E-04
Atomic Weight K = 39.0983 ± 0.0001 g
Trapped 40/36(a) = 298.56 ± 0.31
Trapped 38/36(a) = 0.1885 ± 0.0003
Standard MDF 40/36(a) = 298.56 ± 0.31
Standard MDF Reference = Lee et al 2006

Sample produced a concordant age plateau that incorporated 73% of 39Ar released. Possible CPX inclusions from low K/Ca ratios at higher temperatures.

Results	40(a)/36(a) ± 2σ	40(r)/39(k) ± 2σ	Age ± 2σ (Ma)	MSWD	39Ar(k) (%n)	K/Ca ± 2σ
Age Plateau		16.78672 ± 0.02363 ± 0.14%	85.61 ± 0.14 ± 0.17% Full External Error ± 3.52 Analytical Error ± 0.12	0.75 73% 1.0000	98.97 15 2σ Confidence Limit Error Magnification	0.0641 ± 0.0086
Total Fusion Age		16.78403 ± 0.02947 ± 0.18%	85.59 ± 0.17 ± 0.20% Full External Error ± 3.52 Analytical Error ± 0.15		21	0.0564 ± 0.0002
Normal Isochron	256.51 ± 37.06 ± 14.45%	16.82391 ± 0.03803 ± 0.23%	85.79 ± 0.21 ± 0.24% Full External Error ± 3.53 Analytical Error ± 0.19	0.59 87% 1.0000	98.97 15 2σ Confidence Limit Error Magnification	
Inverse Isochron	279.15 ± 38.13 ± 13.66%	16.80319 ± 0.03913 ± 0.23%	85.69 ± 0.21 ± 0.25% Full External Error ± 3.52 Analytical Error ± 0.19	0.74 73% 1.0000	98.97 15 2σ Confidence Limit Error Magnification Spreading Factor	



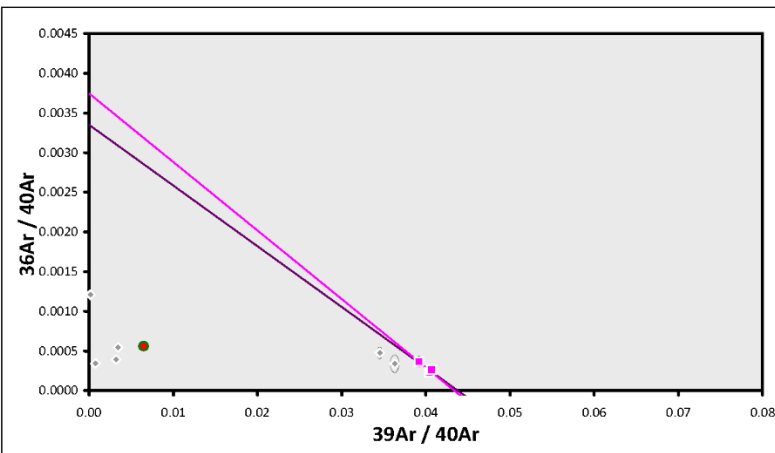
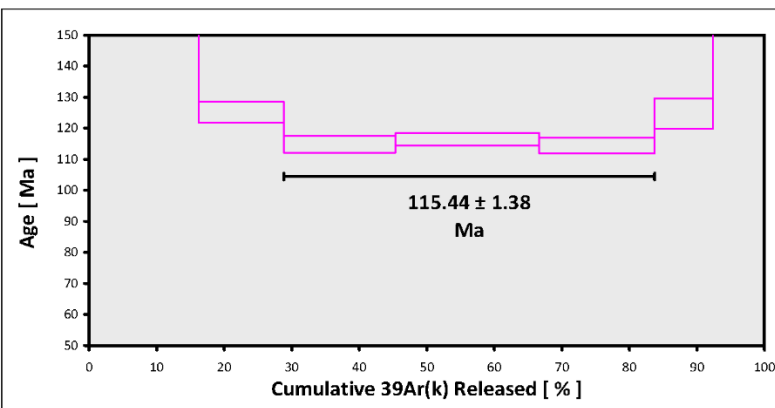
**EXP#FK210605-338 > FK210605-338 >
HOWLAND AND BAKER ISLAND > HOWLAND AND BAKER ISLAND
UNLV-131-2 > Sample > Plagioclase > Kevin Konrad**

**Information on Analysis
and Constants Used in Calculations**

Project =
Sample = **FK210605-338**
Material = **Plagioclase**
Location = **Howland and Baker Island**
Region = **Howland and Baker Island**
Analyst = **Kevin Konrad**
Irradiation = **UNLV-131-2**
Position = **X: 0 | Y: 0 | Z/H: 50 mm**
FCT-NM Age = **28.201 ± 0.023 Ma**
FCT-NM Reference = **Kuiper et al. (2008)**
FCT-NM 40Ar/39Ar Ratio =
FCT-NM J-value = **0.00284896 ± 0.00000142**
Air Shot 40Ar/36Ar = **307.7160 ± 0.8647**
Air Shot MDF = **0.99255171 ± 0.00072772 (LIN)**
Experiment Type = **Sample**
Extraction Method = **Furnace Heating**
Heating = **840 sec**
Isolation = **20.00 min**
Instrument = **NGX**
Preferred Age = **Plateau Age**
Age Classification = **Crystallization Age**
IGSN = **Undefined**
Rock Class = **Igneous>Volcanic>Mafic**
Lithology = **Basanite**
Lat-Lon = **Undefined - Undefined**
Age Equations = **Min et al. (2000)**
Negative Intensities = **Allowed**
Collector Calibrations = **36Ar**
Decay 40K(total) = **5.463 ± 0.107 E-10 1/a**
Decay Activity 40K(EC,β⁺) = **3.310 ± 0.060 1/gs**
Decay Activity 40K(β⁻) = **27.890 ± 0.300 1/gs**
Decay 39Ar = **2.940 ± 0.016 E-07 1/h**
Decay 37Ar = **8.230 ± 0.012 E-04 1/h**
Decay 36Cl = **2.257 ± 0.015 E-06 1/a**
Production 39/37(ca) = **0.0006890 ± 0.0000562**
Production 38/37(ca) = **0.0000362 ± 0.0000113**
Production 36/37(ca) = **0.0002941 ± 0.0000086**
Production 38/39(k) = **0.012320 ± 0.000060**
Production 36/38(cl) = **262.80 ± 1.71**
Scaling Ratio K/Ca = **0.430**
Abundance Ratio 40K/K = **1.1700 ± 0.0100 E-04**
Atomic Weight K = **39.0983 ± 0.0001 g**
Trapped 40/36(a) = **298.56 ± 0.31**
Trapped 38/36(a) = **0.1885 ± 0.0003**
Standard MDF 40/36(a) = **298.56 ± 0.31**
Standard MDF Reference = **Lee et al 2006**

The (trace) amount of plagioclase phenocrysts produced a small (3-step) concordant plateau that accounts for 55% of the 39Ar released. The three steps used fall along the atmospheric reference line. The higher temperature steps have some excess 40Ar with very low [39Ar]

Results	40(a)/36(a) ± 2σ	40(r)/39(k) ± 2σ	Age ± 2σ (Ma)	MSWD	39Ar(k) (%),n	K/Ca ± 2σ
Age Plateau		22.84863 ± 0.28002 ± 1.23%	115.44 ± 1.38 ± 1.19% Full External Error ± 4.91 Analytical Error ± 1.37	0.88 41% 3.00 1.0000	54.92 3 2σ Confidence Limit Error Magnification	0.104 ± 0.003
Total Fusion Age		128.72190 ± 0.49339 ± 0.38%	571.87 ± 1.95 ± 0.34% Full External Error ± 21.41 Analytical Error ± 1.88		9 0.091 ± 0.001	
Normal Isochron No Convergence	250.23 ± 224.61 ± 89.76%	23.14538 ± 1.58328 ± 6.84%	116.89 ± 7.75 ± 6.63% Full External Error ± 9.10 Analytical Error ± 7.75	1.78 18% 3.83 1.3344	54.92 3 2σ Confidence Limit Error Magnification	
Inverse Isochron Clustered Points	267.07 ± 236.49 ± 88.55%	23.06449 ± 1.53427 ± 6.65%	116.49 ± 7.51 ± 6.45% Full External Error ± 8.89 Analytical Error ± 7.51	1.67 20% 3.83 1.2915	54.92 3 2σ Confidence Limit Error Magnification Spreading Factor	



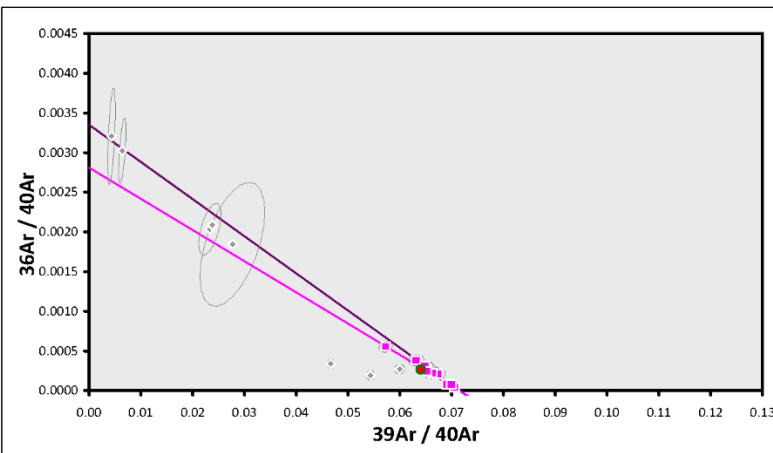
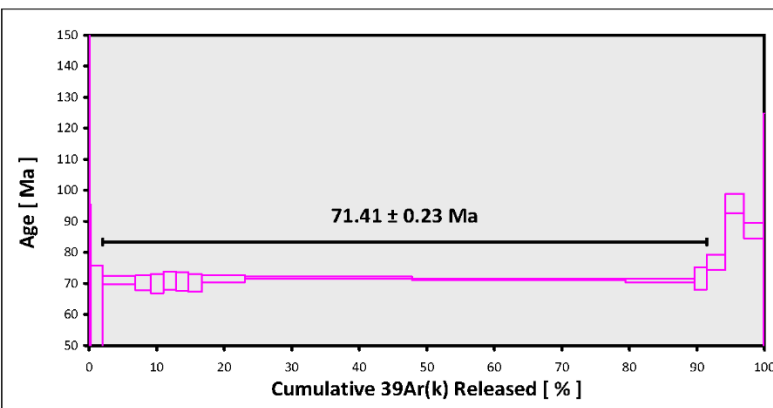
**EXP#FK210605-397 > FK210605-397 >
HOWLAND AND BAKER ISLAND > HOWLAND AND BAKER ISLAND
UNLV-131-2 > Sample > Amphibole > Kathy Zanetti**

**Information on Analysis
and Constants Used in Calculations**

Project =
Sample = FK210605-397
Material = Amphibole
Location = Howland and Baker Island
Region = Howland and Baker Island
Analyst = Kathy Zanetti
Irradiation = UNLV-131-2
Position = X: 0 | Y: 0 | Z/H: 53 mm
FCT-NM Age = 28.201 ± 0.023 Ma
FCT-NM Reference = Kuiper et al. (2008)
FCT-NM 40Ar/39Ar Ratio =
FCT-NM J-value = 0.00284420 ± 0.00000228
Air Shot 40Ar/36Ar = 306.8230 ± 0.8929
Air Shot MDF = 0.99325859 ± 0.00075273 (LIN)
Experiment Type = Sample
Extraction Method = Furnace Heating
Heating = 840 sec
Isolation = 20.00 min
Instrument = NGX
Preferred Age = Inverse Isochron
Age Classification = Crystallization Age
IGSN = Undefined
Rock Class = Igneous>Volcanic>Intermediate
Lithology = Trachyandesite
Lat-Lon = Undefined - Undefined
Age Equations = Min et al. (2000)
Negative Intensities = Allowed
Collector Calibrations = 36Ar
Decay 40K(total) = 5.463 ± 0.107 E-10 1/a
Decay Activity 40K(EC,β⁺) = 3.310 ± 0.060 1/gs
Decay Activity 40K(β⁻) = 27.890 ± 0.300 1/gs
Decay 39Ar = 2.940 ± 0.016 E-07 1/h
Decay 37Ar = 8.230 ± 0.012 E-04 1/h
Decay 36Cl = 2.257 ± 0.015 E-06 1/a
Production 39/37(ca) = 0.0006890 ± 0.00000562
Production 38/37(ca) = 0.0000362 ± 0.00000113
Production 36/37(ca) = 0.0002941 ± 0.0000086
Production 38/39(k) = 0.012320 ± 0.000060
Production 36/38(cl) = 262.80 ± 1.71
Scaling Ratio K/Ca = 0.430
Abundance Ratio 40K/K = 1.1700 ± 0.0100 E-04
Atomic Weight K = 39.0983 ± 0.0001 g
Trapped 40/36(a) = 356.01 ± 22.74
Trapped 38/36(a) = 0.1885 ± 0.0003
Standard MDF 40/36(a) = 298.56 ± 0.31
Standard MDF Reference = Lee et al 2006

Excess 40/36 = 356.01 ± 6.39 (%SD). Sample produced a concordant isochron that incorporated 89% of 39Ar released. It contained a 40Ar/36Ar intercept of 356 indicating excess argon. Plateau shown is recalculated using new intercept value. Possible CPX inclusions from low K/Ca ratios at higher temperatures.

Results	40(a)/36(a) ± 2σ	40(r)/39(k) ± 2σ	Age ± 2σ (Ma)	MSWD	39Ar(k) (%n)	K/Ca ± 2σ
Age Plateau		13.98696 ± 0.03964 ± 0.28%	71.41 ± 0.23 ± 0.32% Full External Error ± 2.95 Analytical Error ± 0.20	1.06 39% 1.0277	89.43 11 2σ Confidence Limit Error Magnification	0.135 ± 0.024
Total Fusion Age		14.14388 ± 0.09168 ± 0.65%	72.19 ± 0.47 ± 0.65% Full External Error ± 3.01 Analytical Error ± 0.46		19 0.062 ± 0.000	
Normal Isochron	348.57 ± 44.34 ± 12.72%	13.99726 ± 0.06277 ± 0.45%	71.46 ± 0.33 ± 0.47% Full External Error ± 2.96 Analytical Error ± 0.31	1.83 6% 1.3534	89.43 11 2σ Confidence Limit Error Magnification	
Inverse Isochron	356.01 ± 45.48 ± 12.78%	13.99902 ± 0.06469 ± 0.46%	71.47 ± 0.34 ± 0.48% Full External Error ± 2.96 Analytical Error ± 0.32	1.82 6% 1.3493	89.43 11 2σ Confidence Limit Error Magnification Spreading Factor	



References

- Anderson, D.L., 2000, The thermal state of the upper mantle; No role for mantle plumes: *Geophysical Research Letters*, v. 27, p. 3623–3626, doi:10.1029/2000GL011533.
- Anderson, D.L., and Natland, J.H., 2014, Mantle updrafts and mechanisms of oceanic volcanism: *Proceedings of the National Academy of Sciences*, v. 111, doi:10.1073/pnas.1410229111.
- Balbas, A., Jung, C., and Konrad, K., 2023, The origin of the Musicians Seamount Province and its inferences for Late Cretaceous Pacific Plate Motion: *Marine Geology*, v. 465, p. 107166, doi:10.1016/j.margeo.2023.107166.
- Bas, M.L., Maitre, R.L., Streckeisen, A., Zanettin, B., and IUGS Subcommittee on the Systematics of Igneous Rocks, 1986, A Chemical Classification of Volcanic Rocks Based on the Total Alkali-Silica Diagram: *Journal of Petrology*, v. 27, p. 745–750, doi:10.1093/petrology/27.3.745.
- Benyshek, E.K., Wessel, P., and Taylor, B., 2019, Tectonic Reconstruction of the Ellice Basin: *Tectonics*, v. 38, p. 3854–3865, doi:10.1029/2019TC005650.
- Bercovici, D., and Karato, S., 2003, Whole-mantle convection and the transition-zone water filter: *Nature*, v. 425, p. 39–44, doi:10.1038/nature01918.
- Bianco, T.A., Ito, G., Becker, J.M., and Garcia, M.O., 2005, Secondary Hawaiian volcanism formed by flexural arch decompression: *Geochemistry, Geophysics, Geosystems*, v. 6, p. 2005GC000945, doi:10.1029/2005GC000945.
- Bonneville, A., Dosso, L., and Hildenbrand, A., 2006, Temporal evolution and geochemical variability of the South Pacific superplume activity: *Earth and Planetary Science Letters*, v. 244, p. 251–269, doi:10.1016/j.epsl.2005.12.037.

- Bonneville, A., Suavé, R.L., Audin, L., Clouard, V., Dosso, L., Gillot, P.Y., Janney, P., Jordahl, K., and Maamaatuaiahutapu, K., 2002, Arago Seamount: The missing hotspot found in the Austral Islands: *Geology*, v. 30, p. 1023, doi:10.1130/0091-7613(2002)030<1023:ASTMHF>2.0.CO;2.
- Bono, R.K., Tarduno, J.A., and Bunge, H.-P., 2019, Hotspot motion caused the Hawaiian-Emperor Bend and LLSVPs are not fixed: *Nature Communications*, v. 10, p. 3370, doi:10.1038/s41467-019-11314-6.
- Boschman, L.M., and Van Hinsbergen, D.J.J., 2016, On the enigmatic birth of the Pacific Plate within the Panthalassa Ocean: *Science Advances*, v. 2, p. e1600022, doi:10.1126/sciadv.1600022.
- Brown, S.M., Elkins-Tanton, L.T., and Walker, R.J., 2014, Effects of magma ocean crystallization and overturn on the development of ^{142}Nd and ^{182}W isotopic heterogeneities in the primordial mantle: *Earth and Planetary Science Letters*, v. 408, p. 319–330, doi:10.1016/j.epsl.2014.10.025.
- Buff, L., Jackson, M.G., Konrad, K., Konter, J.G., Bizimis, M., Price, A., Rose-Koga, E.F., Blusztajn, J., Koppers, A.A.P., and Herrera, S., 2021, “Missing links” for the long-lived Macdonald and Arago hotspots, South Pacific Ocean: *Geology*, v. 49, p. 541–544, doi:10.1130/G48276.1.
- Burke, K., 2011, Plate Tectonics, the Wilson Cycle, and Mantle Plumes: *Geodynamics from the Top: Annual Review of Earth and Planetary Sciences*, v. 39, p. 1–29, doi:10.1146/annurev-earth-040809-152521.

- Burke, K., Steinberger, B., Torsvik, T.H., and Smethurst, M.A., 2008, Plume Generation Zones at the margins of Large Low Shear Velocity Provinces on the core–mantle boundary: *Earth and Planetary Science Letters*, v. 265, p. 49–60, doi:10.1016/j.epsl.2007.09.042.
- Chandler, M.T., Wessel, P., Taylor, B., Seton, M., Kim, S.-S., and Hyeong, K., 2012, Reconstructing Ontong Java Nui: Implications for Pacific absolute plate motion, hotspot drift and true polar wander: *Earth and Planetary Science Letters*, v. 331–332, p. 140–151, doi:10.1016/j.epsl.2012.03.017.
- Chauvel, C., Hofmann, A.W., and Vidal, P., 1992, himu-em: The French Polynesian connection: *Earth and Planetary Science Letters*, v. 110, p. 99–119, doi:10.1016/0012-821X(92)90042-T.
- Chauvel, C., McDonough, W., Guille, G., Maury, R., and Duncan, R., 1997, Contrasting old and young volcanism in Rurutu Island, Austral chain: *Chemical Geology*, v. 139, p. 125–143, doi:10.1016/S0009-2541(97)00029-6.
- Clague, D.A., and Dalrymple, B.G., 1987, The Hawaiian-emperor volcanic chain: *S Geol. Surv. Prof. Pap.*, v. 1350, p. 5–54.
- Coffin, M.F., 2002, Kerguelen Hotspot Magma Output since 130 Ma: *Journal of Petrology*, v. 43, p. 1121–1137, doi:10.1093/petrology/43.7.1121.
- Courtillot, V., Davaille, A., Besse, J., and Stock, J., 2003, Three distinct types of hotspots in the Earth's mantle: *Earth and Planetary Science Letters*, v. 205, p. 295–308, doi:10.1016/S0012-821X(02)01048-8.
- Dalrymple, G.B., Jarrard, R.D., and Clague, D.A., 1975, K-Ar ages of some volcanic rocks from the Cook and Austral Islands: *Geological Society of America Bulletin*, v. 86, p. 1463, doi:10.1130/0016-7606(1975)86<1463:KAOSVR>2.0.CO;2.

- Davidson, P.C., Koppers, A.A.P., and Konter, J.G., 2023a, Rapid Formation of the Ellice and Osbourn Basins and Ontong Java Nui Breakup Kinematics: Geochemistry, Geophysics, Geosystems, v. 24, p. e2022GC010592, doi:10.1029/2022GC010592.
- Davidson, P.C., Koppers, A.A.P., Sano, T., and Hanyu, T., 2023b, A younger and protracted emplacement of the Ontong Java Plateau: Science, v. 380, p. 1185–1188, doi:10.1126/science.ade8666.
- Dobrovine, P.V., Steinberger, B., and Torsvik, T.H., 2012, Absolute plate motions in a reference frame defined by moving hot spots in the Pacific, Atlantic, and Indian oceans: Journal of Geophysical Research: Solid Earth, v. 117, p. 2011JB009072, doi:10.1029/2011JB009072.
- Duncan, R.A., and Clague, D.A., 1985, Pacific Plate Motion Recorded by Linear Volcanic Chains, in Nairn, A.E.M., Stehli, F.G., and Uyeda, S. eds., The Ocean Basins and Margins: Volume 7A The Pacific Ocean, Boston, MA, Springer US, p. 89–121, doi:10.1007/978-1-4613-2351-8_3.
- Dziewonski, A.M., and Woodhouse, J.H., 1987, Global Images of the Earth's Interior: Science, v. 236, p. 37–48, doi:10.1126/science.236.4797.37.
- Finlayson, V.A., Konter, J.G., Konrad, K., Koppers, A.A.P., Jackson, M.G., and Rooney, T.O., 2018, Sr–Pb–Nd–Hf isotopes and $^{40}\text{Ar}/^{39}\text{Ar}$ ages reveal a Hawaii–Emperor-style bend in the Rurutu hotspot: Earth and Planetary Science Letters, v. 500, p. 168–179, doi:10.1016/j.epsl.2018.08.020.
- Gastra, K.M., Gordon, R.G., and Woodworth, D.T., 2022, Quantification of Pacific Plate Hotspot Tracks Since 80 Ma: Tectonics, v. 41, p. e2021TC006772, doi:10.1029/2021TC006772.

- Garnero, E.J., McNamara, A.K., and Shim, S.-H., 2016, Continent-sized anomalous zones with low seismic velocity at the base of Earth's mantle: *Nature Geoscience*, v. 9, p. 481–489, doi:10.1038/ngeo2733.
- GEBCO 2023 Grid, 2023, GEBCO Compilation Group.:
- Geldmacher, J., Hauff, F., Dürkefälden, A., Sano, T., Garbe-Schönberg, D., Portnyagin, M., and Hoernle, K., 2023, The effects of submarine alteration and phosphatization on igneous rocks: Implications for Sr-, Nd-, Pb-isotope studies: *Chemical Geology*, v. 631, p. 121509, doi:10.1016/j.chemgeo.2023.121509.
- Hanyu, T., Dosso, L., Ishizuka, O., Tani, K., Hanan, B.B., Adam, C., Nakai, S., Senda, R., Chang, Q., and Tatsumi, Y., 2013, Geochemical diversity in submarine HIMU basalts from Austral Islands, French Polynesia: *Contributions to Mineralogy and Petrology*, v. 166, p. 1285–1304, doi:10.1007/s00410-013-0926-x.
- Hart, S.R., Hauri, E.H., Oschmann, L.A., and Whitehead, J.A., 1992, Mantle Plumes and Entrainment: Isotopic Evidence: *Science*, v. 256, p. 517–520, doi:10.1126/science.256.5056.517.
- Hassan, R., Müller, R.D., Gurnis, M., Williams, S.E., and Flament, N., 2016, A rapid burst in hotspot motion through the interaction of tectonics and deep mantle flow: *Nature*, v. 533, p. 239–242, doi:10.1038/nature17422.
- He, M., Zhang, S., Zhang, L., Yang, F., Zhang, Y., Huang, X., and Wei, G., 2022, Element mobility and oxygen isotope systematics during submarine alteration of basaltic glass: *American Mineralogist*, v. 107, p. 432–442, doi:10.2138/am-2021-7831.
- van der Hilst, R.D., Widiyantoro, S., and Engdahl, E.R., 1997, Evidence for deep mantle circulation from global tomography: *Nature*, v. 386, p. 578–584, doi:10.1038/386578a0.

- Hoernle, K., Hauff, F., Van Den Bogaard, P., Werner, R., Mortimer, N., Geldmacher, J., Garbe-Schönberg, D., and Davy, B., 2010, Age and geochemistry of volcanic rocks from the Hikurangi and Manihiki oceanic Plateaus: *Geochimica et Cosmochimica Acta*, v. 74, p. 7196–7219, doi:10.1016/j.gca.2010.09.030.
- Hoernle, K., Rohde, J., Hauff, F., Garbe-Schönberg, D., Homrighausen, S., Werner, R., and Morgan, J.P., 2015, How and when plume zonation appeared during the 132 Myr evolution of the Tristan Hotspot: *Nature Communications*, v. 6, p. 7799, doi:10.1038/ncomms8799.
- Hofmann, A.W., 2007, 2.03 - Sampling Mantle Heterogeneity through Oceanic Basalts: Isotopes and Trace Elements, *in* Holland, H.D. and Turekian, K.K. eds., *Treatise on Geochemistry*, Oxford, Pergamon, p. 1–44, doi:10.1016/B0-08-043751-6/02123-X.
- Hofmann, A.W., and White, W.M., 1982, Mantle plumes from ancient oceanic crust: *Earth and Planetary Science Letters*, v. 57, p. 421–436, doi:10.1016/0012-821X(82)90161-3.
- Huang, S., Tschauner, O., Yang, S., Humayun, M., Liu, W., Gilbert Corder, S.N., Bechtel, H.A., and Tischler, J., 2020, HIMU geochemical signature originating from the transition zone: *Earth and Planetary Science Letters*, v. 542, p. 116323, doi:10.1016/j.epsl.2020.116323.
- Jackson, M.G., Halldórsson, S.A., Price, A., Kurz, M.D., Konter, J.G., Koppers, A.A.P., and Day, J.M.D., 2020, Contrasting Old and Young Volcanism from Aitutaki, Cook Islands: Implications for the Origins of the Cook–Austral Volcanic Chain: *Journal of Petrology*, v. 61, p. egaa037, doi:10.1093/petrology/egaa037.
- Jackson, M.G., Hart, S.R., Konter, J.G., Koppers, A.A.P., Staudigel, H., Kurz, M.D., Blusztajn, J., and Sinton, J.M., 2010, Samoan hot spot track on a “hot spot highway”: Implications for mantle plumes and a deep Samoan mantle source: *Geochimica et Cosmochimica Acta*, v. 74, p. 1035–1050, doi:10.1016/j.gca.2010.02.012.

- Jiang, Q., and Jourdan, F., 2024, Obtaining accurate ages of basaltic rocks using $^{40}\text{Ar}/^{39}\text{Ar}$ techniques, *in* Shellnutt, J.G., Denyszyn, S.W., and Suga, K. eds., *Methods and Applications of Geochronology*, Elsevier, p. 345–366, doi:10.1016/B978-0-443-18803-9.00003-1.
- Johansson, L., Zahirovic, S., and Müller, R.D., 2018, The Interplay Between the Eruption and Weathering of Large Igneous Provinces and the Deep-Time Carbon Cycle: *Geophysical Research Letters*, v. 45, p. 5380–5389, doi:10.1029/2017GL076691.
- Konrad, K., Koppers, A.A.P., Balbas, A.M., Miggins, D.P., and Heaton, D.E., 2019, Dating Clinopyroxene Phenocrysts in Submarine Basalts Using $^{40}\text{Ar}/^{39}\text{Ar}$ Geochronology: *Geochemistry, Geophysics, Geosystems*, v. 20, p. 1041–1053, doi:10.1029/2018GC007697.
- Konrad, K., Koppers, A.A.P., Steinberger, B., Finlayson, V.A., Konter, J.G., and Jackson, M.G., 2018, On the relative motions of long-lived Pacific mantle plumes: *Nature Communications*, v. 9, p. 854, doi:10.1038/s41467-018-03277-x.
- Konter, J.G., Hanan, B.B., Blichert-Toft, J., Koppers, A.A.P., Plank, T., and Staudigel, H., 2008, One hundred million years of mantle geochemical history suggest the retiring of mantle plumes is premature: *Earth and Planetary Science Letters*, v. 275, p. 285–295, doi:10.1016/j.epsl.2008.08.023.
- Koppers, A.A.P., 2002, ArArCALCFsoftware for $^{40}\text{Ar}/^{39}\text{Ar}$ age calculations\$:
- Koppers, A.A.P. et al., 2012, Limited latitudinal mantle plume motion for the Louisville hotspot: *Nature Geoscience*, v. 5, p. 911–917, doi:10.1038/ngeo1638.
- Koppers, A.A.P., 2011, Mantle plumes persevere: *Nature Geoscience*, v. 4, p. 816–817, doi:10.1038/ngeo1334.

- Koppers, A.A.P., Becker, T.W., Jackson, M.G., Konrad, K., Müller, R.D., Romanowicz, B., Steinberger, B., and Whittaker, J.M., 2021, Mantle plumes and their role in Earth processes: Nature Reviews Earth & Environment, v. 2, p. 382–401, doi:10.1038/s43017-021-00168-6.
- Koppers, A.A.P., Morgan, J.P., Morgan, J.W., and Staudigel, H., 2001, Testing the fixed hotspot hypothesis using $^{40}\text{Ar}/^{39}\text{Ar}$ age progressions along seamount trails: Earth and Planetary Science Letters,.
- Koppers, A.A.P., Staudigel, H., and Duncan, R.A., 2003, High-resolution $^{40}\text{Ar}/^{39}\text{Ar}$ dating of the oldest oceanic basement basalts in the western Pacific basin: Geochemistry, Geophysics, Geosystems, v. 4, p. 2003GC000574, doi:10.1029/2003GC000574.
- Koppers, A.A.P., Staudigel, H., Phipps Morgan, J., and Duncan, R.A., 2007, Nonlinear $^{40}\text{Ar}/^{39}\text{Ar}$ age systematics along the Gilbert Ridge and Tokelau Seamount Trail and the timing of the Hawaii-Emperor Bend: Geochemistry, Geophysics, Geosystems, v. 8, doi:10.1029/2006GC001489.
- Kuiper, K.F., Deino, A., Hilgen, F.J., Krijgsman, W., Renne, P.R., and Wijbrans, J.R., 2008, Synchronizing Rock Clocks of Earth History: Science, v. 320, p. 500–504, doi:10.1126/science.1154339.
- Lassiter, J.C., Blichert-Toft, J., Hauri, E.H., and Barszczus, H.G., 2003, Isotope and trace element variations in lavas from Raivavae and Rapa, Cook–Austral islands: constraints on the nature of HIMU- and EM-mantle and the origin of mid-plate volcanism in French Polynesia: Chemical Geology, v. 202, p. 115–138, doi:10.1016/j.chemgeo.2003.08.002.
- Maragos, J. et al., 2008, US Coral Reefs in the Line and Phoenix Islands, Central Pacific Ocean: History, Geology, Oceanography, and Biology, *in* Riegl, B.M. and Dodge, R.E. eds., Coral

- Reefs of the USA, Dordrecht, Springer Netherlands, p. 595–641, doi:10.1007/978-1-4020-6847-8_15.
- Mazza, S.E., Gazel, E., Bizimis, M., Moucha, R., Béguelin, P., Johnson, E.A., McAleer, R.J., and Sobolev, A.V., 2019, Sampling the volatile-rich transition zone beneath Bermuda: *Nature*, v. 569, p. 398–403, doi:10.1038/s41586-019-1183-6.
- McKenzie, D., and Bickle, M.J., 1988, The Volume and Composition of Melt Generated by Extension of the Lithosphere: *Journal of Petrology*, v. 29, p. 625–679, doi:10.1093/petrology/29.3.625.
- McKenzie, D.A.N., and O’Nions, R.K., 1991, Partial Melt Distributions from Inversion of Rare Earth Element Concentrations: *Journal of Petrology*, v. 32, p. 1021–1091, doi:10.1093/petrology/32.5.1021.
- McNutt, M.K., Caress, D.W., Reynolds, J., Jordahl, K.A., and Duncan, R.A., 1997, Failure of plume theory to explain midplate volcanism in the southern Austral islands: *Nature*, v. 389, p. 479–482, doi:10.1038/39013.
- Min, K., Mundil, R., Renne, P.R., and Ludwig, K.R., 2000, A test for systematic errors in $^{40}\text{Ar}/^{39}\text{Ar}$ geochronology through comparison with U/Pb analysis of a 1.1-Ga rhyolite: *Geochimica et Cosmochimica Acta*, v. 64, p. 73–98, doi:10.1016/S0016-7037(99)00204-5.
- Morgan, W.J., 1972, Deep Mantle Convection Plumes and Plate Motions: *AAPG Bulletin*, v. 56, p. 203–213, doi:10.1306/819A3E50-16C5-11D7-8645000102C1865D.
- Mukhopadhyay, S., and Parai, R., 2019, Noble Gases: A Record of Earth’s Evolution and Mantle Dynamics: *Annual Review of Earth and Planetary Sciences*, v. 47, p. 389–419, doi:10.1146/annurev-earth-053018-060238.

- Müller, R.D., Cannon, J., Qin, X., Watson, R.J., Gurnis, M., Williams, S., Pfaffelmoser, T., Seton, M., Russell, S.H.J., and Zahirovic, S., 2018, GPlates: Building a Virtual Earth Through Deep Time: *Geochemistry, Geophysics, Geosystems*, v. 19, p. 2243–2261, doi:10.1029/2018GC007584.
- Naif, S., Miller, N.C., Shillington, D.J., Bécel, A., Lizarralde, D., Bassett, D., and Hemming, S.R., 2023, Episodic intraplate magmatism fed by a long-lived melt channel of distal plume origin: *Science Advances*, v. 9, p. eadd3761, doi:10.1126/sciadv.add3761.
- Nakanishi, M., Tamaki, K., and Kobayashi, K., 1992, Magnetic anomaly lineations from Late Jurassic to Early Cretaceous in the west-central Pacific Ocean: *Geophysical Journal International*, v. 109, p. 701–719, doi:10.1111/j.1365-246X.1992.tb00126.x.
- Neal, C., Coffin, M., and Sager, W., 2019, Contributions of Scientific Ocean Drilling to Understanding the Emplacement of Submarine Large Igneous Provinces and Their Effects on the Environment: *Oceanography*, v. 32, p. 176–192, doi:10.5670/oceanog.2019.142.
- Ogg, J.G., 2020, Geomagnetic Polarity Time Scale, *in* *Geologic Time Scale 2020*, Elsevier, p. 159–192, doi:10.1016/B978-0-12-824360-2.00005-X.
- Olierook, H.K.H., Jourdan, F., and Merle, R.E., 2019, Age of the Barremian–Aptian boundary and onset of the Cretaceous Normal Superchron: *Earth-Science Reviews*, v. 197, p. 102906, doi:10.1016/j.earscirev.2019.102906.
- O'Neill, H.St.C., 2016, The Smoothness and Shapes of Chondrite-normalized Rare Earth Element Patterns in Basalts: *Journal of Petrology*, v. 57, p. 1463–1508, doi:10.1093/petrology/egw047.

- O'Neill, C., Müller, D., and Steinberger, B., 2005, On the uncertainties in hot spot reconstructions and the significance of moving hot spot reference frames: *Geochemistry, Geophysics, Geosystems*, v. 6, p. 2004GC000784, doi:10.1029/2004GC000784.
- Pearce, J.A., 2007, Geochemical fingerprinting of oceanic basalts with applications to ophiolite classification and the search for Archean oceanic crust: *Lithos*, v. 100, p. 14–48, doi:10.1016/j.lithos.2007.06.016.
- Rooney, T.O., Bastow, I.D., and Keir, D., 2011, Insights into extensional processes during magma assisted rifting: Evidence from aligned scoria cones: *Journal of Volcanology and Geothermal Research*, v. 201, p. 83–96, doi:10.1016/j.jvolgeores.2010.07.019.
- Rooney, T.O., Morell, K.D., Hidalgo, P., and Fraceschi, P., 2015, Magmatic consequences of the transition from orthogonal to oblique subduction in P anama: *Geochemistry, Geophysics, Geosystems*, v. 16, p. 4178–4208, doi:10.1002/2015GC006150.
- Rose, J., and Koppers, A.A.P., 2019, Simplifying Age Progressions within the Cook-Austral Islands using ARGUS-VI High-Resolution $^{40}\text{Ar}/^{39}\text{Ar}$ Incremental Heating Ages: *Geochemistry, Geophysics, Geosystems*, v. 20, p. 4756–4778, doi:10.1029/2019GC008302.
- Sano T., Tejada M.L.G., Nakanishi M., Hanyu T., Miura S., Suetsugu D., Tonegawa T., Ishikawa A., Shimizu K., and Shimizu S., 2021, Testing the Ontong Java Nui Hypothesis: The Largest Supervolcano Ever on Earth: *Journal of Geography (Chigaku Zasshi)*, v. 130, p. 559–584, doi:10.5026/jgeography.130.559.
- Schaen, A.J. et al., 2021, Interpreting and reporting $^{40}\text{Ar}/^{39}\text{Ar}$ geochronologic data: *GSA Bulletin*, v. 133, p. 461–487, doi:10.1130/B35560.1.

- Sharp, W.D., and Clague, D.A., 2006, 50-Ma Initiation of Hawaiian-Emperor Bend Records Major Change in Pacific Plate Motion: *Science*, v. 313, p. 1281–1284, doi:10.1126/science.1128489.
- Staudigel, H., and Hart, S.R., 1983, Alteration of basaltic glass: Mechanisms and significance for the oceanic crust-seawater budget: *Geochimica et Cosmochimica Acta*, v. 47, p. 337–350, doi:10.1016/0016-7037(83)90257-0.
- Staudigel, H., Park, K.-H., Pringle, M., Rubenstone, J.L., Smith, W.H.F., and Zindler, A., 1991, The longevity of the South Pacific isotopic and thermal anomaly: *Earth and Planetary Science Letters*, v. 102, p. 24–44, doi:10.1016/0012-821X(91)90015-A.
- Steinberger, B., 2000, Plumes in a convecting mantle: Models and observations for individual hotspots: *Journal of Geophysical Research: Solid Earth*, v. 105, p. 11127–11152, doi:10.1029/1999JB900398.
- Steinberger, B., and O’Connell, R.J., 1998, Advection of plumes in mantle flow: implications for hotspot motion, mantle viscosity and plume distribution: *Geophysical Journal International*, v. 132, p. 412–434, doi:10.1046/j.1365-246x.1998.00447.x.
- Steinberger, B., Sutherland, R., and O’Connell, R.J., 2004, Prediction of Emperor-Hawaii seamount locations from a revised model of global plate motion and mantle flow: *Nature*, v. 430, p. 167–173, doi:10.1038/nature02660.
- Stracke, A., Hofmann, A.W., and Hart, S.R., 2005, FOZO, HIMU, and the rest of the mantle zoo: *Geochemistry, Geophysics, Geosystems*, v. 6, p. 2004GC000824, doi:10.1029/2004GC000824.

- Sun, S. -s., and McDonough, W.F., 1989, Chemical and isotopic systematics of oceanic basalts: implications for mantle composition and processes: Geological Society, London, Special Publications, v. 42, p. 313–345, doi:10.1144/GSL.SP.1989.042.01.19.
- Tamaki, K., and Larson, R.L., 1988, The Mesozoic tectonic history of the Magellan Microplate in the western central Pacific: *Journal of Geophysical Research: Solid Earth*, v. 93, p. 2857–2874, doi:10.1029/JB093iB04p02857.
- Tarduno, J.A. et al., 2003, The Emperor Seamounts: Southward Motion of the Hawaiian Hotspot Plume in Earth's Mantle: *Science*, v. 301, p. 1064–1069, doi:10.1126/science.1086442.
- Tarduno, J., Bunge, H.-P., Sleep, N., and Hansen, U., 2009, The Bent Hawaiian-Emperor Hotspot Track: Inheriting the Mantle Wind: *Science*, v. 324, p. 50–53, doi:10.1126/science.1161256.
- Taylor, B., 2006, The single largest oceanic plateau: Ontong Java–Manihiki–Hikurangi: *Earth and Planetary Science Letters*, v. 241, p. 372–380, doi:10.1016/j.epsl.2005.11.049.
- Timm, C., Hoernle, K., Werner, R., Hauff, F., Den Bogaard, P.V., Michael, P., Coffin, M.F., and Koppers, A., 2011, Age and geochemistry of the oceanic Manihiki Plateau, SW Pacific: New evidence for a plume origin: *Earth and Planetary Science Letters*, v. 304, p. 135–146, doi:10.1016/j.epsl.2011.01.025.
- Tominaga, M., Tivey, M.A., and Sager, W.W., 2021, A New Middle to Late Jurassic Geomagnetic Polarity Time Scale (GPTS) From a Multiscale Marine Magnetic Anomaly Survey of the Pacific Jurassic Quiet Zone: *Journal of Geophysical Research: Solid Earth*, v. 126, p. e2020JB021136, doi:10.1029/2020JB021136.

- Torsvik, T.H., Doubrovine, P.V., Steinberger, B., Gaina, C., Spakman, W., and Domeier, M., 2017, Pacific plate motion change caused the Hawaiian-Emperor Bend: *Nature Communications*, v. 8, p. 15660, doi:10.1038/ncomms15660.
- Torsvik, T.H., Steinberger, B., Shephard, G.E., Doubrovine, P.V., Gaina, C., Domeier, M., Conrad, C.P., and Sager, W.W., 2019, Pacific-Panthalassic Reconstructions: Overview, Errata and the Way Forward: *Geochemistry, Geophysics, Geosystems*, v. 20, p. 3659–3689, doi:10.1029/2019GC008402.
- Turner, D.L., and Jarrard, R.D., 1982, K-Ar dating of the Cook-Austral island chain: A test of the hot-spot hypothesis: *Journal of Volcanology and Geothermal Research*, v. 12, p. 187–220, doi:https://doi.org/10.1016/0377-0273(82)90027-0.
- Vankeken, P., and Ballentine, C., 1998, Whole-mantle versus layered mantle convection and the role of a high-viscosity lower mantle in terrestrial volatile evolution: *Earth and Planetary Science Letters*, v. 156, p. 19–32, doi:10.1016/S0012-821X(98)00023-5.
- Vermeesch, P., 2006, Tectonic discrimination diagrams revisited: *Geochemistry, Geophysics, Geosystems*, v. 7, p. 2005GC001092, doi:10.1029/2005GC001092.
- Weis, D. et al., 2023, Earth's mantle composition revealed by mantle plumes: *Nature Reviews Earth & Environment*, v. 4, p. 604–625, doi:10.1038/s43017-023-00467-0.
- Wessel, P., 2008, Hotspotting: Principles and properties of a plate tectonic Hough transform: *Geochemistry, Geophysics, Geosystems*, v. 9, p. 2008GC002058, doi:10.1029/2008GC002058.
- Wessel, P., and Kroenke, L.W., 2008, Pacific absolute plate motion since 145 Ma: An assessment of the fixed hot spot hypothesis: *Journal of Geophysical Research*, v. 113, p. B06101, doi:10.1029/2007JB005499.

- Wessel, P., and Kroenke, L.W., 1998, The geometric relationship between hot spots and seamounts: implications for Pacific hot spots: *Earth and Planetary Science Letters*, v. 158, p. 1–18, doi:10.1016/S0012-821X(98)00043-0.
- Willbold, M., and Stracke, A., 2006, Trace element composition of mantle end-members: Implications for recycling of oceanic and upper and lower continental crust: *Geochemistry, Geophysics, Geosystems*, v. 7, p. 2005GC001005, doi:10.1029/2005GC001005.
- Wilson, J.T., 1965, A New Class of Faults and their Bearing on Continental Drift: *Nature*, v. 207, p. 343–347, doi:10.1038/207343a0.
- Wilson, J.T., 1963, A Possible Origin of the Hawaiian Islands: *Canadian Journal of Physics*, v. 41, p. 863–870, doi:10.1139/p63-094.
- Woodhead, J.D., 1996, Extreme HIMU in an oceanic setting: the geochemistry of Mangaia Island (Polynesia), and temporal evolution of the Cook—Austral hotspot: *Journal of Volcanology and Geothermal Research*, v. 72, p. 1–19, doi:10.1016/0377-0273(96)00002-9.
- Zheng, L., Gordon, R.G., and Woodworth, D., 2018, Pacific Plate Apparent Polar Wander, Hot Spot Fixity, and True Polar Wander During the Formation of the Hawaiian Island and Seamount Chain From an Analysis of the Skewness of Magnetic Anomaly 20r (44 Ma): *Tectonics*, v. 37, p. 2094–2105, doi:10.1029/2017TC004897.
- Zindler, A., and Hart, S., 1986, Chemical Geodynamics: *Annual Review of Earth and Planetary Sciences*, v. 14, p. 493–571, doi:10.1146/annurev.earth.14.050186.002425.

Curriculum Vitae

Nicholas Michael Foresta
Nforest1756@gmail.com

Education

Masters in Geoscience

August 2024

University of Nevada Las Vegas

- Thesis: “New Insights into the Diverse Intraplate Volcanism Present within the Howland and Baker Island Exclusive Economic Zone”. Advisor: Dr. Kevin Konrad
- GPA: 4.0

Bachelor of Science in Geology

May 2022

University of Nevada Las Vegas

- GPA: 3.74

Experience

Graduate Assistant

Spring 2021-Spring 2024

Geoscience Department, UNLV

- Conducted research on intraplate volcanism using $^{40}\text{Ar}/^{39}\text{Ar}$ geochronology, major and trace element geochemistry, and lithospheric plate reconstructions illustrated with GIS software. Employed analytical techniques including physical/chemical sample preparation of seamount basalts for analyses and dynamic modeling of mantle plumes.
- Collaborated with professors to foster an engaging classroom experience for a diverse student population. Actively communicated with students, providing direct support in the fields of geology and geography. Assist in developing course materials and grading assignments.

Scientist – Ocean Exploration trust (OET)

Summer 2023

E/V Nautilus Expedition NA153

- Served as a research expedition scientist aboard OET’s *E/V Nautilus* NA153 deep sea biodiversity and seamount exploration mission to Johnston Atoll. Regularly communicated

in live streams, describing submarine geologic features and collecting samples. Retrieved, described, and cataloged samples for ongoing research into seamount processes.

Undergraduate Researcher

September 2021 – August 2022

Nevada Plasma Facility Lab, UNLV

- Prepared sample solutions using HNO₃, HCl, and HF acids. Conducted laboratory experiments on pyrite and basalt samples using inductively coupled plasma mass spectrometry (ICP-MS) and performed data reduction on experimental results. Presented research findings during an oral presentation at the UNLV Geosymposium.

Intern

Summer 2021

Maricopa-Stanfield Irrigation Drainage District, Maricopa, Arizona

- Utilized GIS technology to prepare detailed maps illustrating groundwater deficiencies by service area. Assisted the watermaster with logistics, scheduling, and communication for the implementation of the Central Arizona Project drought contingency plan.

Onboard Scientist

Summer 2022

- Prepared sample solutions using HNO₃, HCl, and HF acids. Conducted laboratory experiments on pyrite and basalt samples using inductively coupled plasma mass spectrometry (ICP-MS) and performed data reduction on experimental results. Presented research findings during an oral presentation at the UNLV Geosymposium.

Professional Presentations

Foresta, N., Konrad, K. (2023). New Insights into the Long-lived Macdonald Hotspot from the

Age and Composition of Lava Flows in the Howland and Baker Island US Economic Exclusive Zone. Poster Presentation: American Geophysical Union.

Foresta, N., Konrad, K. (2023). Mapping the Cretaceous to Cenozoic History of the Macdonald Hotspot. Oral Presentation: UNLV Geosymposium.

Foresta, N., DeFelice, C, Huang, S. (2022). Concentrations of U in Th in Pyrites Using the Standard Addition Method. Oral Presentation: UNLV Geosymposium.